Science Reviews

from the end of the world

Pérez Celis - "Energía solar" (1990)

Science Reviews
from the end of the world

Science Reviews - from the end of the world is a quaterly publication that aims at providing authoritative reviews on hot research topics developed mainly by scientists that carry out their work far away from the main centers of science. Its research reviews are short, concise, critical and easy-reading articles describing the state of the art on a chosen hot topic, with focus on the research carried out by the authors of the article. These articles are commissioned by invitation and are accessible not only to hardcore specialists, but also to a wider readership of researchers interested in learning about the state-of-the-art in the reviewed subject. The reviews cover all fields of science and are written exclusively in English. They are refereed by peers of international prestige and the evaluation process follows standard international procedures.

Science Reviews
from the end of the world

Table of Contents

EDITORIAL

Big Science for the Small World

In these strange days of confinement and health emergency, the quality of Argentine Science stands as a strong, comforting light even for those who had never been seduced by scientific research before. And it is like a paradox that the invisible, the small, the nanometric, attracts our attention even more than the big world, showing that, oftentimes, what is essential is (certainly!) invisible to eyes.

Nanomaterials are a unique example of how matter can be redefined when we adopt a different point of view. The nano-scale has given researchers the opportunity of re-discovering matter and to think and dream about applications as broad and diverse that they can be found even in our daily lives. An excellent example of this is brought to us today by María Molina and her group, from Río Cuarto, when she describes photothermal nano-materials with potential applications and impact on medical therapies. But this is not the only area in which nanostructured materials, or "nanomaterials," shine. As Ileana Zucchi from Mar del Plata tells us, the nanoscopic structures formed by a block copolymer can dramatically alter the structure of traditional materials, leading to big changes in many of their properties. The high impact of synthesis control is demonstrated by David Comedi and his team, from Tucumán, who show us how to produce zinc oxide nanostructures with fascinating properties and optical applications. But, how can we study these new properties and the differences of these materials versus their classic relatives without any tools? Félix Requejo from the SUNSET group at La Plata explains an aspect of this "how" when he describes the synchrotron X-ray based techniques applied to the study of nanomaterials.

The diversity of these examples and the very long list of others that, unfortunately, have not been included in this issue due to space limitations, show us the degree of maturity of nanomaterial research lines in Argentina. It is my wish that all this work can continue in the next years and that it translates soon as a positive impact on quality of life for people, the environment and this wonderful country around us.

Cristina E. Hoppe
Editor

Bio

Cristina E. Hoppe

Cristina E. Hoppe was born in Buenos Aires, Argentina, in 1975. She graduated in Chemistry (2000) at the University of Mar del Plata (UNMdP, Argentina), where she also received her Ph.D. in Materials Science (2004) working on polymer dispersed liquid crystals (PDLC) under the supervision of Prof. Roberto J. J. Williams (Institute of Materials Science and Technology, INTEMA, UNMdP/CONICET). In 2004, she was awarded a Postdoctoral Antorchas fellowship and she moved to the University of Santiago de Compostela (Nanotechnology and Magnetism group), Spain, where she worked with Prof. Arturo López Quintela in the synthesis and characterization of metal and oxide nanoparticles. After one year, she was awarded a Marie Curie European Postdoctoral Fellowship (International Incoming Fellowship, 6th framework Programme) to work in the arrangement of nanoparticles in polymer multiphasic systems. She returned to Argentina in December 2007, and she is currently working at INTEMA (Nanostructured Polymers Group) as staff researcher (independent researcher, CONICET). She has been in charge of several research projects in the field of polymer materials and nanomaterials. She has participated as the national representative for the country in international cooperation official missions to USA, Portugal, Italy, Mexico and South Africa in the framework of I+D cooperation agreements in Nanoscience and Nanotechnology. Her main research interests are in relation with the design and application of functional polymers and nanocomposites.

IN THIS ISSUE

ZnO Nanostructures Synthesized by Vapor Transport and Liquid Phase Synthesis Techniques: Growth and Properties

Oscar Marin*, Silvina C. Real*, Nadia Celeste Vega*, Mónica Tirado, and David Comedi**

NanoProject, Departamento de Física, Facultad de Ciencias Exactas y Tecnología, Universidad Nacional de Tucumán (UNT) and Instituto de Física del Noroeste Argentino – INFINOA (CONICET-UNT), San Miguel de Tucumán, Argentina.
* These authors contributed equally to this work.
** Corresponding author. E-mail: dcomedi@herrera.unt.edu.ar

Abstract

In this review, we briefly describe work devoted in recent years towards the effective control of morphology, structure and optical properties of ZnO nanostructures, with particular focus on cost effective and simple methods for ZnO nanowires (NWs) fabrication. For the vapor transport technique, we describe in detail mechanisms for growth precursors generation, their transport in inert and forming gas, as well as their reactions on different pre-treated substrates and corresponding growth mechanisms. As for low temperature synthesis methods, three techniques are outlined: sol-gel, solvothermal and electrophoretic deposition, with emphasis on effective morphology, structure and optical properties control. In this context, we discuss recent attempts to understand the role of solvent and alkaline agents used during solvothermal synthesis of ZnO nanostructures on their morphology and photoluminescence properties. Recent success of electrophoretic deposition of ZnO nanoparticles on pre-patterned silicon substrates in the form of NWs and NW bunches is highlighted over many previous attempts to fabricate ZnO NWs with inconvenient sacrificial templates. Finally, we present a critical discussion on the current understanding of passivation mechanisms of ZnO NW surfaces by MgO shells.
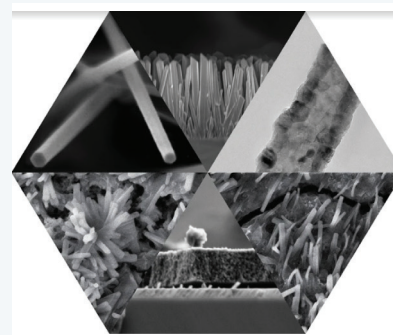
Keywords:
ZnO nanowires, semiconductor nanostructures, electrophoretic deposition, solvothermal synthesis, vapor transport deposition

Introduction

As a result of the rapid progress of modern microelectronics and nanophotonics, semiconductor nanostructures, in particular nanowires (NWs), have attracted much attention during the last two decades, becoming a very active field of research[1,2]. Due to their numerous applications, their versatile properties, and the possibility of integrating them into large areas, new techniques have been developed for the creation of flexible electronic and optoelectronic systems based on these nanostructures, which can eventually be manufactured at mass production scale[3].

Zinc oxide NWs are part of a large family of wide band gap semiconductor nanostructures, including nanoparticles (NPs), nanocombs and nanolayers[4]. Many promising innovative applications in different fields such as photonics[5], spintronics[6] and optoelectronics[4] have been envisaged. ZnO is a II-VI semiconductor that regularly crystallizes in the hexagonal structure of wurtzite, where monoatomic planes of tetrahedrally coordinated O^{2-} or Zn^{2+} atoms alternate along

the axis of hexagonal symmetry (c). This property leads to a preferential growth along this axis, originating elongated nanostructures such as NWs, nanobelts, or nanorods.

Much of the potential of nanotechnology depends on the ability to manipulate atoms during the fabrication process of nanostructures. For ZnO nanostructures, bottom-up approaches have been applied through various growth methods where the specific morphologies were engineered by controlling growth kinetics or thermodynamic conditions through specific choices of techniques and/or fabrication parameters.

In this review, we focus on specific cost effective and simple techniques for ZnO nanostructure growth that our group has thoroughly studied in recent years, such as the vapor transport technique, sol-gel, solvothermal and electrophoretic deposition.

1. Assessment and discussion

1.1. Growth of ZnO nanowires

There are several techniques for the growth of ZnO nanowires, which can be grossly divided into two categories: vapor phase and liquid phase synthesis. Traditionally, vapor phase techniques have been preferred for electronic and optoelectronic device quality materials, while the liquid phase has been regarded as a group of low-cost methods providing the possibility of fabricating NWs at low temperature. However, recent efforts have shown that the latter can yield to optimum high quality ZnO NW materials as well[7].

1.1.1. Gas phase methods

Among gas phase methods, the most popular ones are vapor transport deposition (VTD), molecular beam epitaxy (MBE), pulsed laser deposition (PLD) and atomic layer deposition (ALD).

The VTD technique is one of the simplest methods available to synthesize one-dimensional ZnO nanostructures and is probably the most widely used because of its relatively low-cost and versatility[8]. Basically, this ZnO NW fabrication method consists in transporting Zn and O vapors from some source at high temperature, using an inert gas flow, to the zone of a substrate at lower temperature, where vapor atoms condense, deposit and react, forming nanostructures.

Three important points in this technique should be emphasized: 1) the process used to generate source vapors, 2) the transport regime and 3) the mechanism for NW growth on the substrates.

1) *Vapor source*: Zn and O precursors generation can occur in several ways, such as (to name a few):

    A) Direct sublimation of ZnO powder in an inert atmosphere: for this, temperatures of 1400°C or higher are required, which is technically difficult and relatively expensive[9].

    B) Sublimation of Zn metal in an O_2 atmosphere: this can be achieved at lower temperatures, approximately 500°C[9], but control of the Zn to O_2 partial pressure ratio (P_{Zn}/P_{O2}) on the substrate may be difficult. This directly affects the ability to control the resulting nanostructure stoichiometry and morphology.

    C) The carbothermal reaction, with or without O_2 [8-12], where solid ZnO and graphite powders are mixed to react at high temperature (between 800°C and 1100°C) to reduce the ZnO into Zn and ZnO_x (x<1) cluster vapors, with the formation of CO/CO_2 as a byproduct. Vapors rich in Zn then condense on the substrate and react with O atoms to form the ZnO nanocrystals, while most of the CO/CO_2 molecules (due to their great stability) are essentially removed by the pumping system[13,14].

2) *Vapor transport:* Once Zn or ZnO vapors are generated, they are transported within or by the inert or forming gas through essentially two main mechanisms: diffusion and advection[11]. Roughly speaking, and assuming laminar flow, the first mechanism will become dominant at large working pressures within the reactor tube (typically above few Torr) while the second mechanism dominates at lower pressures. At intermediate pressures, transport by both mechanisms may compete. One way to experimentally check the importance of diffusion is searching for growth on substrates placed upstream the source crucible[11,12]. The transport mechanism will determine the velocity and pressure distributions of Zn precursors along the reactor tube axis, and hence it must be considered when studying growth mechanisms. When advection is dominant, the Zn vapors mean velocity is directly determined by transport

gas flow rate and pumping speed. Under these conditions, Zn precursor pressure (P_{Zn}) will be maximum at a certain distance from the Zn source and then it will decrease to zero at larger distances[11,12,15,16]. The distance at which P_{Zn} is maximum increases with increasing transport gas flow rate. Other parameters that may locally influence Zn growth precursor concentration and velocity distribution at the growth region are the reactor tube diameter, substrate holder shape, and its position along the tube's cross section[17].

3) *NW growth mechanisms*: As the Zn, ZnO_x and O precursors reach the substrate, they react to form the final ZnO product. Substrates in VTD must support high temperatures (usually, they are placed not too far away from the source, in a colder region within the furnace, where temperature is typically between 500°C and 800°C). NW growth typically requires a metal nanocatalyst seed before fabrication[11], although catalyst-free substrates have been also reported[18].

Depending on growth conditions, the application of various mechanisms has been proposed, such as the catalyst-free self-nucleation mechanisms (CFSN), vapor-solid (VS), vapor-liquid-solid (VLS) and combined VLS+VS processes.

The VLS mechanism was originally proposed for Si NW[19] and later reported for ZnO NW growth as well[8]. A typical VLS process begins with the absorption of vapor precursor molecules into particles of a catalyst metal previously deposited on the substrate and melted to the liquid state at a high temperature. Adsorbed reactant gases diffuse through the liquid phase of the metal. Then, the drop is supersaturated and nucleation of a precipitate of the source material occurs at the liquid/solid interface between the alloy drop and the substrate. A mark that reveals the VLS process is the presence of catalyst metal NPs on the tips of the fabricated NWs typically observed through electronic microscopy.

The catalyst must be properly selected to make a one-dimensional nanostructure possible and to avoid unwanted solid phases formation in the medium or to avoid metal contamination of the ZnO NWs. Catalyst species reported for the growth of ZnO NWs are Au, Ag, Se, Cu, and Sn[20]. Also, Zn has been found to act as a self-catalyst, as a result of the decomposition of the Zn growth precursor and its subsequent condensation[19]. This is believed to be the principle for ZnO NW growth on many catalyst-free substrates (CFSN mechanism). The most used catalyst, however, has been Au, which has the advantage that, when it is alloyed with Zn, its melting temperature turns out to be considerably lower than that of pure Au, due to the Au-Zn eutectic temperature of 680°C for an Au rich composition (66%)[21].

Another growth mechanism is VS, which dominates when no intermediate liquid phase for VLS growth is available. In this case, nucleation sites are, in general, structural irregularities at the substrate surface, such as steps, craters, or solid metallic nanoparticles (NPs), whose nanometric roughness results in reactive atomic sites for growth. The VS mechanism was proposed for several ZnO nanostructure growth experiments on substrates without catalysts[11,12,22-24]. When synthetizing ZnO NWs under conditions favoring the VS mechanism, a porous ZnO wetting layer on the metal-seeded substrate has been often observed below the ZnO NWs[11,12]. In this case, the metal catalysts remain below the porous ZnO layer and NWs grow by a VS mechanism on the porous ZnO layer. The mechanism behind this behavior is believed to be a 2D-1D growth transition to reduce strain after some critical strain has accumulated within the 2D ZnO layer[11]. The absence of metal nanoclusters, however, leads to total suppression of any growth on polished crystalline Si wafers[11].

A combined VLS + VS mechanism can also occur on substrates that have catalytic NPs, which remain attached to the substrate during growth[22] or are immersed in a base layer of ZnO. This phenomenon can occur due to the rapid saturation of the catalyst metal droplets, when a large flow of ZnO particles is absorbed, generating a new semiconductor nucleation center, from which the nanostructure grows[22].

Different VTD parameters and their influence on NW morphology and other physical properties have been studied by various authors. When ZnO NWs are grown in the advection regime in O_2-containing forming gas, the Zn partial pressure, P_{Zn}, dependence on the substrate-source distance can be used as a means of changing the P_{Zn}/P_{O2} ratio (P_{O2} = oxygen partial pressure) to control nanostructure growth morphology[11-13]. While P_{O2} is fixed by the O_2 flow rate Q_{O2}, P_{Zn} is determined by the transport gas flow rate, Q_{Tr}, which carries the Zn vapor from the source to the substrate positions. This important variation of P_{Zn} with position has been overlooked in many reports, where only temperature variations with position along the reactor tube axis were considered.

Vega et al.[11] showed that an increase in the vapor source-substrate distance in the advection regime results in a proportional reduction of NW mean diameters and lengths by more than an order of magnitude (from 800 to 40 nm and from 22 to 1 μm, respectively). This was explained as an effect of the reduction of the Zn supersaturation with increasing distance from the Zn source.

It has been shown that ZnO NWs can grow on carbon-based substrates without any metal catalyst[11,17,25]. Furthermore, NWs grow directly from the graphite surface without the presence of any wetting ZnO layer[11,17]. The ZnO/C

system is particularly interesting for field emission applications. In[25], the growth of NWs on amorphous carbon substrates was reported and analyzed, and explained in terms of a VS mechanism favored by the immiscibility between ZnO and C. According to the authors, this immiscibility promotes NW – as opposed to film – growth to reduce the ZnO/C interface area to minimize interface energy.

1.1.2. Liquid phase synthesis methods

ZnO nanostructures can also be obtained through sol-gel[26,27], hydrothermal or solvothermal synthesis[28], co-precipitation, electrophoretic deposition[29], and other liquid phase synthesis techniques. The various advantages offered by these synthetic routes confer them high industrial as well as scientific interest, such as reduction of synthesis temperature and larger yields with respect to vapor deposition methods, and the possibility of implementing scalable processes with better controllability and lower costs. Furthermore, the low synthesis temperature used allows obtaining new metastable phases and materials that would not be feasible using high-temperature fabrication processes[28], hence paving the way for the exploration of new technological applications.

Sol-gel

Sol-gel synthesis is among the most popular routes for ZnO synthesis due to its low cost and possibility to operate at temperatures as low as 150°C. In sol-gel, molecular precursors are transformed on a stable condensed oxide network through multiple stages – in the first step, the formation of a stable sol precursor through hydrolysis and polymerization occurs, followed by condensation through dehydration, nucleation and growth. The highest temperature throughout the synthesis process occurs at the annealing process needed for the growth stage; for ZnO, an annealing temperature as low as 150°C has been reported[30].

Several parameters affect the growth and orientation of sol-gel synthesized nanostructured ZnO films – the main ones are type of chelating agent and drying temperature[31,32]. Marin et al. synthesized ZnO on SiO_2/Si substrates using the sol-gel technique with diethanolamine (DEA) as chelating agent and annealing at 600°C in an Ar/O_2 atmosphere[31,32]. Contrary to what is commonly found when methanolamine (MEA) is used as chelating agent (for which oriented growth along the c-direction of wurtzite occurs only when subjecting samples to high drying temperature at the condensation stage[33]), for DEA such a preferred orientation is observed at low temperature (150°C) and lost at larger temperature (300°C)[32]. This result emphasizes the important role of the chelating agent during condensation and polymerization in determining the final ZnO film texture.

The sol-gel technique also allows the relatively easy fabrication of ZnO alloys. In[34], nanostructured $Zn_xNi_{1-x}O$ films (0 < x < 0.2) were fabricated using DEA as chelating agent. Since a drying temperature of 300°C was used, samples for x=0 (pure ZnO) did not show any preferred orientation. Interestingly, the incorporation of Ni was found to promote strong preferential orientation along the c-direction of the wurtzite structure. The experiments showed that for low x values (x < 0.1), Ni^{2+} ions were incorporated into the ZnO lattice substitutionally. This was evidenced by a reduction of the lattice parameter, the observation of oxidized Ni by X-ray photoelectrons spectroscopy and the absence of the NiO phase in diffraction patterns[34].

Typically, the sol-gel method is used for the fabrication of nanocrystalline thin films on substrates, or it may also be employed to obtain nanostructured powders. In contrast, the growth of ZnO NWs (or nanorods) has been rarely reported, mainly due to the nature of the sol formation process and subsequent gelification. During these stages, nucleation centers are formed within a homogeneous pseudo-polymeric net, and they remain evenly dispersed therein, with no evident mechanism capable of imposing anisotropic growth along any given crystalline direction. However, some reports on ZnO nanorod growth through sol-gel can be found in the literature[30,31], albeit this was achieved during the annealing stage of initially fabricated ZnO thin films through a mechanism that involved surface diffusion of Zn atoms in a solid-solid process[30]. When growing from solution, the fabrication of ZnO NWs and nanotubes using alumina templates has been reported[32], however this technique is complicated due to the high viscosity of colloids used in the sol-gel technique, which hinders their penetration into template pores.

Solvothermal

In recent years, the interest in ZnO nanostructure synthesis by solvothermal routes has increased considerably, mainly motivated by i) the possibility of easily attaining different morphologies through the modification of alkaline agent or solvent, ii) the very low temperature of synthesis, usually between 90 to 150°C, iii) easy doping processes and iv) the possibility of growing different ZnO arrangements on substrates.

The synthesis procedure involves the reaction between a metal precursor with an alkaline agent solubilized in a suitable solvent, which can be either water or organic; the reaction occurs in a polytetrafluoroethylene (PTFE) vessel, which is put inside a stainless steel autoclave.

As for the morphology and its relation with the alkaline agent, synthesis of nanostructured ZnO using several kinds of alkaline agents have been reported, including alkali hydroxides (NaOH and KOH), ammonia hydroxide (NH$_4$OH), ethanolamine family reagents, and hexamethylenetetramine (MHTA), among others.

It has been demonstrated that the use of alkaline agents from the ethanolamine family, when water is used as the solvent, leads to the formation of ZnO microspheres resulting from ZnO nanoparticles agglomeration[28,33], see Fig. 1(a). Experiments with different diethanolamine (DEA) concentrations indicated that DEA plays a multiple role during the synthesis of such microspheres, including precursor stabilization through the formation a stable colloidal phase, providing a growth medium at alkaline pH for the formation of basic ZnO precursors, and the control of the morphology and nanoparticle agglomeration[28]. On the other hand, when HMTA is used as alkaline agent in presence of water, ZnO NWs are obtained instead of nanoparticles or microspheres[34], see Figures 1(b, c).
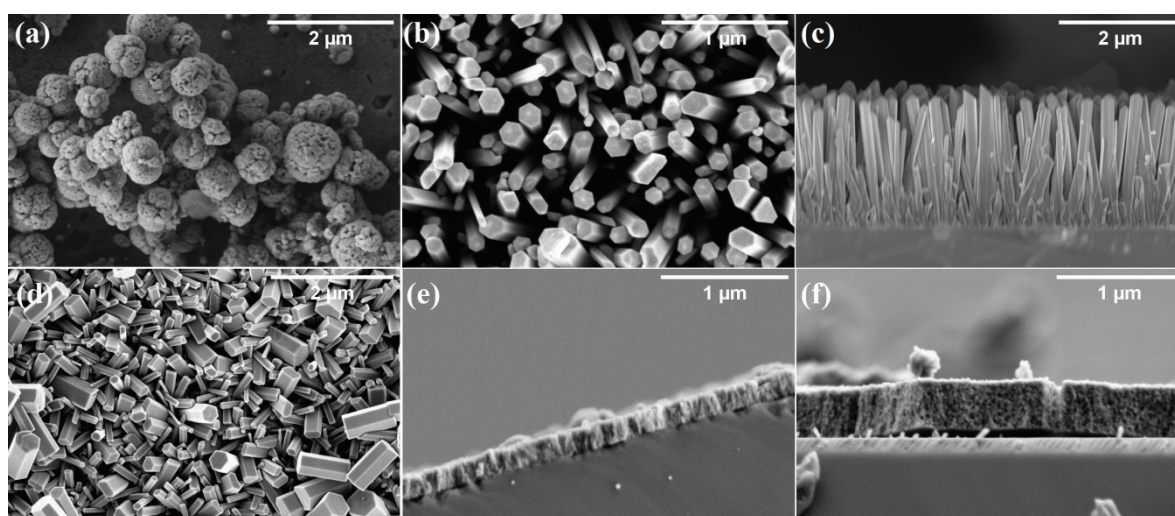

Figure 1. (a) Microspheres obtained with DEA/water; (b, c) top and lateral view of nanowires obtained with HMTA/water respectively; (d) nano and microprism obtained with HMTA and water:methanol 50:50; (e) columnar thin film obtained with DEA/water; (f) microporous thin film obtained with HMTA/methanol.

As mentioned before, the solvothermal synthesis allows obtaining different arrangements of ZnO on a substrate, including oriented ZnO NWs, ZnO nano/microprisms and nanostructured films, just by changing either the alkaline agent or the solvent[34]. Thus, with water as solvent, HMTA leads to oriented NWs, while DEA results in a compact columnar nanostructured film[28,34]. Synthesis with alcohols as solvents using DEA also results in compact columnar films, but for HMTA in alcoholic media, a micropourous film formed by an assemble of NPs instead of NWs is obtained, see Fig. 1(d-f).

The mechanism behind this shape-control with HMTA is currently under discussion. Two main hypotheses have been proposed: i) HMTA is absorbed on non-polar surfaces of the growing ZnO and acts as capping agent, promoting the anisotropic growth along the polar direction and ii) the solubilization and heating of HMTA in water produces its decomposition to formaldehyde and ammonia, and the ammonia can be hydrolyzed to produce OH⁻ [35]; HMTA acts as pH buffer that releases OH⁻ ions slowly to the reactive media, hence promoting a very low ZnO growth rate resembling thermodynamic quasi-equilibrium conditions. In this case, the anisotropic growth arises from the minimization of the surface area on the polar faces, whose surface energy is larger than that of non-polar faces[36].

Regarding the first hypothesis, it has been reported that nanorod synthesis can also be carried out by using NH$_4$OH or adding metallic cations to the solution[37,38], showing that the presence of HMTA or another particular capping agent is not a necessary condition. In addition, the growth of microporous thin films using methanol as solvent, even in presence of HMTA, demonstrates that HMTA by itself does not promote the anisotropic growth that results in ZnO NWs[34].

Recently observed changes in ZnO nanorod morphology induced by varying HMTA concentration[39] and temperature[40] (using water as solvent) indicate that the key to obtain ZnO nanorods is related to the concentration of OH⁻ ions in the

reactive medium. When OH⁻ concentration is low, nanorod growth is promoted. When it increases, other morphologies appear. These findings agree with the hypothesis that the synthesis of ZnO nanorods is controlled by the slow release of OH⁻ rather than by the presence of capping agents on non-polar ZnO faces.

Less studied, but not less interesting, is the relationship between the structure of intermediate compounds in the synthesis and the final morphology of the synthesized ZnO products. Since the composition of such intermediate compounds could be related to the composition of the reactive medium, they are expected to correlate with OH⁻ concentration, which in turn is fixed by alkaline agent concentration. Hence, a current challenge in solvothermal synthesis is designing experiments or autoclaves aimed at studying *in-situ* the initial stages of nanomaterial synthesis in general and ZnO in particular. Some such experiments have already been designed and carried out[41,42]. Of special interest are the compositions of the intermediate compounds, as well as their morphological and structural properties. A detailed study of these could provide valuable information in efforts to unveil the mechanism controlling the morphology, among other physical properties, of solvothermal synthesized nanomaterials.

Photoluminescence

Photoluminescence (PL) is one of the most widely studied characteristics of ZnO because it is one of the properties that lead to promising technological applications such as LED and laser, in addition to providing valuable partial information on the defect structure and bandgap in the ZnO nanostructure[11-13,17,18,24]. A PL spectrum from a ZnO sample excited with larger than bandgap energy photons (usually in the UV) typically exhibits two bands: one in the near-UV (at ~3.2 eV) corresponding to near band-edge (NBE) electron-hole recombination processes ("NBE band"), and a broader one in the visible due to luminescent defect centers with states in the ZnO bandgap ("defect band"). The reader should bear in mind, however, that there is no consensus about a specific defect type responsible for the defect band. For instance, a component centered at ~2.06 eV (yellow emission) has been associated with interstitial oxygen defects but also with oxygen vacancies[18]. For the component centered at ~2.48 eV (green emission), there is also controversy, since it has been attributed to both oxygen vacancies, zinc vacancies and copper contamination[18,43]. Given its relatively large width, the defect band most probably contains contributions from different point defects and defect configurations. Conversely, different point defects may have electronic states at similar energies within the bandgap, thus giving overlapping contributions to the defect PL band.

Hence, it may be expected that PL spectra are very sensitive to the fabrication process. Indeed, in the ZnO nanostructures obtained by high temperature methods (solid state reactions, VTD, sputtering, etc.), the defect band is usually dominated by the green component[11-13,17,18,24], while in those synthesized through chemical methods (sol-gel, co-precipitation, solvothermal synthesis, etc.), the yellow component predominates[28].

Let us first discuss the PL from ZnO nano and microstructures synthesized by solvothermal techniques. When DEA was used as alkaline agent, a time evolution of the PL spectrum while the samples were continuously excited with laser radiation in the UV (3.81 eV) was observed[28]. The defect band in the visible increased and, concomitantly, the NBE band in the UV decreased with irradiation time, see Fig. 2. This PL dependence on irradiation time disappeared, however, when samples were annealed at 900°C for 1 h in air[28]. The fact that the PL could be stabilized both thermally and by prolonged UV illumination led authors to propose that the observed PL behavior was associated with structural metastable configurations that resulted from the low growth temperature[28].

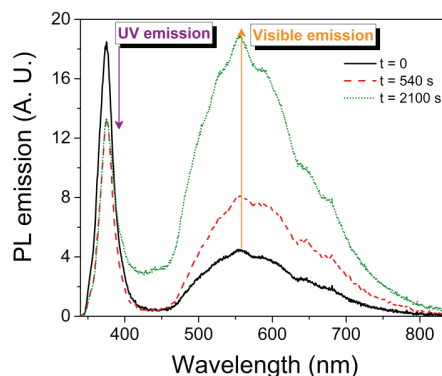The PL from VTD ZnO NWs is discussed in Section 2.2.

Figure 2. Evolution of the photoluminescence spectrum as function of the excitation time for microspheres obtained with DEA/water. The legend indicates the excitation times at which each spectrum was acquired. From [28], copyright IOP.

In addition to the elimination of PL metastability, the annealing treatment also was found to induce enhancement of the yellow emission and reduction of the NBE intensity in the UV. The fact that the yellow component dominates the visible emission in the as-grown samples as well as in the annealed samples, in addition to the yellow band increase at the expense of the UV emission (see Fig. 3), suggests that these samples are in a metastable state characterized by a lower than equilibrium defect density, which increases towards its higher equilibrium value by thermal annealing or by laser irradiation[28].
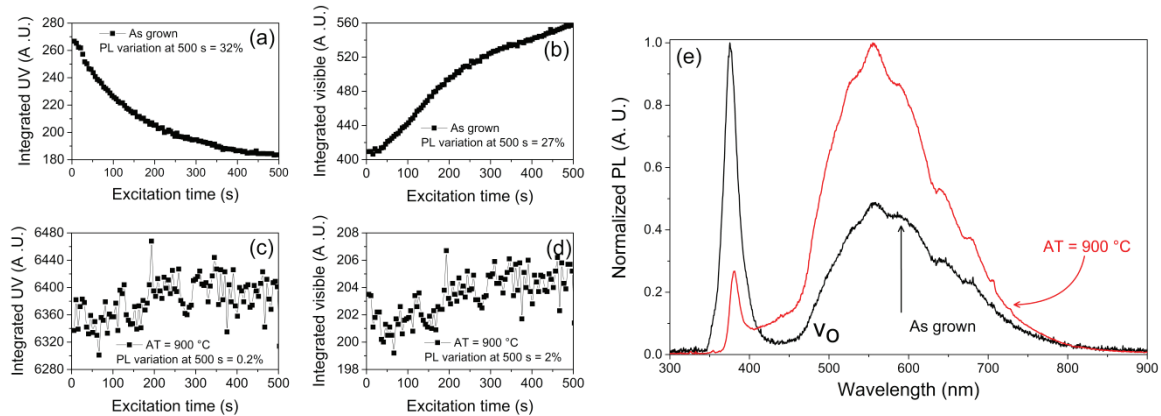

Figure 3. PL evolution for microspheres obtained with DEA/water after annealing at 900°C in air. (a, b) integrated emission intensity from the as-grown sample, (c, d) integrated emission intensity from the sample annealed at 900°C for 1 h. (e) PL spectra for the as-grown (black) and annealed (red) samples. From[28], copyright IOP.

Electrophoretic deposition technique

In the electrophoretic deposition (EPD) technique, charged particles suspended in a liquid move under the action of an electric field through a process known as electrophoresis[44,45]. The electric field is usually produced by a two-electrode system immersed in the liquid suspension, so that charged particles are collected on the oppositely charged electrode to form a deposit. If a stable colloidal suspension with sufficiently low particle content (<10 g/L) is used[46], then the particles are sufficiently separated from each other and arrive individually at the electrode. Hence, by conveniently attaching a substrate to this electrode in such conditions, deposits with excellent particle packing uniformity can be obtained. By changing the colloidal suspension, combined depositions of different types of materials can be obtained on the substrate. Materials deposited by EPD include oxides, nitrides, semiconductors, carbides, cermet, bioactive glasses, organic materials, living cells, and others[44,45,47].

EPD has been recognized as one of the most versatile techniques for particle processing due to the wide variety of size ranges to which it can be applied (from micrometric to nanometric size[47,48]). Nanoparticle EPD was first used by Giersig et al.[49] to prepare ordered monolayers of gold nanoparticles. One of the advantages of EPD over other methods lies on it being a technique based on particles, whose stoichiometry can be controlled during their production stage and, therefore, is directly transferred to the deposit[50]. The characteristics of materials deposited via EPD are influenced as much by parameters related to the colloidal suspension (zeta potential, electrophoretic mobility, pH, conductivity, viscosity, and others) as by physical parameters related to the deposition (working electrode type, substrate material, applied voltage, separation between electrodes, current intensity, deposition time, and others).

The EPD method is an interesting option because it can be used to deposit materials on objects of several shapes and geometrically complicated configurations[45,48,51]. As most wet chemistry methods, EPD does not demand costly or sophisticated equipment. EPD constitutes a low energy consumption, eco-friendly and easily scalable method, which translates as an enormous advantage for its application in the development of low-cost nanotechnology devices.

In this context, the number of publications on electrophoretic deposition of ZnO has been exponentially increasing in the past few years. These cover different topics of the EPD process, such as electrokinetic phenomena, particle stabilization and surface charge, or the use of templates, as well as growth and applications of EPD ZnO thin films.

Experimental results using EPD show that the morphology and quality obtained in the deposition are strongly dependent on the substrate type used[44,45,47]. Substrate conductivity and surface morphology are critical parameters that determine deposit quality. For instance, several authors claim that a low conductivity substrate leads to a non-uniform film and slow deposition rates[45,48].

Table I shows a selected summary of published data on EPD ZnO fabrication; substrates, colloidal suspensions and main EPD process parameters used, as well as resulting morphologies, are listed.

Table I. Summary of results from the literature on EPD ZnO. In all cases parallel electrodes were used, measurements were performed under room conditions and the deposited material was ZnO.

Electrode	Substrate (deposition electrode)	Liquid medium ZnO concentration and ZnO average diameter	Chemical additives used for stablilization and binder agent	Process parameters V, ΔL, Δt	EPD type	Deposition morphology	Reference
Stainless steel	Tin oxide coated glass	0.004 M ZnO colloidal suspension in 2-Propanol average diam.≈ 5 nm Bahnemann [67]	No chemical additives	≈10²V 2 cm 15 min	I=const. 10 mA	Thin Film	Wong and Searson [52]
Stainless steel	Tin oxide coated glass	0.004 M ZnO colloidal suspension in 2-Propanol average diam.≈ 5 nm Bahnemann [67]	No chemical additives	≈10²V 2 cm 1 h	I=const. 10 mA	Thin Film	Wong and Searson [53]
Pt	AAM 200 nm pore diameter attached to Cu foil	ZnO colloidal suspension in 2-Propanol average diam.≈ 5 nm Bahnemann [67]	Binder agent: $Zn(NO_3)_2.6H_2O$	10-30 V 60-400 V 2 cm 5-25 min	V=const.	Nanofibrils Nanotubules In AAM chanels	Wang et al. [54]
Pt	AAM 200 nm pore diameter, Au one side coated attached to Cu foil	ZnO colloidal suspension in 2-Propanol average diam.≈ 5 nm Bahnemann [67]	Binder agent: $Zn(NO_3)_2.6H_2O$	10-30 V 60-400 V 2 cm 5-25 min	V=const.	Nanofibrils Nanotubules In AAM chanels	Wang et al. [55, 56]
Pt	Cu foil	ZnO colloidal suspension in 2-Propanol average diam.≈ 5 nm Bahnemann [67]	Binder agent: $Zn(NO_3)_2.6H_2O$	20-100 V 2 cm 30-1500 s	V=const.	Uniform films	Wang et al. [57]
Cu	Etched n-type Si substrates uncovered/covered with a patterned, developed resist attached to a Cu electrode with In–Ga eutectic	1:5 EtOH/CHCl₃ mixture, ZnO concentrations 10-40 µM	No chemical additives	20-100 V 1-3 cm 1 s - 60 min	V=const.	Films with different thickness	Lommens et al. [58]
Pt	Conductive ITO-glass substrate with deposited colloidal crystal	ZnO colloidal suspension in 2-Propanol average diam.≈ 5 nm Bahnemann [67]	No chemical additives	2.5-25 V 2 cm 5 min	V=const.	High-quality ZnO inverse opal	Chung et al. [59]
Pt	ITO conductive glass	ZnO colloidal suspension in 2-Propanol average diam.≈ 5 nm Bahnemann [67]	No chemical additives	50-300 V 1 cm 8 min	V=const.	Films	Miao et al. [60]
Pt	Stainless Steel and Pt	10 g/L ZnO suspension in ethanol	dopamine hydrochloride or alizarin yellow	20-50 V 1.5 cm 1-10 min	V=const.	Films	Wu et al. [61]
Pt	Electropolished stainless steel	g/L and 1 g/L aqueous flake-shaped ZnO nanopowder suspension average size ≈ 9.8 nm	PEI (Polyethylenimine)	<5 V 2 cm 1-10 min	I=const.	Films	Verde et al. [50]
Stainless steel	WE43 magnesium alloy	5 g/L de ZnO in 10^{-3} M $Zn(NO_3)_2$ in a mixture of 95% vol. anhydrous ethanol and 5 % vol. deionized water, average diam. ≈ 50 nm	No chemical additives	2.5-4 V 2 cm 30-210 min	V=const.	Films	Qu et al. [62]
Pt	Si substrate with Au nanoclusters previously deposited	ZnO colloidal suspension in 2-Propanol average diam.≈ 5 nm Bahnemann [67]	No chemical additives	30 V 7 mm 1 h	V=const.	Nanowires	Sandoval et al. [29]
Pt	B doped Si substrate	ZnO colloidal suspension in 2-Propanol average diam.≈ 5 nm Bahnemann [67]	No chemical additives	33 V 7.5 mm 1 h	V=const.	Nanowires bunches	Real et al. [63] Espíndola et al. [64]

EPD is generally used to obtain films, whereas, according to the bibliography, ZnO with other morphologies or aspect ratios have been achieved mainly through templates. Some of the most widely used templates are anodic alumina membranes (AAM) or porous alumina membranes[47,65]. In these publications, two types of ZnO nanostructure morphologies (fibrils, tubules) and a mix of both, were reported, depending on the voltage-dependent filling characteristics of the AAM. The use of membranes, however, is relatively expensive and difficulties often arise when post-growth elimination of templates is necessary, as is generally the case due to undesired impacts of the membrane on the fabricated composite properties (see, for instance, ref.[66]).

In order to avoid these drawbacks, our research group proposed the use of substrates on which Au nanoclusters had been previously deposited for the growth of ZnO NWs without any membrane templates[29]. Au nanoclusters (15-25 nm) change the morphology of working electrodes and, hence, may promote a concentration of the electric field lines on nanoclusters, thus inducing the preferential deposition of particles on the nanoclusters. Indeed, the metallic character of the nanoclusters should impose new boundary conditions on the electric field lines, leading to their alignment normally to the curved nanocluster surfaces. This would in turn produce a "focusing effect", driving electric field lines away from the uncovered low-conductivity Si substrate and towards the Au nanoclusters. ZnO NPs are electrophoretically transferred from the colloidal suspension to the substrate along the electric field lines, resulting in their columnar packing on Au nanoclusters, giving rise to the observed growth of ZnO NWs. It should be noted that Au nanoclusters do not affect the band gap energy of ZnO nanowires as they are not incorporated into ZnO structure.

EPD deposition was carried out from a low concentration colloidal suspension of ZnO nanoparticles in 2-propanol, synthesized following the precipitation method reported by Bahnemann et al.[67]. The nanoparticles obtained in the colloidal suspension have an average diameter of 5 nm with a narrow size distribution, between 4 and 6 nm, which induces a more orderly packing, since similar sized particles tend to pack together, in concordance with Tabellion et al.[68]. The sample obtained showed a large density of ZnO NWs, with preferential vertical orientation. Their diameters ranged between 20 and 90 nm, and lengths were around ~1.2 µm. The possibility of growing ZnO NWs at room temperature and without the use of templates by EPD is to be highlighted and should lead to further work to explore controllability of the method and properties of the NWs obtained.

More recently, efforts were directed to attain ZnO NW growth by EPD without using metallic nanoclusters. Experiments included the use of highly doped Si substrates for improved conductivity and uniformity of the electric field lines close to the substrates. EPD samples grown on boron doped Si substrates without Au nanoclusters showed novel nanostructures consisting of ZnO NW bunches[63,64]. Figures 4 (a, b) show scanning electron microscopy (SEM) micrographs at different magnifications of the ZnO nanostructures grown on p-type crystalline Si doped with B <100> substrates, polished surface high quality, with resistivity (1-10) Ω cm. Optimum parameters of applied voltage, separation between electrodes and deposition time were 33 V, 7.5 mm and 1 h, respectively. The sample obtained showed a large density of ZnO NW bunches, with diameters ranging between 55 and 85 nm, apparent lengths between 330 and 500 nm and NW bunch diameters around 1 µm.
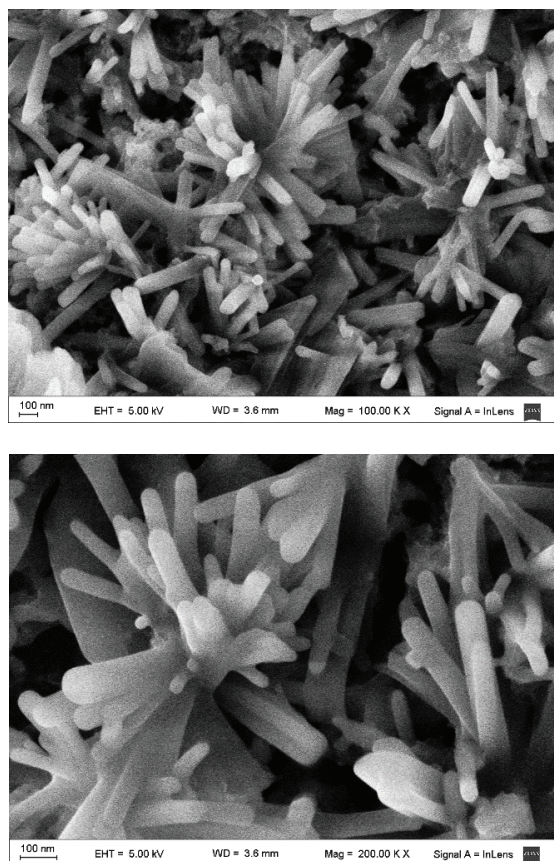

Figure 4. SEM micrographs at different magnifications a) 100 KX and b) 200 KX, of ZnO nanowire bunches, grown on p-type crystalline Si doped with B <100> substrates, with resistivity (1-10) Ω cm. Optimum parameters of applied voltage, electrode-substrate separation and deposition time were 33 V, 7.5 mm and 1 h, respectively.

In the early stages of deposition (at 40 minutes), SEM micrographs show the appearance of a nanoporous film on which NW bunches grow, see Figure 5 (a, b). One might think that the formation of these NW bunches comes from preferential centers of growth, whether present in the substrate or in the nanoporous film. According to Besra et al.[69], particle deposition by EPD on a poor-conducting substrate is made possible through the use of an adequately porous substrate which facilitates availability of electric field near the substrate. The pores, when saturated with the solvent, help establishing a conductive path between the electrical contact and the particles in suspension. Besra found that deposition increases with increasing porosity up to a certain value. For a given applied voltage, there exists a threshold porosity value above which deposition by EPD is possible[45].
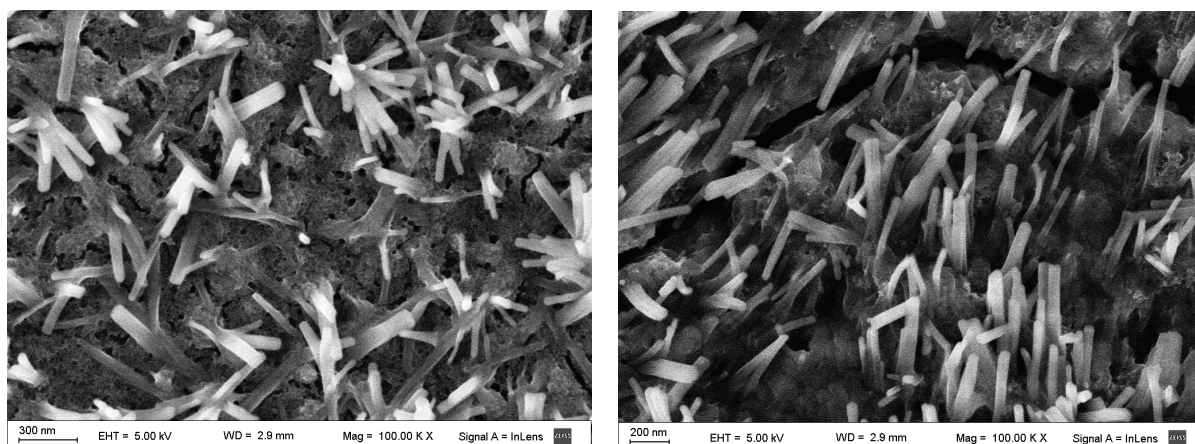

Figure 5. SEM micrographs of ZnO nanowires grown in the first stages of deposition by EPD, corresponding to two different zones of the same sample (a and b). It shows the initial appearance of a nanoporous film on which the ZnO nanowires grow. Parameters of applied voltage, electrode-substrate separation and deposition time were 33 V, 7.5 mm and 40 minutes, respectively. SEM micrographs at 100 KX of magnification.

1.2. Surface passivation of ZnO NWs

Many years of research have shown that the effective surface passivation of ZnO nanomaterials to neutralize surface electronic and optical effects is crucial for applications in optoelectronics due to the large specific surface area of these nanostructures. For instance, surface trap states shorten carrier lifetimes and are responsible for deep-defect luminescence in the visible[24,70]. Strategies proposed to provide effective passivation have included annealing in forming atmospheres and the deposition of various shell materials, such as PMMA[71], polyvinyl-alcohol (PVA)[72] or polymers[73]. The MgO coating of the ZnO NW has been proved to reduce lasing thresholds and enhance excitonic PL[24,74-75]. As ZnO, MgO is II-VI wide band-gap oxide; however, since it exhibits a much larger MgO bandgap than that of ZnO (~7.8 eV as compared to ~3.3 eV), a MgO shell is expected to provide very efficient confining barriers to both electrons and holes within the ZnO core, which in turn should further favor UV radiative excitonic recombination. Typically, hydrothermal[4] and electron beam evaporation synthesis[78] have been used to coat ZnO NWs with MgO. An attractive method for the fabrication of ZnO and ZnO/MgO core/shell NWs is VTD[75].

While the MgO shell is indeed very useful in improving the UV emission from ZnO nanostructures and reducing the spurious visible emission due to surface defects, the physical passivation mechanisms behind these improvements remained elusive for many years. Some authors suggested that the MgO shell physically removes oxygen vacancies or other defects from the ZnO NW walls, thus eliminating the recombination channels that compete with the excitonic recombination[79]. Others, inspired by the fact that efficient passivation effects have been achieved using not only MgO, but also polymers and other insulating materials, proposed a model where dielectric screening that could be provided by any dielectric shell was responsible for the beneficial effects observed[80]. Later, a new model was introduced where passivation is not due to elimination of surface states, but a result of mechanical stabilization of the nanosurfaces[81].

Grinblat et al.[24] and Vega et al.[76] studied this problem in ZnO/MgO core/shell NWs grown by a two-step VTD technique. Scanning and transmission electron microscopy (SEM and HRTEM) images of the ZnO and ZnO/MgO core/shell NWs are shown in Fig. 6. A clear correlation between the PL defect/NBE bands ratio and the specific surface area of hierarchical ZnO nanostructures[12] had shown previously that most luminescent defects were at the ZnO surfaces. By analyzing PL temperature dependence on ZnO/MgO core/shell NW samples, it was concluded that the MgO shell, when grown under the right conditions, led to strong shortening of the excitonic radiative recombination time and to orders of

magnitude increase of the UV emission[24]. In[76], ZnO/MgO core/shell NWs with varying shell widths (w) were grown in an effort to shed light on the passivation mechanism. The PL dependence on w revealed that a thin MgO shell of a few monolayers was not enough to fully passivate the surface. Instead, a gradual increase (decrease) of the PL intensity for the UV (visible) band with increasing w was observed. Only after a sufficiently thick shell was deposited ($w \sim 17$ nm), optimal passivation was attained[76]. This was explained as the combination of two effects: one related to the elimination of the ZnO NW/air interface, which is achieved for the thinnest MgO shell, and another w-dependent effect.
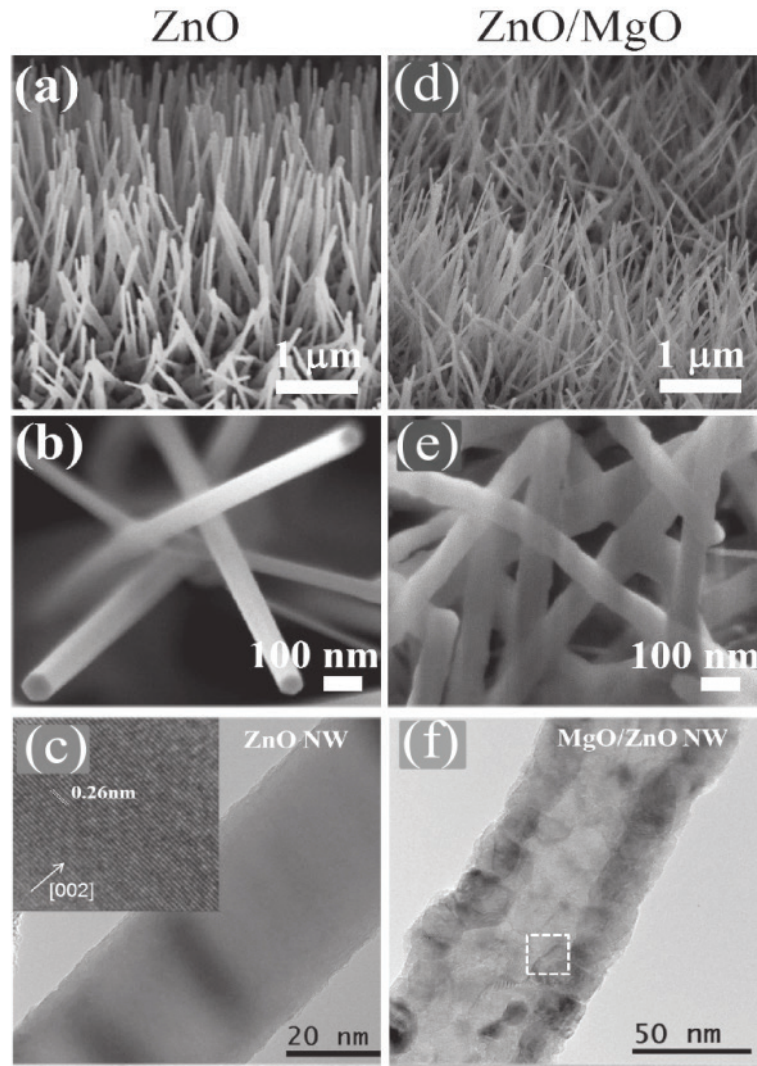
Figure 6. SEM images with different magnifications of a ZnO NW sample (a), (b) and of a ZnO/MgO core/shell NW sample (d), (e). As observed in (b), the ZnO NWs are highly crystalline, exhibiting hexagonal cross-section expected from wurtzite c-axis alignment. (c) and (f) show HRTEM images of a ZnO NW and of a ZnO/MgO core/shell NW, respectively. From[76].

To understand these effects, the excitonic NBE emission band shape dependence on w was carefully studied. The intensities of the first and second longitudinal-optical (LO) phonon replica of the free exciton recombination emission, which dominate the NBE band from ZnO at room temperature, changed dramatically with the incorporation of the MgO shell; see Fig. 7[76]. The relative contribution of the second phonon replica was strongly reduced, while the otherwise weak free exciton recombination contribution was intensified by orders of magnitude. This indicated a reduced exciton-phonon coupling probably because the MgO shell induced reduction of Zn and O atoms surface vibrational amplitudes.

Figure 7. Experimental (black symbols) and fitted (yellow lines) PL spectra from ZnO (a) and from ZnO/MgO core/shell NW samples (b, c, d), for different MgO shell widths, w, in the UV region (NBE band). The components of the fits attributed to the excitonic emission (X) and its phonon replica (X-1LO, X-2LO) are indicated by vertical dashed lines (positions) and by blue, red, and green, respectively. Note the very different vertical scales in (a, b, c, d). From[76].

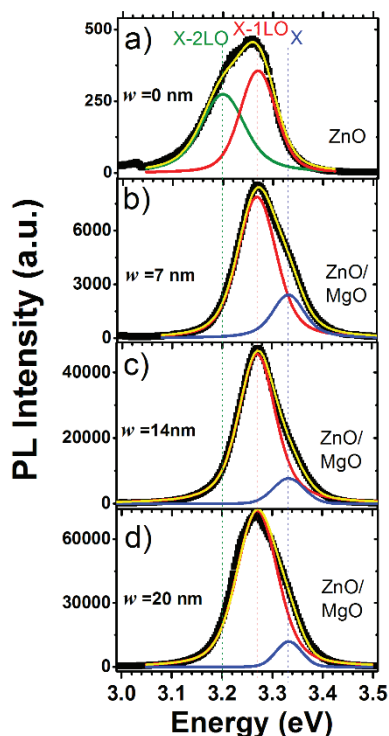The study also found significant strain build-up within the ZnO core, which increased with increasing MgO shell width w and correlated with the NBE/defect bands intensity ratio. It was then concluded that the NBE band enhancement and defect band quench in the core/shell NWs involved complex mechanisms that include elimination of adsorbates and mechanical stabilization of the ZnO NW interface (which dominate for small w) and strain build-up (which becomes increasingly important with increasing w).

Conclusion

In this review, we have briefly described much of the important work devoted in recent years towards the effective control of the morphology, structure and optical properties of ZnO nanostructures, with special focus on our own work on ZnO NWs. Much progress has been achieved in the basic understanding of the main mechanisms involved in VTD, enabling better control and reproducibility of ZnO NW growth and properties, such as length, diameter and luminescence. Furthermore, it has been possible to synthetize ZnO NWs under different prevailing mechanisms (such as VLS, VS and VLS+VS), to systematically change the ZnO nanostructure morphology by changing the P_{Zn}/P_{O2} ratio, to synthetize NWs without metal catalyst, to eliminate the ZnO layer that grows under advection conditions on various metal catalyzed substrates, and to fabricate ZnO/MgO core/shell NWs.

In the quest for novel applications of NWs potential in general, and ZnO NWs in particular, the proposal for their integration into flexible (optoelectronic, electronic, spintronic, photonic or any combination of these) circuits has promoted the development of novel growth methods at low temperatures. The possibility of synthesizing ZnO NWs at room temperature on at least two types of conveniently preformed substrates by just manipulating colloidal ZnO NPs with electric fields, as in EPD, is very encouraging. Even though understanding of growth mechanisms during sol-gel, solvothermal and EPD techniques has improved substantially as a result of years of research, especially on the role of the solvent and the alkaline agent on the morphology during solvothermal synthesis, it is clear that much work is still needed. In particular, studies on the composition and structure of intermediate products within the complex reactive media in solvothermal synthesis are needed to achieve a better control of the size and defect structure of ZnO nanostructures deposited at low temperatures on the one hand. PL metastability, on the other hand, deserves greater attention because it shows structural

metastabilities that, albeit expected for low temperature processing, could be detrimental for real life applications of these nanostructures.

Last but not least, it is clear that after many years of work, a consistent picture of the ZnO NW surface passivation mechanism is finally emerging. The main role of the shell is that of a physical barrier that separates the ZnO NW walls from atmospheric adsorbates, which otherwise provide detrimental surface states on ZnO NW walls. Hence, to a first approximation, this can explain the large enhancements of the UV emission and the quenching of the defect band when NWs are covered with a broad range of shells (from polymers to ceramic oxides). However, other important physical effects (such as strain buildup, mechanical stabilization and confinement) may also occur, which lead to strong changes in PL spectra and may depend on shell thickness. Some of these effects are specific to the shell material, as they depend on the shell electronic, structural and mechanical properties. Future studies will focus on applications of these passivated ZnO NWs on different devices and the choice of the passivating shell material will certainly depend on each technological platform specific requirements.

References

[1] Y. Xia, P. Yang, Y. Sun, Y. Wu, B. Mayers, B. Gates, Y. Yin, F. Kim, and H. Yan. One-Dimensional Nanostructures: Synthesis, Characterization, and Applications. *Adv. Mater.*, 15(5):353-389, 2003.

[2] C. Lieber and Z. Wang. Functional Nanowires. *MRS Bull.*, 32(02):99-108, 2007.

[3] X. Wang, C. Summers, and Z. Wang. Large-Scale Hexagonal-Patterned Growth of Aligned ZnO Nanorods for Nano-optoelectronics and Nanosensor Arrays. *Nano Lett.*, 4(3):423-426, 2004.

[4] M. Willander. *Zinc Oxide Nanostructures: Advances and Applications.* Jenny Stanford Publishing, New York, USA, 2013.

[5] G. Grinblat, M. Rahmani, E. Cortés, M. Caldarola, D. Comedi, S. Maier, and A. Bragas. High Efficiency Second Harmonic Generation from a Single Hybrid ZnO Nanowire/Au Plasmonic Nano-Oligomer. *Nano Lett.*, 14(11):6660-6665, 2014.

[6] Y. Tian, S. Bakaula, and T. Wu. Oxide Nanowires for Spintronics: Materials and Devices. *Nanoscale*, 4:1529-1540, 2012.

[7] A. Kołodziejczak-Radzimska and T. Jesionowski. Zinc Oxide-From Synthesis to Application: A Review. *Materials*, 7(4):2833-2881, 2014.

[8] M. Huang, Y. Wu, H. Feick, N. Tran, E. Weber, and P. Yang. Catalytic Growth of Zinc Oxide Nanowires by Vapor Transport. *Adv. Mater.*, 13(2):113-116, 2001.

[9] Z. Wang. Zinc Oxide Nanostructures: Growth, Properties and Applications. *J. Phys. Condens. Matter.*, 16(25):829-858, 2004.

[10] D. Comedi, M. Tirado, C. Zapata, S.P. Heluani, M. Villafuerte, P. Mohseni, and R.R. LaPierre. Randomly Oriented ZnO Nanowires Grown on Amorphous SiO_2 by Metal-Catalized Vapour Deposition. *J. Alloys Compd.*, 495(2):439-442, 2010.

[11] N.C. Vega, R. Wallar, J. Caram, G. Grinblat, M. Tirado, R.R. LaPierre, and D. Comedi. ZnO Nanowire co-Growth on SiO_2 and C by Carbothermal Reduction and Vapour Advection. *Nanotechnology*, 23(27):275602, 2012.

[12] G. Grinblat, M.G. Capeluto, M. Tirado, A.V. Bragas, and D. Comedi. Hierarchical ZnO nanostructures: Growth Mechanisms and Surface Correlated Photoluminescence. *Appl. Phys. Lett.*, 100:233116, 2012.

[13] N.C. Vega, M. Tirado, D. Comedi, A. Rodriguez, T. Rodriguez, G. Hughes, Crm. Grovenor, and F. Audebert. Electrical, Photoelectrical and Morphological Properties of ZnO Nanofiber Networks Grown on SiO_2 and on Si Nanowires. *Mater. Res.*, 16(3):597-602, 2013.

[14] M. Biswas, E. Mcglynn, M. Henry, M. McCann, and A. Rafferty. Carbothermal Reduction Vapor Phase Transport Growth of ZnO Nanostructures: Effects of Various Carbon Sources. *J. Appl. Phys.*, 105(9):094306, 2009.

[15] C. Ye, X. Fang, Y. Hao, X. Teng, and L. Zhang. Zinc Oxide Nanostructures: Morphology Derivation and Evolution. *J. Phys. Chem. B*, 109(42):19758-19765, 2005.

[16] J.H. Choi, J.S. Seo, S.N. Cha, H.J. Kim, S.M. Kim, Y.J. Park, S. Kim, J. Yoo, and J.M. Kim. Effects of Flow Transport of the Ar Carrier on the Synthesis of ZnO Nanowires by Chemical Vapor Deposition. *Jpn. J. Appl. Phys.*, 50(1R):015001, 2011.

[17] E. Tosi. Estudio de Superficies de Nanoestructuras Semiconductoras. PhD Thesis, Universidad Nacional de Tucumán, Argentina (2019).

[18] O. Marin, G. Grinblat, A.M. Gennaro, M. Tirado, R.R. Koropecki, and D. Comedi. On the Origin of White Photoluminescence from ZnO Nanocones/Porous Silicon Heterostructures at Room Temperature. *Superlattices Microstruct.*, 79:29-37, 2015.

[19] R.S. Wagner and W.C. Ellis. Vapor-Liquid-Solid Mechanism of Single Crystal Growth. *Appl. Phys. Lett.*, 4(5):89-90, 1964.

[20] T. Steiner. *Semiconductor Nanostructures for Optoelectronics Applications*. Semiconductor Materials and Devices Series, Artech House, Inc., USA, 2004.

[21] H.S. Liu, K. Ishida, Z.P. Jin, and Y. Du. Thermodynamic Assessment of the Au-Zn Binary System. *Intermetallics*, 11(10):987-994, 2003.

[22] D.S. Kim, R. Scholz, U. Gösele, and M. Zacharias. Gold at the Root or at the Tip of ZnO Nanowires: A Model. *Small*, 4(10):1615-1619, 2008.

[23] G. Zhu, Y. Zhou, S. Wang, R. Yang, Y. Ding, X. Wang, Y. Bando, and Z. Wang. Synthesis of Vertically Aligned Ultra-Long ZnO Nanowires on Heterogeneous Substrates with Catalyst at the Root. *Nanotechnology*, 23(5):055604, 2012.

[24] G. Grinblat, L.J. Borrero González, L.A.O. Nunez, M. Tirado, and D. Comedi. Enhanced optical properties and (Zn, Mg) interdiffusion in vapour transport grown ZnO/MgO core/shell nanowires. *Nanotechnology,* 25(3):035705, 2014.

[25] Y.H. Yang, C.X. Wang, B. Wang, N. Xu, and G.W. Yang. ZnO nanowire and amorphous diamond nanocomposites and field emission enhancement. *Chem. Phys. Lett.*, 403(4-6):248-251, 2005.

[26] O. Marin, P. Alastuey, E. Tosi, J. Orive, E. Mosquera, G. Zampieri, S. Suárez, D. Comedi, and M. Tirado. Suppression of the green emission, texturing , solute-atom diffusion and increased electron-phonon coupling induced by Ni in sol-gel ZnNiO thin films. *Appl. Surf. Sci.*, 456:771-780, 2018.

[27] O. Marin, M. Tirado, N. Budini, E. Mosquera, C. Figueroa, and D. Comedi. Photoluminescence from c-axis oriented ZnO films synthesized by sol-gel with diethanolamine as chelating agent. *Mater. Sci. Semicond. Process.*, 56:59-65, 2016.

[28] V. González, O. Marin, M. Tirado, and D. Comedi. Metastability effects on the photoluminescence of ZnO nano-micro structures grown at low temperature and influence of the precursors on their morphology and structure. *Mater. Res. Express*. 5:125003, 2018.

[29] C. Sandoval, O. Marin, S. Real, D. Comedi, and M. Tirado. Electrophoretic deposition of ZnO nanostructures: Au nanoclusters on Si substrates induce self-assembled nanowire growth. *Mater. Sci. Eng. B*, 187:21-25, 2014.

[30] M.W. Zhu, N. Huang, J. Gong, B. Zhang, Z.J. Wang, C. Sun, and X. Jiang. Growth of ZnO nanorod arrays by sol-gel method: transition from two-dimensional film to one-dimensional nanostructure. *Appl. Phys. A*, 103(1):159-166, 2011.

[31] Y. Song, M. Zheng, L. Ma, and W. Shen. Anisotropic growth and formation mechanism investigation of 1D ZnO nanorods in spin-coating sol-gel process. *J. Nanosci. Nanotechnol.*, 10(1):426-432, 2010.

[32] G.S. Wu, T. Xie, X.Y. Yuan, Y. Li, L. Yang, Y.H. Xiao, and L.D. Zhang. Controlled synthesis of ZnO nanowires or nanotubes via sol-gel template process. *Solid State Commun.*, 134:485-489, 2005.

[33] O. Marin, T. Soliz, J.A. Gutierrez, M. Tirado, C. Figueroa, and D. Comedi. Structural, optical and vibrational properties of ZnO:M (M=Al^{3+} and Sr^{2+}) nano and micropowders grown by hydrothermal synthesis. *J. Alloys Compd.*, 789:56-65, 2019.

[34] O. Marin, V. González, M. Tirado, and D. Comedi. Effects of methanol on morphology and photoluminescence in solvothermal grown ZnO powders and ZnO on Si. *Mater. Lett.*, 251:41-44, 2019.

[35] Z. Liu, S. Liu, W. Wu, and C.R. Liu. Mechanism of controlled integration of ZnO nanowires using pulsed-laser-induced chemical deposition. *Nanoscale*, 11(6):2617-2623, 2019.

[36] K.M. McPeak, T.P. Le, N.G. Britton, Z.S. Nickolov, Y.A. Elabd, and J.B. Baxter. Chemical Bath Deposition of ZnO Nanowires at Near-Neutral pH Conditions without Hexamethylenetetramine (HMTA): Understanding the Role of HMTA in ZnO Nanowire Growth. *Langmuir*, 27(7):3672-3677, 2011.

[37] Y. Tak, and K. Yong. Controlled Growth of Well-Aligned ZnO Nanorod Array Using a Novel Solution Method. *J. Phys. Chem. B.*, 109(41):19263-19269, 2005.

[38] J. Joo, B.Y. Chow, M. Prakash, E.S. Boyden, and J.M. Jacobson. Face-selective electrostatic control of hydrothermal zinc oxide nanowire synthesis. *Nat. Mater.*, 10(8):596-601, 2011.

[39] R. Devaraj, K. Venkatachalam, K. Saravanakumar, P.M. Razad, and K. Mahalakshmi. Role of hexamine: growth of multiarmed ZnO nanorods and evidence of merging due to lateral growth. *J. Mater. Sci. - Mater. Electron.*, 27(11):12201-12208, 2016.

[40] A. Saranya, T. Devasena, H. Sivaram, and R. Jayavel. Role of hexamine in ZnO morphologies at different growth temperature with potential application in dye sensitized solar cell. *Mater. Sci. Semicond. Process.*, 92:108, 2019.

[41] P. Nørby, M. Roelsgaard, M. Søndergaard, and B.B. Iversen. Hydrothermal Synthesis of CoSb$_2$O$_4$: In Situ Powder X-ray Diffraction, Crystal Structure, and Electrochemical Properties. *Cryst. Growth Des.*, 16(2):834-841, 2016.

[42] E.D. Bøjesen, K.M.Ø. Jensen, C. Tyrsted, N. Lock, M. Christensen, and B.B. Iversen. In Situ Powder Diffraction Study of the Hydrothermal Synthesis of ZnO Nanoparticles. *Cryst. Growth Des.*, 14(6):2803-2810, 2014.

[43] J.L. Lyons, A. Alkauskas, A. Janotti, and C.G. Van De Walle. Deep donor state of the copper acceptor as a source of green luminescence in ZnO. *Appl. Phys. Lett.*, 111(4):042101/1-5, 2017.

[44] B. Ferrari, and R. Moreno. EPD kinetics: A review. *J. Eur. Ceram. Soc.*, 30(5):1069-1078, 2010.

[45] L. Besra, and M. Liu. A review on fundamentals and applications of electrophoretic deposition (EPD). *Prog. Mater. Sci.*, 52(1):1-61, 2007.

[46] P. Sarkar, and P.S. Nicholson. Electrophoretic Deposition (EPD): Mechanisms, Kinetics, and Application to Ceramics. *J. Am. Ceram. Soc.*, 79(8):1987-2002, 1996.

[47] J.H. Dickerson, and A.R. Boccaccini. *Electrophoretic Deposition of Nanomaterials*. Springer, New York, 2012.

[48] P. Amrollahi, J.S. Krasinski, R. Vaidyanathan, L. Tayebi, and D. Vashaee. Chapter 17: Electrophoretic Deposition (EPD): Fundamentals and Applications from Nano- to Microscale Structures. In *Handbook of Nanoelectrochemistry*. Springer International Publishing Switzerland, 2015.

[49] M. Giersig, and P. Mulvaney. Formation of ordered two-dimensional gold colloid lattices by electrophoretic deposition. *J. Phys. Chem.*, 97(24):6334-6336, 1993.

[50] M. Verde, M. Peiteado, A.C. Caballero, M. Villegas, and B. Ferrari. Electrophoretic Deposition of Transparent ZnO Thin Films from Highly Stabilized Colloidal Suspensions. *J. Colloid Interface Sci.*, 373(1):27-33, 2012.

[51] M. Verde. EPD-deposited ZnO thin films: a review. *Boletín de la Sociedad Española de Cerámica y Vidrio*, 53(4):149-161, 2014.

[52] E.M. Wong and P.C. Searson. Kinetics of Electrophoretic Deposition of Zinc Oxide Quantum Particle Thin Films. *Chem. Mater.*, 11(8):1959-1961, 1999.

[53] E.M. Wong and P.C. Searson. ZnO quantum particle thin films fabricated by electrophoretic deposition. *Appl. Phys. Lett.*, 74:2939-2942, 1999.

[54] Y.-C. Wang, I.-C. Leu, and M.-H. Hon. Preparation of Nanosized ZnO Arrays by Electrophoretic Deposition. *Electrochem. Solid-State Lett.*, 5(4):C53-C55, 2002.

[55] Y.-C. Wang, I.-C. Leu, and M.-H. Hon. Effect of colloid characteristics on the fabrication of ZnO nanowire arrays by electrophoretic deposition. *J. Mater. Chem.*, 12(8):2439–2444, 2002.

[56] Y.-C. Wang, I.-C. Leu, and M.-H. Hon. Size Control of ZnO Nanofibril within Template by Electrophoretic Deposition. *Electrochem. Solid-State Lett.*, 7(10):D15-D18, 2004.

[57] Y.-C. Wang, I.-C. Leu, and M.-H. Hon. Kinetics of Electrophoretic Deposition for Nanocrystalline Zinc Oxide Coatings. *J. Am. Ceram. Soc.*, 87(1):84-88, 2004.

[58] P. Lommens, D. Van Thourhout, P.F. Smet, D. Poelman, and Z. Hens. Electrophoretic deposition of ZnO nanoparticles, from micropatterns to substrate coverage. *Nanotechnology*, 19(24):245301, 2008.

[59] Y.-W. Chung, I.-C. Leu, J.-H. Lee, and M.-H. Hon. Filling behavior of ZnO nanoparticles into opal template via electrophoretic deposition and the fabrication of inverse opal. *Electrochim. Acta*, 54(13):3677-3682, 2009.

[60] L. Miao, S. Cai, and Z. Xiao. Preparation and characterization of nanostructured ZnO thin film by electrophoretic deposition from ZnO colloidal suspensions. *J. Alloys Compd.*, 490(1-2):422-426, 2010.

[61] K. Wu, and I. Zhitomirsky. Electrophoretic Deposition of Ceramic Nanoparticles. *Int. J. Appl. Ceram. Technol.*, 8(4):920-927, 2011.

[62] J.E. Qu, M. Ascencio, L.M. Jiang, S. Omanovic, and L.X. Yang. Improvement in corrosion resistance of WE43 magnesium alloy by the electrophoretic formation of a ZnO surface coating. *J. Coat. Technol. Res.*, 1-12, 2019.

[63] S. Real, O. Espindola, O. Marin, D. Comedi, and M. Tirado. Novel nanostructures grown by electrophoretic deposition using Si substrates with low resistivity (58). In *Electrophoretic Deposition VI: Fundamentals and Applications*, A. Boccaccini, O. van der Biest, J. Dickerson (Eds), ECI Symposium Series (58), 2017.

[64] O. Espindola, S. Real, O. Marin, D. Comedi, and M. Tirado. Influence of substrate morphology on ZnO nanostructures grown by electrophoretic deposition (4). In *Electrophoretic Deposition VI: Fundamentals and Applications*, A. Boccaccini, O. van der Biest and J. Dickerson (Eds), ECI Symposium Series (4), 2017.

[65] Y.C. Wang, I.C. Leu, and M.H. Hon. Effect of colloid characteristics on the fabrication of ZnO nanowire arrays by electrophoretic deposition. *J. Mater. Chem.*, 12(8):2439-2444, 2002.

[66] Y.C. Wang, I.C. Leu, and M.H. Hon. Dielectric property and structure of anodic alumina template and their effects on the electrophoretic deposition characteristics of ZnO nanowire arrays. *J. Appl. Phys.*, 95(3):1444-1449, 2004.

[67] D.W. Bahnemann, C. Kormann, and M.R. Hoffmann. Preparation and characterization of quantum size zinc oxide: a detailed spectroscopic study. *J. Phys. Chem.*, 91(14):3789–3798, 1987.

[68] J. Tabellion, and R. Clasen. Electrophoretic deposition from aqueous suspension for near-shape manufacturing of advanced ceramics and glasses–applications. *J. Mater. Sci*, 39:803–811, 2004.

[69] L. Besra, and M. Liu. Electrophoretic Deposition on Non-Conducting Substrates: The Case of YSZ Film on NiO-YSZ Composite Substrates for Solid Oxide Fuel Cell Application. *J. of Power Sources*, 173(1):130-136, 2007.

[70] Y. Yang, X.W. Sun, B.K. Tay, P.H.T. Cao, J.X. Wang, and X.H. Zhang. Revealing the surface origin of green band emission from ZnO nanostructures by plasma immersion ion implantation induced quenching. *J. Appl. Phys.*, 103(6):064307, 2008.

[71] W.K. Hong, B.J. Kim, T.W. Kim, G. Jo, S. Song, S.S. Kwon, A. Yoon, E.A. Stach, and T. Lee. Electrical properties of ZnO nanowire field effect transistors by surface passivation. *Colloids Surf. A: Physicochem. Eng. Aspects*, 313-314(1):378-382, 2008.

[72] L. Qin, C. Shing, S. Sawyer, and P.S. Dutta. Enhanced ultraviolet sensitivity of zinc oxide nanoparticle photoconductors by surface passivation. *Opt. Mater.*, 33(3):359-362, 2011.

[73] L. Guo, S. Yang, C. Yang, P. Yu, J. Wang, W. Ge, and G.K.L. Wong. Highly monodisperse polymer-capped ZnO nanoparticles: Preparation and optical properties. *Appl. Phys. Lett.*, 76(20):2901-2903, 2000.

[74] H.Y. Yang, S.F. Yu, G.P. Li, and T. Wu. Random lasing action of randomly assembled ZnO Nanowires with MgO coating. *Opt. Express*, 18(13):13647-13654, 2010.

[75] Y. Wu, W. Wu, X.M. Zou, L. Xu, and J.C. Li. Growth and great UV emission improvement of highly crystalline quality core–shell ZnO/MgO nanowires. *Mater. Lett.*, 84:147-150, 2012.

[76] N.C. Vega, O. Marin, E. Tosi, G. Grinblat, E. Mosquera, M.S. Moreno, M. Tirado, and D. Comedi. The shell effect on the room temperature photoluminescence from ZnO/MgO core/shell nanowires: exciton-phonon coupling and strain. *Nanotechnology*, 28(27):275702, 2017.

[77] G. Grinblat, F. Bern, J. Barzola-Quiquia, M. Tirado, D. Comedi, and P. Esquinazi, Luminescence and electrical properties of single ZnO/MgO core-shell nanowires. *Appl. Phys. Lett.*, 104:103113, 2014.

[78] C.Y. Liu, H.Y. Xu, J.G. Ma, X.H. Li, X.T. Zhang, Y.C. Liu, and R. Mu. Electrically pumped near-ultraviolet lasing from ZnO/MgO core/shell nanowires. *Appl. Phys. Lett.*, 99(6):063115, 2011.

[79] Z.F. Shi, Y.T Zhang, X.J. Cui, S.W. Zhuang, B. Wu, X.W. Chu, X. Dong, B.L. Zhang, and G.T. Duab. Photoluminescence performance enhancement of ZnO/MgO heterostructured nanowires and their applications in ultraviolet laser diodes. *Phys. Chem. Chem. Phys.*, 17(21):13813-13820, 2015.

[80] J.-P. Richters, T. Voss, D.S. Kim, R. Scholz, and M. Zacharias. Enhanced surface-excitonic emission in ZnO/Al$_2$O$_3$ core-shell nanowires. *Nanotechnology*, 19(30):305202, 2008.

[81] D. Bozyigit, N. Yazdani, M. Yarema, O. Yarema, W.M.M. Lin, S. Volk, K. Vuttivorakulchai, M. Luisier, F. Juranyi, and V. Wood. Soft surfaces of nanomaterials enable strong phonon interactions. *Nature*, 531(7596):618-622, 2016.

Bios

Oscar Marin

Oscar Marin graduated as Chemist at the University of Quindío (Colombia) in 2007 and as Doctor in Chemistry at the National University of the Littoral (Argentina) in 2013 with scholarships from ANPCyT and CONICET. He obtained a postdoctoral scholarship from CONICET in 2013 and joined the Nanoproject group at the National University of Tucumán (Argentina). He moved to the University of Chile in 2015 to lead a postdoctoral project funded by Fondecyt, and returned to Argentina in 2017 to become a researcher of CONICET. His research interests include the synthesis, characterization and applications of nanostructured materials, mainly semiconductors.

Silvina C. Real

Silvina Real is Associate Professor at the National University of Tucumán (UNT), Argentina and a researcher in the Nanoproject Group, INFINOA, CONICET-UNT. She received her PhD in Exact Sciences and Engineering in 2017 at UNT, with a thesis in Physics directed by Mónica Tirado and David Comedi. Her research topic are nanostructures manufacture by electrophoretic deposition and the application of mathematical models

Nadia Celeste Vega

Nadia Celeste Vega graduated as Physicist (2012) at the National University of Tucumán (UNT), Argentina, where she also obtained her PhD. She is currently a teaching assistant at the Physics Department of that house of studies. Her PhD thesis, about ZnO nanostructures and their applications in optoelectronic devices, was honored with the First Mention by the Jorge Sábato Institute award. Between 2017 and 2019, she was a postdoctoral fellow at INQUINOA (CONICET-UNT). She participated in collaborations and research stays at the University of Oxford (England), UNICAMP (Campinas-Brazil) and ICMAB (Barcelona-Spain). Currently, she is an Assistant Researcher at INFINOA (CONICET-UNT), where she is working on the integration of semiconductor nanostructures in solar cells.

Mónica Tirado

Full Professor at the National University of Tucumán (UNT), Argentina; Independent Researcher of CONICET, director of the Laboratory of Nanomaterial and co-director of the research group NANOPROJECT (INFINOA:CONICET-UNT). She received the award J.J.GIAMBIAGI 2004 for Best Doctoral Thesis in Argentina. She has published over 40 works in international journals and 25 papers in proceedings. She has presented more than 200 research works in national and international congresses. She has supervised 7 Ph. D. students. She spoke at a TEDx talk called "Llegando al Corazón de la Materia" (2015). Her main research topic is the manufacture and characterization of semiconductor nanostructures to obtain nanodevice prototypes.

David Comedi

David Comedi obtained his PhD in Physics in 1990 at the Israel Institute of Technology, Technion, and completed his postdoctoral work at the Centre for Electrophotonic Materials and Devices, McMaster University, Canada. After many years as Professor of Physics at UNICAMP, Brazil, he was repatriated in 2006 by CONICET as an Independent Investigator working at the National University of Tucumán (UNT). Currently, he is a Principal Investigator of CONICET, Associate Professor at the Physics Department of UNT, Director of the NanoProject group and Head of the Physics Institute of Northwestern Argentina (INFINOA-CONICET/UNT). His scientific contributions are focused on the fields of ion-solid interactions and semiconductor nanotechnology

Nanomaterials as Photothermal Agents for Biomedical Applications

Antonia Cuello,[1] Silvestre Bongiovanni Abel,[2] César A. Barbero,[1] Inés Yslas,[1] and María Molina[1]*

[1] Instituto de Investigaciones en Tecnologías Energéticas y Materiales Avanzados (IITEMA), Fac. Ciencias Exactas Fisicoquímicas y Naturales, Universidad Nacional de Río Cuarto (UNRC)-Consejo Nacional de Investigaciones Científicas y Técnicas (CONICET), Río Cuarto, Argentina.
[2] Instituto de Investigaciones en Ciencia y Tecnología de Materiales (INTEMA), Universidad Nacional de Mar del Plata (UNMdP)-Consejo Nacional de Investigaciones Científicas y Técnicas (CONICET), Mar del Plata, Argentina.
* Corresponding author. E-mail: mamolina7@gmail.com

Abstract

Photothermal therapy (PTT) is a potentially curative treatment modality that in recent years has been the object of growing interest and rapid technological advances due to its specific therapeutic efficacy and because it is a non-invasive technique. Nowadays, several nanomaterials have been developed as photothermal agents including metallic and carbon-based nanoparticles, conducting polymers, and different kinds of nanocomposites, among others. In this article, the most relevant applications of these photothermal nano-agents in antibacterial and anticancer therapy are reviewed.

Keywords:
photothermal nanoagents, PTT, antibacterial therapy, anticancer therapy

Introduction

Photothermal therapy (PTT) is an alternative treatment to conventional therapies that lately has been the object of increasing interest in the scientific community. This is due to its specific therapeutic efficacy, since it is a non-invasive technique and has the potential for combination in the same approach diagnosis and therapy (Millenbaugh *et al.* 2015). PTT is based on the use of photothermal agents that absorb radiation in the near infrared (NIR) region and convert the absorbed energy into heat through a non-radiative mechanism without oxygen consumption. Therefore, PTT requires the use of nanomaterials that exhibit high absorption in the NIR region of the electromagnetic spectrum. NIR absorbing nanomaterials are promising agents for PTT, allowing application deep in the tissue. Human tissue has almost no absorption of NIR radiation, while other body constituents, such as hemoglobin and water, have minimal absorption (Weissleder 2001). The advantage of using nanomaterials is that the light absorbed can be rapidly converted into heat, greatly increasing the temperature of the irradiated zone, which heats up the whole organ, avoiding the drawback of macroscopic hyperthermia (Zhou *et al.* 2018). The amount of heat induced by NIR irradiation is related to different parameters, namely, NIR light intensity, irradiation time, and the concentration of the photothermally active nanomaterials. Nanoparticles under irradiation scatter some of the photons and absorb the others. The energy produced by the absorbed photons can be released in two ways – photon emission or phonon emission. The emission of phonons generates heat. To obtain a good candidate for PTT therapies, nanoparticles need to show large absorption efficiencies and low luminescence quantum yields. This is what will ensure a large photothermal conversion efficiency.

It was reported that temperatures greater than 41°C inhibit cell proliferation and mobility, which, in turn, can increase permeability, trigger cell wall damage and increase cellular lysis (Tsuchido *et al.* 1985). Intracellular temperature causes irreversible cellular damage, such as denaturation of cell proteins/enzymes, and, therefore, interferes in essential intra-cellular reactions, leading to the death of cells in a rapid and effective manner. In addition, damage to the DNA structure is triggered, causing genotoxic effects that include breakage of the DNA strand and disruption of the chromosomal cell membrane (Jia *et al.* 2017, Korupalli *et al.* 2017, Wu *et al.* 2013). The heat generated by NIR exposition also could break the cell membrane. Additionally, some researchers even predict NIR-light-triggered therapy platforms to be an innovative and exciting possibility for clinical nanomedicine applications.

This review focuses on the latest progress and future development trends in the applications of nanomaterials as photothermal agents for biological applications, with special emphasis in antibacterial and anticancer therapy (Figure 1). We review the use of nanomaterials as photothermal absorbers, including metallic and carbon-based nanoparticles, nano-composites and conductive polymers.
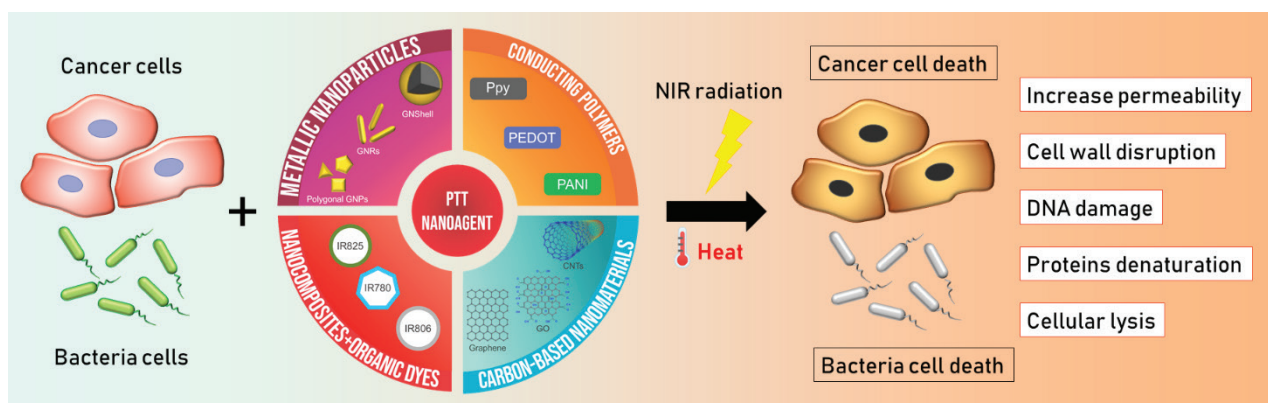

Figure 1. Different nanomaterials as photothermal agents for biological applications.

1. Progress on utilizing tremendous potential PTT for mitigating bacterial infections

Infectious diseases caused by bacteria are a problem that has potentially catastrophic global consequences related to health. In recent decades, the emergence of bacteria resistant to multiple antibiotics has become a common cause of infectious diseases due to overprescribing and indiscriminate use of antibiotics (World Health Organization 2014). The proportion of antibiotics-resistant bacterial isolates has been alarmingly increasing through the intrinsic and acquired mechanisms of antimicrobial resistance (Andersson *et al.* 2010). The problem of antibiotic-resistant bacteria and the high costs of medical care encourages researchers to come up with innovative approaches to develop more effective antibacterial agents that overcome bacterial resistance and reduce costs. Thus, there is an urgent need to develop novel antibacterial agents and therapies to combat pathogens in a safer and more effective way (Zharov *et al.* 2006).

It is well known that most pathogenic bacteria die at temperatures above 40°C (Mackowiak 1981). Therefore, the PTT approach has been widely applied as bacteria-killing mechanism for the last few years. Recently, He *et al. (*He *et al. 2018)* designed an antimicrobial hybrid based on polydopamine (PDA)-coated gold nanorods (PDA@GNRs) grafted with gly-col chitosan (GCS-PDA@GNRs) and loaded with daptomycin (DAP-GCS-PDA@GNRs) which improves antibacterial activity and reduces side effects *in vivo*. This hybrid material showed an outstanding chemo-photothermal synergistic therapeutic effect on the abscess, leading to sufficient bacteria eradication that could thoroughly ablate abscess while reducing the damage to normal tissue, accelerating wound healing. Khan *et al.* reported the synergistic biocide effect of graphene oxide (GO) and Nd-YAG laser for antibacterial and antifungal treatments (Shahnawaz Khan *et al.* 2015). The authors suggest that this will serve as a novel and promising therapeutic strategy and has great potential to serve for PTT against pathogenic microorganisms. It was also reported that GO offered high efficiency for photothermal treatment (Pereyra *et al.* 2018, Wu *et al.* 2013). The combination of PTT with pharmacotherapy can not only significantly improve the antibacterial efficiency towards drug-resistant bacteria, but also readily reduce antibiotic dosage, thus providing a potential solution to the problems of drug-resistant bacteria.

Other authors have shown that during the treatment with a PTT agent, as a result of a thermal shock, an excess of reactive oxygen species (ROS) could be produced. Thus, ROS can cause protein or lipids damage leading to cell death. ROS are generally well defined as containing oxygen and active chemical substances, and usually are classified as one of two

kinds: free radicals and nonradicals (Birben *et al.* 2012). ROS that are commonly observed in biological systems include hydroxyl radicals, superoxide, and nitric oxide, ozone, hydroxide, peroxynitrite, and hydrogen peroxide.

Bacteria that adhere to surfaces of materials or tissues have the tendency to encase themselves in a hydrated matrix, forming a layer known as biofilm that is made of a bacterial community embedded in a self-produced matrix of extra-cellular polymeric substances (EPS) (Singh *et al.* 2017). More than 80% of human infectious diseases are related to the formation of biofilms. Bacterial biofilms act as a barrier to prevent the penetration of antibiotics in bacterial cells; therefore, it is generally not effective to destroy such biofilms, which can also generate resistance to antimicrobial agents and result in antibiotic treatment failure. Other scientists have applied PTT to disrupt the biofilm structure by physical effects of the heat that is generated by light absorption of materials without giving rise to drug-resistance of pathogenic bacteria (Tan *et al.* 2018, Zhao *et al.* 2017). Therefore, water may be eventually removed from the biofilm causing dehydration and as consequence, the death of the pathogens, triggering denaturation of the cell wall and protein/enzymes, leading to the leakage of cellular content and bacterial death. (Figure 2).
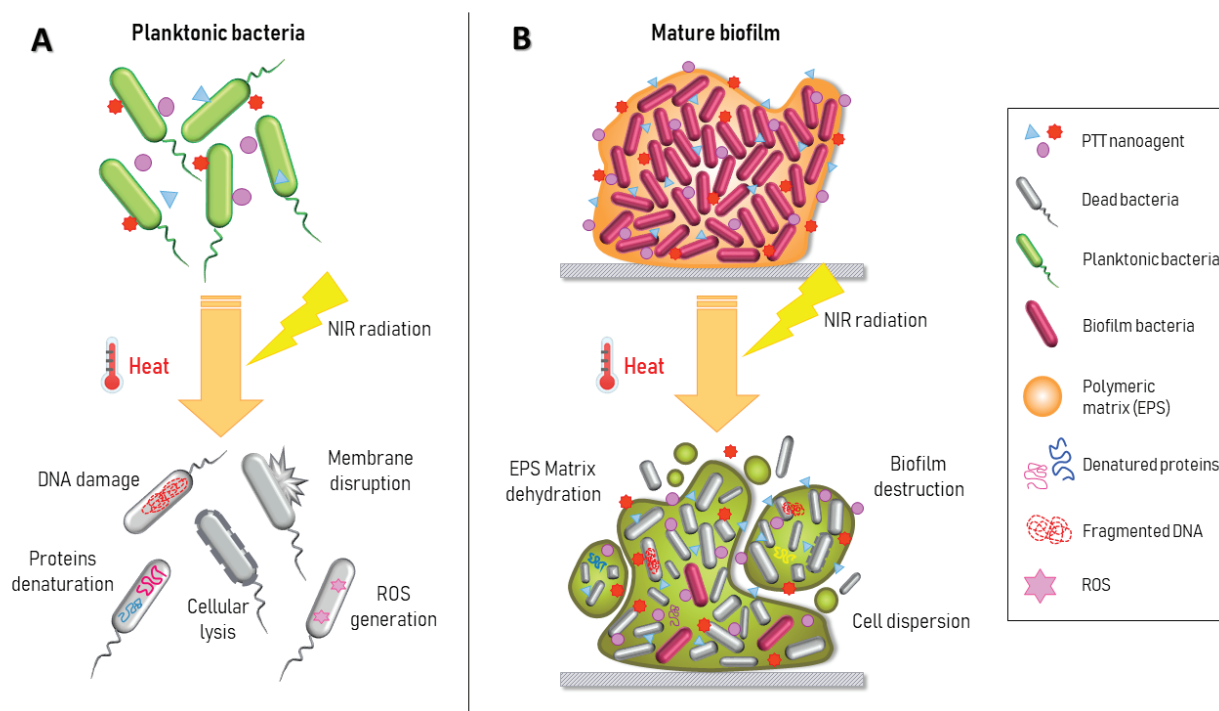

Figure 2. Schematic representation of the possible mechanism of nanomaterials in combination with NIR irradiation for effectively killing planktonic bacteria **(A)** and for destroying bacterial biofilms **(B)** using PTT.

2. PTT for anticancer therapy

Cancer is one of the leading causes of death worldwide, and traditional therapies have enormous drawbacks including side effects and the development of resistance of the cells to the conventional drugs (Housman *et al.* 2014). That is why PTT is an attractive alternative anticancer therapy, since it can provoke cell death via protein denaturation and the subsequent tumor regression with minimal invasion and almost no side effects (Chen *et al.* 2018).

However, to treat tumors that are not at the surface, the activating energy source needs to penetrate tissues, efficiently kill tumors and not damage healthy tissues. Thus, there is an urgent need of looking for nanoagents with high photothermal efficiency that can target tumor cells. In the last years, thermal therapies for treating cancer have received great attention using different heating sources such as laser, focused ultrasound, and microwaves. More interestingly, PTT using NIR induces minimal damage in both tumors and healthy tissues. Thus, there is an increasing interest in developing photothermal nanoagents capable to absorb NIR light and transduce it to heat in order to kill the malignant cells without damaging the surrounding healthy tissues (Wang *et al.* 2016). Several photoactive nanomaterials such as magnetic nanomaterials, carbon nanotubes, or gold nanoparticles, activated with NIR radiation, have proven to be effective in PTT treatment of various cancers (Cheng *et al.* 2014). Additionally, PTT in combination with other therapies, such as chemotherapy (Cao *et al.* 2017), or even other phototherapies, such as photodynamic therapy (PDT) (Liu *et al.* 2018, Wang *et al.* 2017), has gained great attention for increasing treatment efficacy. Furthermore, the combination of PTT with imaging is a new trend to develop theranostic systems for cancer therapy (Jung *et al.* 2018).

3. Nanomaterials as photothermal agents

PTT has been introduced as a potent alternative therapeutic modality against drug-resistant bacterial infections, as well as against drug resistant cancer cells. So far, numerous photothermal nanoagents with strong NIR absorption have been explored for PTT, including gold nanorods, nanoshells, nanocages, nanostars, copper selenide nanoparticles, carbonous nanostructures (graphene oxide (GO), carbon nanotubes (CNTs)) and polymeric nanoparticles (Jaque *et al.* 2014). In fact, advances in nanomedicine have recently allowed us to manufacture multifunctional nanoparticles that offer diagnostic and therapeutic functions in a single environment (Menon *et al.* 2013). In PTT, within a few minutes upon NIR radiation, temperature rises locally due to the heat generation caused by the photothermal agents, which results in irreversible cell damage by hyperthermia effect. This hyperthermia process is triggered by applying pulses of light directly on the infected location, which causes tissue temperature to increase because it absorbs the energy of the light, releasing it as heat.

3.1. Conducting polymers

Conducting polymers exhibit conjugation in their molecular structure due to the presence of a π-electrons system delocalized over the whole polymeric main chain. Additionally, the presence of delocalized charges in the chains render them electrically conductive. However, NIR light absorption in conjugated polymers is related to the presence of low-energy (< 1.58 eV) electronic transitions. Therefore, all conjugated polymers, which can be conducting or semiconducting, could show NIR light absorption. The low cost, stability, biocompatibility, high biodegradability and versatility of conducting polymers allow using them on photothermal processes and therapy treatments. Under light irradiation, the polymer absorbs the energy and transforms it into localized heat that can be useful for generating a hyperthermia process in living systems (Chen *et al.* 2018, Pierini *et al.* 2018). Polyaniline (PANI), polypyrrole (PPy), and poly-(3,4-ethylenedioxythiophene) (PEDOT) are the most important conducting polymers studied for photothermal treatments. In this section, the most relevant and promising nanomaterials and composites based on these and other conducting polymers for PTT applications are described.

Taking into account the synthetic approach reported by Stejskal and coworkers (Stejskal *et al.* 2005), PANI nanoparticles stabilized with polyvinylpyrrolidone (PVP) as a hydrophilic agent were obtained by oxidative polymerization of the monomer salt. Spherical particles of c.a. 200 nm were obtained and fully characterized by several microscopic, light dispersion, and spectroscopic techniques. *In vitro* experiments revealed the successful incorporation of the nanoparticles into the cells, showing no cytotoxicity at high concentrations and unaltered morphology. The destruction of LM2 tumoral cells was achieved by combining the conducting nanoparticles with laser irradiation using NIR light at low power (Yslas *et al.* 2015). Furthermore, *in vivo* assays on an animal model were carried out using the same PANI nanoparticles. In this case, the tumors were injected with the nanomaterial and irradiated during 15 minutes with the same NIR light that was used for the *in vitro* experiments (785 nm, power density of 500 mW cm^{-2}). Results have shown that tumoral growth was inhibited after PTT with a significant reduction of tumor volume, suggesting that the efficient nanoparticles for PTT are a promising agent for anticancer clinical treatments (Ibarra *et al.* 2013). The same PANI nanoparticles generated by oxidative polymerization were also used to explore the antibacterial photothermal effect under *Pseudomonas aeruginosa (P. aeruginosa)*, one of the most important pathogenic bacteria that causes nosocomial infections. The nanomaterials showed a synergistic effect between nanoparticles and NIR light (Bongiovanni Abel *et al.* 2018). In this sense, *P. aeruginosa* colony viability was reduced by more than 80% after irradiating for 15 minutes the bacteria exposed to the nanoparticles, demonstrating that the nanomaterial is an effective photothermal agent capable of inhibiting cellular growth for this bacteria type. The DNA fragmentation in the microorganism exposed to NIR light supports the mechanism of cell death. The authors revealed that the nanomaterial has a PTT effect similar or comparable to that of other materials (e.g. metal nanoparticles).

PANI nanoparticles stabilized with a thermosensitive polymer (PNIPAm) in combination with PVP were synthesized and the photothermal effect was evaluated (Bongiovanni Abel *et al.* 2014). To simulate the environment of the tumoral cell, where pH is lower and the temperature is higher than normal physiological conditions, assays were carried out in acidic media. After NIR laser irradiation, under similar conditions as those used by Ibarra *et al*. (Ibarra *et al.* 2013), a high transmittance decrease of the dispersion was observed in only 6 minutes, indicating the collapse of the PNIPAm stabilizer by the heating of the conducting polymer. Thermosensitive polymer chain aggregation was measured by turbidimetric techniques, resulting close to the LCST (32 °C). The photothermal effect was dependent on nanoparticle concentration, reaching a temperature increment of 13 °C on PANI nanoparticles irradiated for 10 minutes. The thermosensitive properties of PANI/PNIPAm nanoparticles could be useful due to the formation, under heating, of polymeric aggregates that show a reversible behavior. Additionally, another novel method for obtaining PANI nanoparticles was recently reported by Bongiovanni Abel *et al.* (Bongiovanni Abel *et al.* 2018). Multifunctional PANI particles of controlled size and new properties, such as fluorescence, were obtained. First, the conducting polymer was chemically modified in order to add the fluorophore (dansyl chloride). After that, nanoparticles were formed using the solvent displacement method, which yielded monodisperse nanoparticles with a size of c.a. 104 nm. The photothermal effect by application of NIR light was tested

on nanoparticle dispersion, irradiating for 10 minutes. An increment of the local temperature was registered, reaching a total difference of 8 °C. The antibacterial PTT was also evaluated, inhibiting cellular growth in *P. aeruginosa*. However, in this case, the toxicity of the organic solvent (N-methylpyrrolidone) needs to be considered.

On the other hand, Calderón and coworkers obtained dendritic nanogels containing conducting polymers by semi-interpenetration (PNIPAm-dPG/PANI NGs) and studied their performance as *in vivo* PTT agent on tumoral cells (Molina *et al.* 2016). The nanoparticles exhibited diameters between 150-240 nm depending on the temperature of the media and showed spherical morphology. The resulting temperature increment depended on nanocomposite concentration and time of exposure under the irradiation. At higher concentrations (80 μg mL^{-1}), the temperature increase reached c.a. 20 °C, demonstrating the efectiveness for their use as a potential photothermal agent. *In vitro* assays using A2780 cells revealed a markedly reduced viability upon NIR irradiation (785 nm). Additionally, *in vivo* experiments in mice with transplanted A2780 tumor showed a significant reduction of tumor volume under NIR laser at 500 mW power for 5 minutes. Evaluation at different times after injection of nanocomposites and irradiation allowed significant tumor growth inhibition, showing treatment efficacy.

As mentioned above, PPy is another one of the most used conducting polymers to generate a photothermal effect. Some works have shown the efficacy of this material for this application in living systems. For example, hollow PPy microspheres (PPyHMs) generated by one-step oil-water microemulsion method in an aqueous solution containing PVP was synthesized by Zha *et al.* (Zha *et al.* 2013). They have shown that it is possible to combine the photothermal activity of the conducting polymer with ultrasound imaging for evaluating the material as theranostic agent. Tumor ablation was successful, taking advantage of the strong absorption of PPy in the NIR therapeutic window. An increment of c.a. 30 °C was measured in a concentration of 150 μg mL^{-1} of the spherical dispersible particles (Figure 3). Moreover, *in vivo* ultrasound imaging facilitated the evaluation of PPy nanoparticles in a mouse model with tumor, showing excellent photothermal conversion efficiency by applying 0.64 W cm^{-2} laser power and easy identification of the particle location into the tumor. The same authors reported similar results with uniform PPy nanoparticles, where the stabilizer used was polyvinyl alcohol (PVA) and FeCl$_3$ was employed as an oxidizing agent in the synthetic approach to obtain nanospheres with an average diameter of ≈ 46 nm. Photothermal assays were made in a RPMI-1640 culture medium in the presence of conducting particles, and results revealed that temperature could be increased up to 34.5 °C after 10 minutes of NIR irradiation (808 nm, 2 W) for 10 minutes. A concentration-dependent effect was also observed in this case. *In vitro* studies confirmed good material photostability and biocompatibility, showing PTT ablation on HeLa cells (Zha *et al.* 2013). Wang *et al.* reported the application of PPy nanoparticles with a layer of natural red blood cell (RBC) on the surface for local heating generation. A comparison between PPy NPs, PPy-PEG NPs, and PPy@RBC NPs was made in order to find strategies that allow minimizing the dosage of nanoparticles into the living system. The three kinds of nanoparticles were tested as PTT agents on HCT116 cells at concentrations between 0-40 μg mL^{-1} by applying NIR light with power density between 0.75-1.50 W cm^{-2} for 3 minutes, repeating three cycles in each case. A three-factor dependence was found in the hyperthermia treatment: concentration, exposure time, and light power. The best performance was observed with PPy@RBC NPs: 53.2 °C increment in temperature at 40 μg mL^{-1}, 1.50 W cm^{-2}, and 180 seconds of laser irradiation, showing, photothermal conversion efficiency close to 40%. Additionally, nude male mice were used to try the *in vivo* PTT, concluding that a low-dose of PPy@RBC NPs can be sufficient to observe tumor ablation (Wang *et al.* 2017).
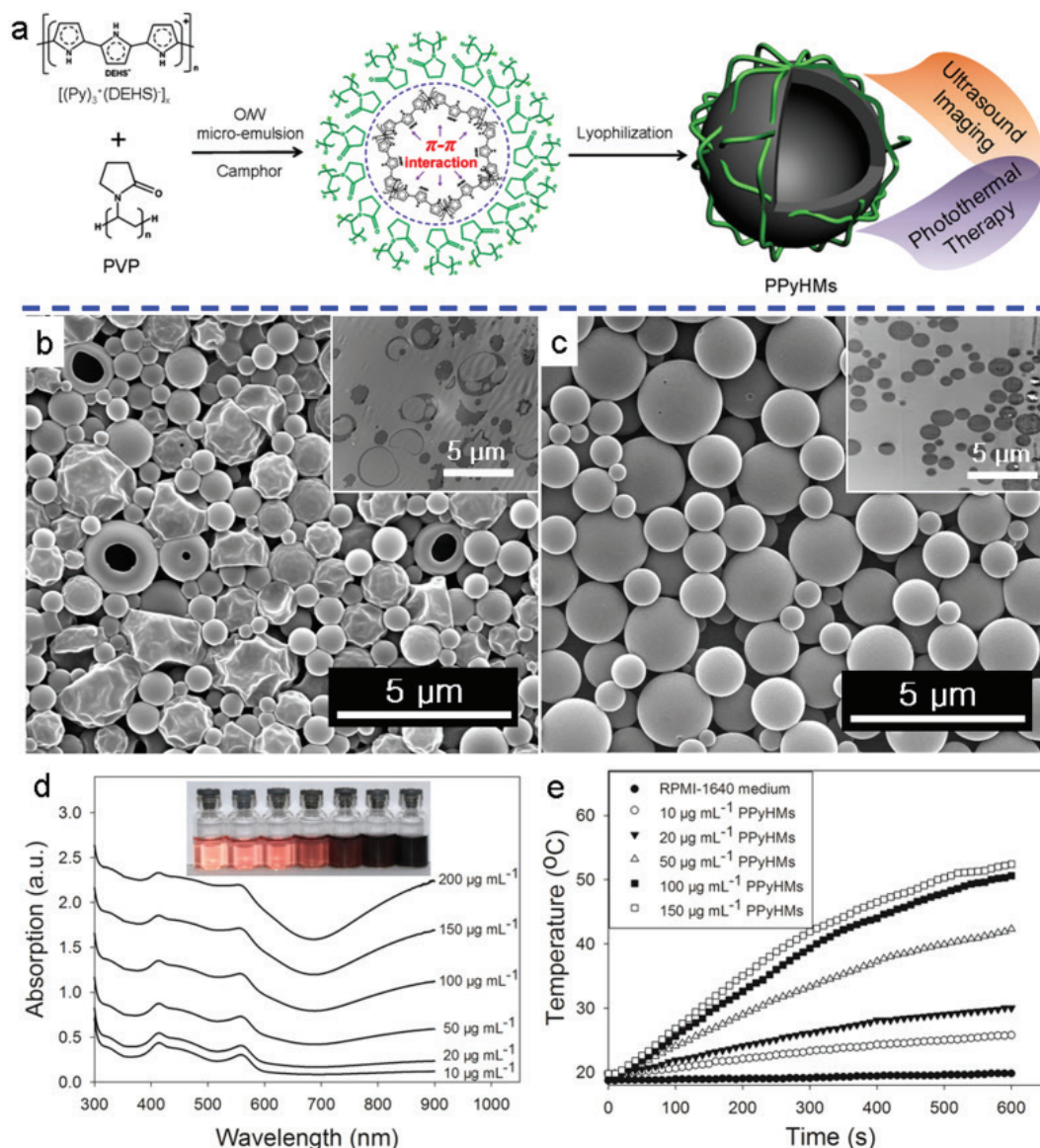
Figure 3. Preparation and characterization of water-dispersible PPyHMs. **(a)** Schematic illustration of echogenic PPyHMs formation for combined US imaging and PTT via a facile O/W microemulsion method; SEM and ultrathin-section TEM images of obtained PPyHMs with **(b)** PVP and **(c)** PVA as stabilizers; **(d)** UV-vis-NIR spectra of various concentrations PPyHMs dispersed in RPMI-1640 culture medium, inset was the photograph for various concentrations of PPyHMs dispersed in RPMI-1640 culture medium, indicating good dispersibility; **(e)** Heating curves of PPyHMs in RPMI-1640 culture medium at different concentrations under 808 nm laser irradiation. Reproduced with permission from reference (Zha *et al.* 2013) which is licensed under a Creative Commons Attribution-NonCommercial-NoDerivs 3.0 Unported License.

In recent years, PEDOT:PSS has been studied and proposed as a photothermal agent. Liu and coworkers synthesized poly-(3,4-ethylenedioxythiophene):poly(4-styrenesulfonate) (PEDOT:PSS) nanoparticles that exhibit uniform spherical shape (Cheng *et al.* 2012). PEGylation was used as a technique to facilitate the incorporation on biological systems. The high optical absorption allowed irradiation at 808 nm using low laser power density. The authors highlighted the good photostability of the nanomaterial, compared with typical metal nanoparticles. *In vivo* experiments were carried out by employing Balb/c mice as animal model for PTT, showing excellent therapeutic efficacy. A recent work, showed the synthesis of poly(diethyl-4,4′-{[2,5-bis(2,3-dihydrothieno[3,4-b][1,4]dioxin-5-yl)-1,4-phenylene] bis(oxy)}dibutanoate) (P1) and poly(3,4-ethylenedioxythiophene) (PEDOT) nanoparticles where 4-dodecylbenzenesulfonic acid and poly(4-styrenesulfonic acid-co-maleic acid) are used as stabilizers (Cantu *et al.* 2017). Particles with an average size of 100 nm were obtained by the two-surfactant emulsion polymerization method. An exhaustive study based on the effect of nanoparticles concentration on PTT activity was carried out. Laser power was fixed on 0.56 W (2.0 W cm^{-2}), and laser irradiation wavelength was 808 nm. Both kinds of nanoparticles studied in this work present important absorption peaks

in the NIR region of the electromagnetic spectra. In a concentration range between 10–500 μg mL^{-1}, the PTT effect was corroborated in both cases, showing a significant increase in local temperature (~35-40°C), with a linear relationship between nanomaterial concentration and temperature. Moreover, the photostability of the dispersions allowed the repetition of irradiation cycles (Figure 4). Photothermal conversion efficiency for both kinds of nanoparticles was estimated at ~ 50%. The materials were successfully tried as agents for laser-induced PTT, showing complete cell ablation achieved by the generation of local heat capable to cause the death of MDA-MB-231 cells at low concentrations (c.a. 10 μg mL^{-1}).
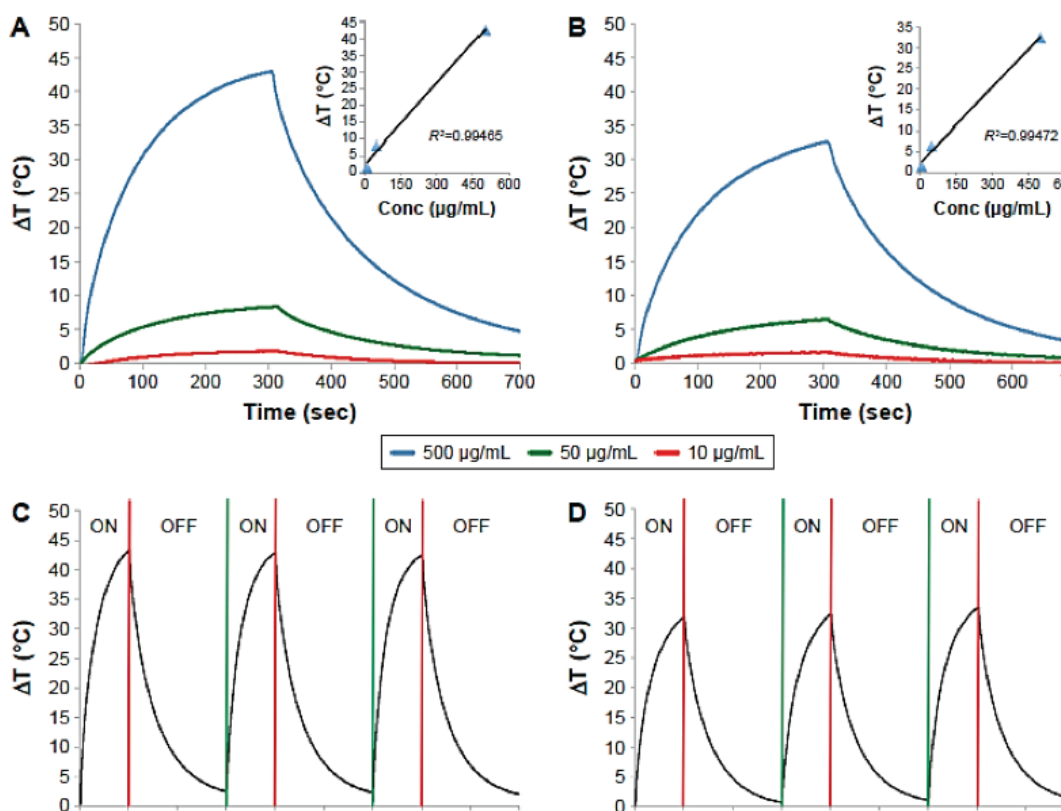

Figure 4. Temperature (T) changes in P1-PMD (A) and PEDOT-PMD (B) NPs at three different concentrations upon irradiation with 808-nm laser at 2 W cm^{-2} for 5 min followed by cooling in the absence of irradiation. Cycled laser-mediated irradiation (ON) and cooling in the absence of irradiation (OFF) for P1-PMD (C) and PEDOT-PMD (D) NP suspensions. Abbreviations: NPs, nanoparticle; P1, poly(diethyl-4,4'- (Zha *et al.* 2013-b][1,4]dioxin-5-yl)-1,4-phenylene] bis(oxy)) dibutanoate); PEDOT, poly(3,4-ethylenedioxythiophene); DBSA, 4-dodecylbenzenesulfonic acid; PSS-co-MA, poly(4-styrenesulfonic acid-co-maleic acid); P1-PMD, P1:PSS-co-MA:DBSA; PEDOT-PMD, PEDOT:PSS-co-MA:DBSA. Reproduced with permission from reference (Cantu *et al.* 2017) which is licensed under a Creative Commons Attribution - Non Commercial (unported, v3.0) License.

    Composite and nanocomposite materials are nowadays flourishing as potential PPT agents. In this way, different materials have been used for PTT applications combining conducting polymers with other kinds of nanostructures or components, such as biopolymers, metals, and carbon-based materials. For example, gold nanorods combined with poly(o-methoxyaniline) (GNRs/POMA) were reported as a promising material. In this synthetic approach, POMA acts as a coating on the nanogold surface, resulting in a kind of core-shell particle. The conducting polymer helps improve the PTT conversion efficiency of the metal particles. In this way, authors demonstrated the photothermal effect of these hybrid materials by exposition under NIR laser at a power of 3.0 W cm^{-2}, performing six cycles of irradiation. Colon cancer CT26 cells were employed for *in vitro* experiments, showing a significant increase of photothermal efficiency when the polymeric shell is present compared with the GNRs without POMA. Only 10 minutes of laser irradiation were enough for the destruction of tumoral cells in contact with the composite. Besides, typical *in vivo* assays employing female Balb/c mice were carried out, regarding a successful tumor elimination by using GNRs/POMA core/shell hybrids (Wang *et al.* 2018). Combining PANI with GO (GO@PANI), PTT nanoagents were obtained as nanosheets hybrids with nanorod array. Under typical conditions of NIR irradiation using a spot size 1 cm long and 0.5 cm wide, the results have shown temperature increasing higher than 20 °C after 700 seconds, with a conversion efficiency close to 50%. This parameter was estimated at 26% when PANI is not present in the GO system (Fan *et al.* 2019). Other examples containing PANI for

applications in antibacterial PTT were summarized by Xu *et al.*, including, among others, NMPA-CS micelles and PANI/PVP composites (*Xu et al.* 2019). Recently, poly (3,4-ethylenedioxythiophene):poly(styrene-sulfonate)/agarose nanocomposites were obtained by Ko *et al.* as antibacterial photothermal materials as hydrogel using a simple synthetic method. *Escherichia coli (E. coli)* and *Staphylococcus aureus (S. aureus)* were the bacteria chosen for the antibacterial PTT tests (Ko *et al.* 2019). The bactericidal action was evaluated at different times in both cases. Under only 1 minute of exposition to NIR light (power 2 W cm^2), the viability of *E. coli* decreased to 44%. In the case of *S. aureus*, viability was reduced to 37% compared to the original colonies. Additionally, in 2 minutes under the same power laser at 808 nm, both bacteria were totally killed, demonstrating the excellent antibacterial effect of the nanocomposites.

Furthermore, in recent years, a new trend is focusing on nanosystems that exhibit a combined effect of different phototherapies (Pierini *et al.* 2018). As a result, the effect of PTT and photodynamic therapeutic (PDT) combined were explored by using conducting polymers composites. Poly(pyrrole-3-carboxylic acid) (PPyCOOH) nanoneedles were generated in order to act as an agent on dual-imaging guided PDT/PTT combination therapy. The final material resulted in the complex PPyCOOH nanoneedles modified with poly(allylamine hydrochloride) (PAH) and poly(acrylic acid) (PAA) and loaded with the photosensitizer aluminum phthalocyanine tetrasulfonate (AlPCS$_4$) (AlPCS4@PPyCONH-PAH-PAA). Nanoneedle therapeutic performance was highly superior to that reached by nanospheres. The fluorescent properties allowed guiding the nanomaterial used for PDT/PTT chemotherapy on *in vitro* and *in vivo* assays (Liu *et al.* 2018). Using the same conducting polymer (PPy) but combined with bismuth, a multifunctional nanocomposite was synthesized as a core-shell hybrid by Yang *et al.* for anticancer treatment (Yang *et al.* 2018). *In vitro* and *in vivo* assays demonstrated a highly effective photothermal ablation on cancer cells that can be combined with computed tomography and photoacoustic dual modal imaging in order to improve the diagnosis. Cao *et al.* developed a system that presents photoacoustic imaging (PAI)-guided photothermal/chemotherapy (Cao *et al.* 2017). Diketopyrrolopyrrole-based polymers (DPP) were designed by combining donor-acceptor moieties. Encapsulation of doxorubicin (DOX) and DPP in tocopherol polyethylene-glycol-succinate-cholesterol (TPGS-CHO) copolymers were made in order to generate the theranostic platform for cancer treatment. NIR-II photothermal nanoagents based on a conjugated polymer (TBDOPV-DT) with 2,2-bithiophene as the donor and thiophene-fused benzodifurandione-based oligo(p-phenylenevinylene) as the acceptor were produced by nanoprecipitation and reported by Sun *et al (*Sun *et al. 2018)*. Their study showed the application of composite nanoparticles for PAI and PTT. Under 1064 nm (NIR-II) laser irradiation, a 50% efficiency in PTT conversion was successfully achieved. The material is promissory for tumoral treatments considering the effect of PTT and the ability of PAI for imaging guiding.

3.2. Metallic nanoparticles

In the past decades, nanoparticles have been exploited in many biomedical applications (Thota *et al.* 2018), some of which have paid special attention to noble metal nanoparticles applied in PTT, especially gold (Au) nanoparticles (Boisselier *et al.* 2009). This is a consequence of their unique optical and photothermal properties, including strong optical absorption and a relatively high photothermal conversion efficiency, showing great photostability. However, other metallic nanoparticles have also been investigated as photothermal agents: palladium nanoparticles, silver nanotriangles, and copper nanoparticles.

Undoubtedly, gold nanoparticles are one the most studied and applied nanomaterials in PTT, mainly because of their simple synthesis and surface modification process, the varied forms that can be manufactured, and their biocompatibility. Simple spherical Au nanoparticles have been widely studied but offer very limited tunability of their "localized surface plasmon resonance" (LSPR) frequency. While a red shift of LSPR is possible, it has been shown that changing the size of Au nanospheres from 9 nm to 99 nm only changes LSPR from 520 to 580 nm (Link *et al.* 1999). Therefore, none are suitable for NIR applications. However, nanoparticle shape has also a strong influence on the LSPR effect, and LSPR could be shifted to the NIR region by producing metallic nanoparticles with non-spherical shapes such as nanorods, nanocages, nanoshells, nanostars, and even nanobipyramids (Lombardi *et al.* 2012, Wang *et al.* 2013). The development of these different gold nanomaterials allowed achieving photothermal performance by simply tuning the LSPR by changing nanomaterial shap.

Among the mentioned non-spherical gold nanoparticles, nanorods (GNRs) have attracted a great deal of attention due to the large number of synthesis methods available, the high achievable monodispersity, and the rational control over the aspect ratio (length vs. diameter), which is primarily responsible for the change in their optical properties. GNRs have two characteristic optical absorptions, transversal and longitudinal, linked to rod the diameter and lengt, respectively. In GNRs spectra (Figure 5a), it can be seen how the LSPR band is split into two bands – a strong band in the NIR region, corresponding to electron oscillations along the long axis (longitudinal band), and a weak band in the visible region at a wavelength similar to that of gold nanospheres (transversal bands). Link *et al.* studied the relationship between the absorption maximum in the longitudinal band and particle aspect ratio (Link *et al.* 2005). According to their research, the

transversal band is insensitive to size changes, whereas the longitudinal band is red-shifted largely from the visible to NIR region with increasing aspect ratios (length/width), causing the color changes from blue to red (Figure 5b). Currently, aspect ratio can be precisely controlled by changing experimental parameters such as the catalyst of silver ions in the seed-mediated growth method (Nikoobakht *et al.* 2003).
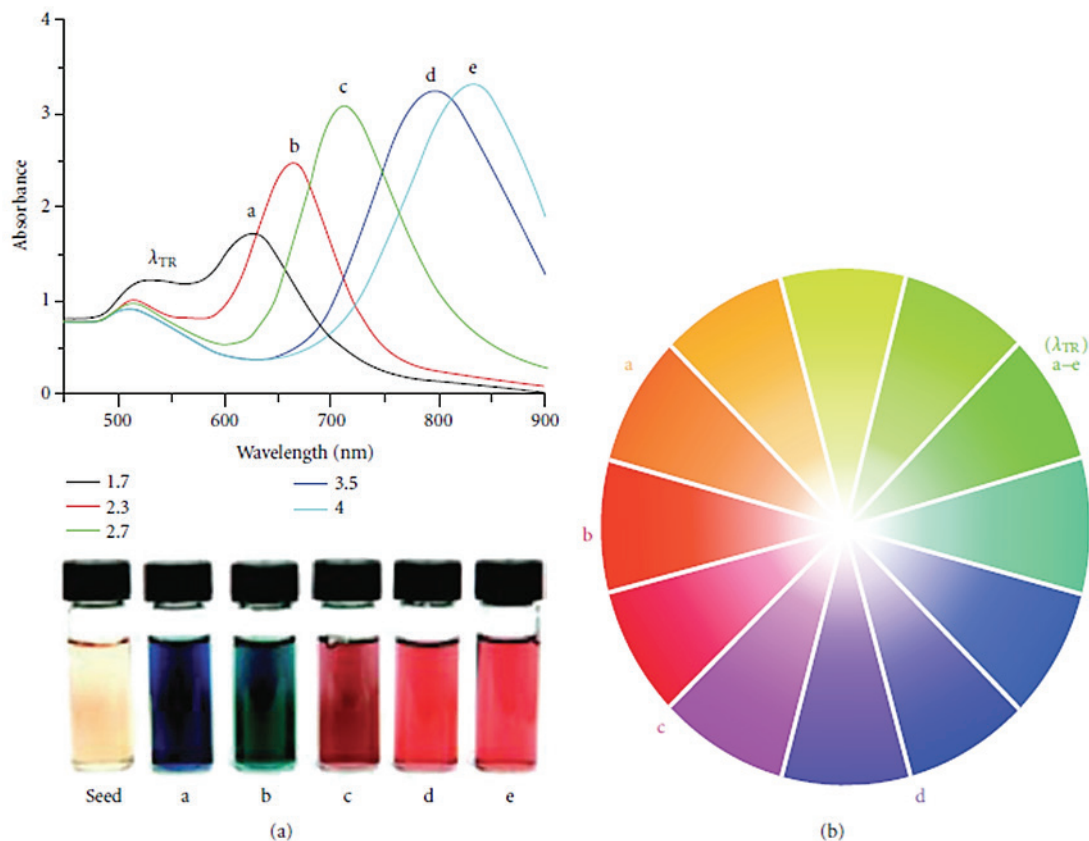

Figure 5. Tunable optical properties of gold nanorods (AuNRs) with absorptions at visible and near-infrared wavelengths region. **(a)** Optical absorption spectra of AuNRs with different aspect ratios and composition (a–e). **(b)** Color wheel representing AuNRs labeled a–e, TR = transverse resonance. Reproduced with permission from reference (Tong *et al.* 2009) with permission from John Wiley and Sons and Copyright Clearance Center.

Nanoshell structures are another example of gold nanoparticles that absorb in the biological window and can be used as PTT agents (Jain *et al.* 2007). In this case, a broad plasmonic extinction band is observed that can be tuned by varying core and shell thickness, as well as total nanoparticle size (Jain *et al.* 2006). Loo *et al.* demonstrated that the plasmonic band shifts to the red when shell thickness decreases (Loo *et al.* 2004).

El-Sayed and coworkers firstly demonstrated the *in vitro* application of gold nanorods in PTT (Huang *et al.* 2006). They studied the binding of the gold nanorods conjugated to anti-epidermal growth factor receptor antibodies, specifically to the malignant epithelial cell lines. After applying the PTT treatment using a Ti:Sapphire laser at 800 nm for 4 minutes, they found that cancer cells required half the laser energy (10 W cm^{-2}) to be photothermally damaged, compared to normal cells (20 W cm^{-2}). This was attributed to the presence of nanoparticles on cell surface. Comparing these results with the ones obtained by Hirsch *et al.* with gold nanoshells (Hirsch *et al.* 2003), where they found that breast carcinoma cells incubated with PEGylated gold nanoshells underwent irreversible photothermal damage after exposure to a NIR laser (820 nm, 35 W cm^{-2}) for 7 minutes, using gold nanorods enables effective treatment at three times lower laser intensity. This is because nanorods exhibit higher absorption efficiency than nanoshells with LSPR at the same wavelength. Thus, it is possible to achieve effective treatment with lower laser intensity using GNRs as photothermal agents.

In addition to the application of PTT for cancer therapies, gold nanoparticles have attracted special attention in researchers who are investigating alternative treatments for bacterial infections, especially those caused by drug-resistant bacteria (Xu *et al.* 2019). Zharov *et al.* proposed that hyperthermia caused by gold-based metallic nanoparticles could be a useful mechanism to kill pathogenic bacteria combining the use of laser and functional gold nanoparticles (Zharov *et al.*

2006). When the nanoparticles reach their target cells and this is followed by irradiation with NIR light, the overheating effects could destroy the target cells rapidly. In addition, some research groups investigated the combination of different methods to achieve more efficient and more specific antibacterial activities in gold nanostructures, like the incorporation of antibiotics for instance. Huang and coworkers studied the use of gold nanoparticles with polygonal shapes functionalized with the antibiotic vancomycin (Au@van nanoparticles) as photothermal agents, when combined with NIR light irradiation (808 nm, 0.2 W cm⁻²), Au@van nanoparticles could effectively inhibit pathogenic bacteria cell growth within 5 minutes, including Gram-positive, Gram-negative, and antibiotic-resistant bacteria (Huang *et al.* 2007). Moreover, Chen *et al.* tested the synergistic effect of photothermal treatment and antibiotic killing of *S. aureus* (Meeker *et al.* 2016). They fabricated gold nanoconstructs coated with polydopamine (PDA) for loading antibiotic daptomycin (Dap) (Figure 6). These Dap-loaded nanostructures were targeted to the bacteria by conjugating antibodies against staphylococcal protein A. The targeted nanodrug was activated by NIR light to convert the photo-energy to thermal energy; the resulting temperature change caused the simultaneous generation of localized photothermal effects and PDA expansion, leading to controlled antibiotic release. It was shown that it is possible to enhance the antibacterial activity of gold nanoparticles by combining them with many other materials. Therefore, this method has the potential for use as a therapeutic method for biofilm-associated infections caused by drug-resistant bacteria.
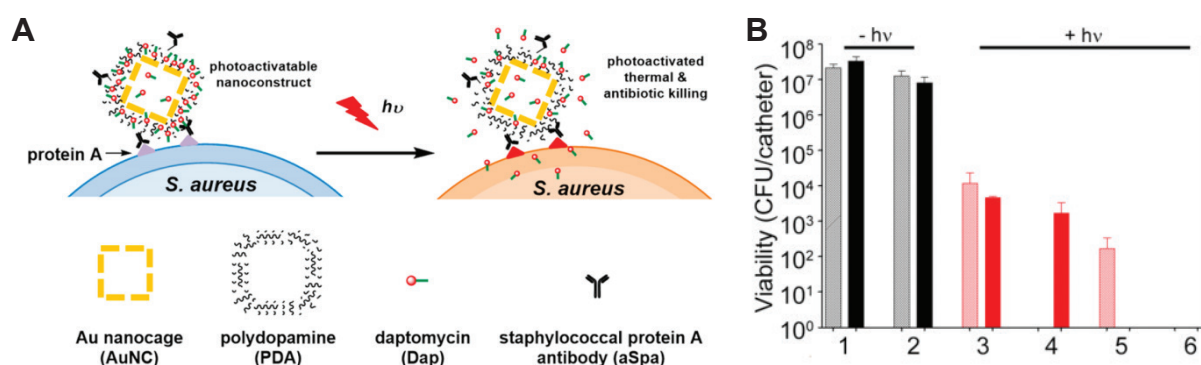

Figure 6. A) Schematic illustration of the working mechanism in the targeted photoactivatable nanoconstruct for the synergistic photothermal and antibiotic treatment of *S. aureus*. **B)** Bacterial cell killing using a biofilm model. Experimental groups are (1) no treatment, (2) 5 µg mL⁻¹ daptomycin (Dap), and irradiation plus (3) polydopamine-coated gold nanocages (AuNC@PDA), (4) AuNC@PDA conjugated to staphylococcal protein A; Spa (aSpa), (5) AuNC@PDA loaded with Dap (AuNC@Dap/PDA), and (6) AuNC@DapHi/PDA conjugated to aSpa (AuNC@Dap/PDA−aSpa). Killing was assessed at 0 h (striped bars) and 24 h (solid bars) after treatment. Black bars indicate non-irradiated groups, and red bars indicate irradiated groups. This figure has been adapted from reference (Meeker *et al.* 2016) which was published under an ACS AuthorChoice License.

Another interesting example of the application of PTT in bacterial infection treatment is a hybrid system of Au NPs in conjunction with polydopamine-assisted hydroxyapatite prepared by Xu *et al.* (Xu *et al.* 2018). This study presented *in situ* promotion of wound healing by a low-temperature PTT assisted nanocatalytic antibacterial system utilizing a polydopamine (PDA) coating on hydroxyapatite (HAp) incorporated with gold nanoparticles (Au-HAp). The PDA@Au-HAp NPs produce hydroxyl radicals (•OH) from H_2O_2 at low concentrations, thus enhancing photothermal antibacterial performance at 45°C and avoiding unnecessary damage on normal tissues. In addition, this approach stimulated tissue repairing-related gene expression to facilitate the formation of granulation tissues and collagen synthesis, accelerating wound healing.

Although noble metal nanomaterials have offered an outstanding photothermal effect for different medical issues, such as cancer treatment and bacterial infections, some problems may need to be solved. For instance, gold-based nanomaterials are non-biodegradable, which leads to further detection of nanoparticles after treatment. Therefore, it is necessary to investigate new kinds of nanomaterials in order to develop photothermal agents with exceptional optical properties, good biocompatibility, and that are biodegradable.

3.3. Carbon-based nanoparticles

The noble metal nanomaterials mentioned before may present some problems that have significantly limited their application in clinical trials, such as their non-biodegradability and possible long-term cytotoxicity. To achieve excellent photothermal nanoagents with improved biocompatibility and lowered cytotoxicity, carbon-based nanoparticles have been

widely studied in recent years in order to reduce lateral effects, mainly due to the intrinsic biocompatibility of carbon. Among the extensive range of carbon nanomaterials, we will focus on graphite-related structures such as single and multi-wall carbon nanotubes (SWCNT and MWCNT, respectively), and graphene derivatives, including graphene oxide (GO) and reduced graphene oxide (rGO). Some applications of nanodiamonds in PTT will also be mentioned.

In the last decades, carbon nanotubes (CNTs) have been the most developed carbon-based nanostructures. These nanostructures, discovered by Iijima (Iijima 1991), are allotropic forms of carbon obtained by rolling up graphene sheets into a tube shape, forming a cylinder (Figure 7a) with characteristic diameters ranging from 0.4 to 50 nm. Length, on the other hand, varies greatly with synthesis conditions and can reach values as high as several centimeters (Wang *et al.* 2009). As a result, CNTs have extremely high aspect ratios. Depending on the number of sheets rolled into concentric cylinders, they can be divided into two broad categories: single-wall carbon nanotubes (SWCNT) and multi-wall carbon nanotubes (MWCNT) (Figure 7b). MWCNTs usually have larger diameters (> 100 nm) than SWCNT, which can be as small as 1 nm.
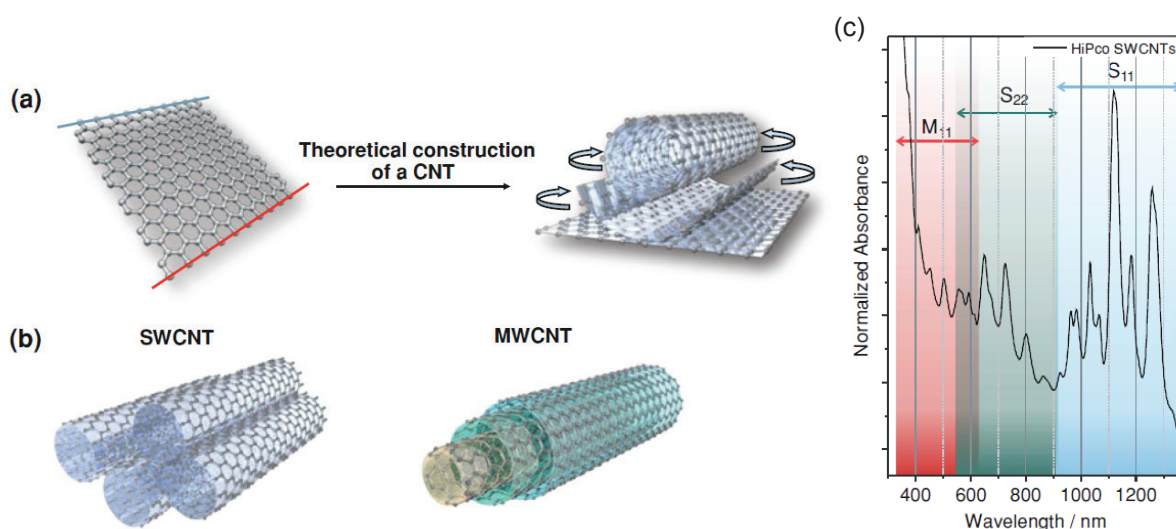

Figure 7. a) Schematic representation of the theoretical construction of a carbon nanotube by rolling up a graphene sheet. **b)** Representation of a single-walled carbon nanotube (SWCNT–left) and a multi-walled carbon nanotube (MWCNT–right). **c)** Typical UV/Vis/ HiPco SWCNTs nIR absorption spectrum of HiPco SWCNT dispersed in an aqueous solution of SDBS (1 wt%) after ultracentrifugation. Metallic M_{11} transitions are indicated by the red shaded background, and semiconducting S_{22} and S_{11} transitions by the green and blue colored shaded background, respectively. Figures have been adapted from reference (Backes *et al.* 2010) with permission from John Wiley and Sons and Copyright Clearance Center.

CNTs exhibit strong absorbance in the NIR, which makes them a promising tool in PTT (Figure 7c). Typically, this kind of nanomaterials are functionalized with PEG coatings, since this helps improve biocompatibility, prolongs blood circulation time, and avoids aggregation. As a typical example, Kam *et al.* have demonstrated that, when irradiated by NIR light, CNTs that were internalized in cells can trigger endosomal rupture and cell death without harming normal cells (Kam *et al.* 2005). This discovery led to the development of SWCNT functionalization whit specific ligands for recognizing and targeting tumoral cells. They exploited folate receptors (FR) that are common tumor markers by making highly water-soluble specific SWCNTs non-covalently functionalized by phospholipid-PEG-folic acid (PL-PEG-FA). After incubating both, normal cells and FR-positive HeLa cells (FR$^+$ cells), and irradiating them with an 808 nm laser (1.4 W cm^{-2}) for 2 min, general cell death was confirmed for the FR$^+$ cells by cell morphology changes, whereas normal cells remained intact. This selective destruction of FR$^+$ cells implied that PL-PEG-FA-SWCNT were successfully internalized inside cancerous cells. In addition to this, Zhang and coworkers reported a self-amplified drug delivery system for tumor PTT using MWCNT, with favorable photothermal effect as the vector, polyethylene glycol (PEG) as the shelter, CREKA peptide as the targeting moiety and NIR illumination as the external power (Zhang *et al.* 2016). This self-amplified targeting system (MWCNT-PEG) showed strong tumor targeting ability and powerful photothermal therapeutic effectiveness. Moreover, Sobhani *et al.* were able to improve the dispersability of MWCNTs in water by oxidizing them (O-CNT) and using polyethylene glycol (PEG) for wrapping the surface of nanotubes (Sobhani *et al.* 2017). They found through different cytotoxicity studies that O-CNT was less cytotoxic than pristine MWCNT, and O-CNT-PEG had the lowest toxicity against HeLa and HepG2 cell lines. The effect of O-CNT-PEG in the reduction of melanoma tumor size after PTT was evaluated by exposing cancerous mice to a continuous-wave NIR laser diode (λ=808 nm, P = 2 W and I=8 W cm^{-2}) for 10

minutes. It was found that tumor average size in the mice receiving O-CNT-PEG decreased sharply in comparison with those that only received laser therapy. Furthermore, using carbon nanotubes as photothermal agents for bacteria killing, Yang *et al.* designed nonchemotherapeutic and robust dual-responsive nanoagents to control the trapping, ablation, and releasing activities of pathogenic bacteria via an NIR and magnetic stimulus-responsive regulatory nanosystem (Yang *et al.* 2018). In this system, the temperature-sensitive polymer brush PNIPAm is chemically grown onto the surface of carbon nanotube–Fe_3O_4, whereby the synthesized nanoagents (Fe_3O_4-CNT-PNIPAM) could transition from hydrophilic dispersion to hydrophobic aggregation upon NIR irradiation, which thus controls bacterial trapping, killing, and detaching (Figure 8).
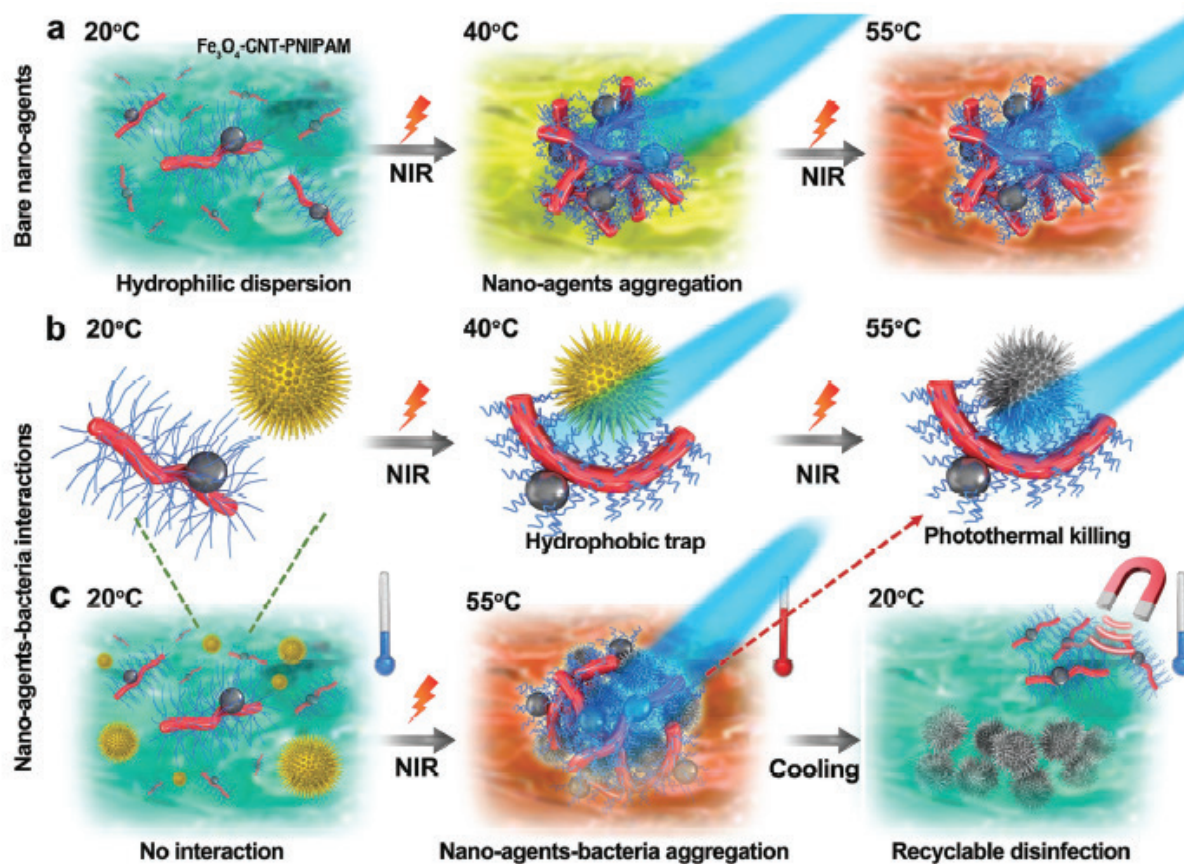

Figure 8. a) The synthesized Fe_3O_4-CNT-PNIPAM nanoagents are hydrophilic and well dispersed at 20°C; upon NIR irradiation, temperature increases; once temperature is above 40°C, the nanoagents turn completely hydrophobic and form robust aggregations. **b)** The detailed interactions between nanoagents with bacteria at different temperatures, the bacteria is trapped by the nanoagents at 40°C, and is killed by the nanoagents at 55°C. **c)** The formation of nanoagent–bacteria aggregations and NIR killing of bacteria at 55°C, the inactivated bacteria can be released from the trap after cooling to low temperature, and the nanoagents can be magnetically collected and reused for antibacterial tests. The figure has been adapted from reference {Yang, 2018 #66} with permission from John Wiley and Sons and Copyright Clearance Center.

Due to their unique intrinsic physical and chemical properties, which include large surface areas, the ability to penetrate biological membranes, a relatively low toxicity, and special electrical, thermal and spectroscopic properties, CNTs constitute a promising nanomaterial for medical applications. Therefore, CNTs combined with different molecules, including the incorporation of antibiotics, antibodies, metals, and magnetic nanoparticles or tumor markers as well as the functionalization with many polymeric materials, enhance their activity as effective photothermal nanoagents in cancer therapy (Thakare *et al.* 2010) and bacterial infectious diseases treatment (Xu *et al.* 2019).

Like CNTs, graphene-based nanomaterials also have strong optical absorption in the NIR region. Compared to metallic nanoparticles and CNTs, graphene materials (especially GO) possess improved properties such as greater optical absorption in the NIR region and higher photothermal conversion, high specific area, and lower cost. Loh and coworkers (Loh *et al.* 2010) have also found that visible and NIR fluorescence of GO can be tuned depending on the intended application, although it was impossible to fully understand the mechanism. Graphene derivatives such as pristine (non-oxi-

dized) graphene sheets, GO and rGO have been widely studied for various biomedical applications, such as drug delivery system, cell imaging, and PTT. For instance, Yang *et al.* were the first group in investigating the application of graphene in PTT (Yang *et al.* 2010). They found that nanographene sheets (NGS) functionalized with PEG (NGS-PEG) exhibited strong NIR absorbance and *in vivo* efficient tumor destruction under NIR laser irradiation. Additionally, the studied nanomaterial presented relatively low retention in reticuloendothelial systems. Furthermore, Dai and colleagues (Robinson *et al.* 2011) developed nanosized, reduced graphene oxide (nano-rGO) sheets with high NIR light absorbance and biocompatibility functionalized with PEG and carrying a targeting peptide covalently bonded. This nanomaterial demonstrated to be an efficient photothermal agent, since it caused a highly effective *in vitro* photoablation of cells.

In addition, combining photothermal and chemotherapy to generate a synergistic treatment is a more effective way to destroy cancer cells than monotherapy. Chen *et al.* studied the combination of rGO with gold nanoparticles and produced a hybrid reduced rGO-loaded ultrasmall gold nanorod vesicle (rGO-AuNRVe) with remarkably amplified PA performance and photothermal effects (Song *et al.* 2015). The hybrid is an excellent drug carrier due to its high loading capacity of doxorubicin (DOX), as both the cavity of the vesicle and the large surface area of the encapsulated rGO can be used for loading DOX. The loaded drug is released sequentially – NIR photothermal heating induces DOX release from the vesicular cavity (Figure 9i), and an intracellular acidic environment induces DOX release from the rGO surface (Figure 9ii).
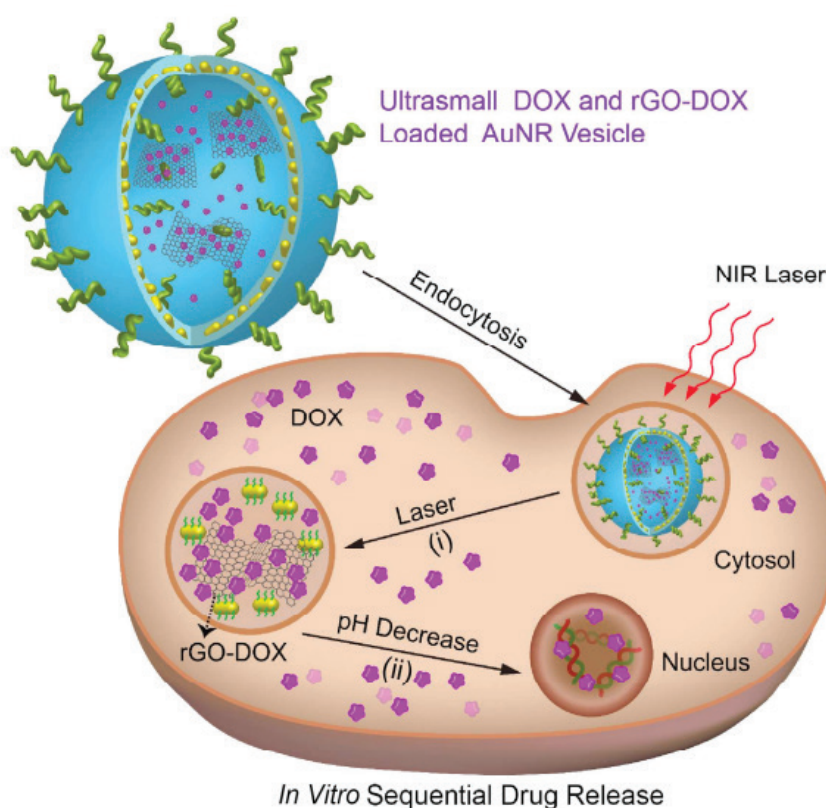

Figure 9. Schematic illustration of sequential DOX release triggered by **(i)** remote NIR laser irradiated photothermal effect and **(ii)** acidic environment of the cancerous cell. Adapted from reference (Song *et al.* 2015) with permission from the American Chemical Society.

Furthermore, graphene nanomaterials are also being studied in combination with different nanomaterials in PTT applied to the treatment of infectious diseases caused by drug-resistant bacteria (Xu *et al.* 2019). Recently, Pereyra *et al.* (Pereyra *et al.* 2018) demonstrated that GO dispersion at low concentrations (c.a. 2 µg mL^{-1}) under NIR irradiation for 15 min decreased bacterial viability by ~98%. *P. aeruginosa* treated with GO and irradiated exhibited DNA fragmentation due to the physical damage of cell membranes. This characteristic represents an advantage in comparison with traditional antibacterial nanomaterials (Ag NPs, for instance), which induce cell killing due to the toxicity of the nanoparticles *per se*. Feng and colleagues investigated 2D rGO supported Au nanostar nanocomposite (rGO/AuNS) for synergistically killing multidrug-resistant bacteria (Feng *et al.* 2019). Owing to their prickly and sharp-edge nanostructure, rGO/AuNS displayed superior antibacterial activity probably due to the damaging of the cell walls or membranes. It was found that the bactericidal efficiency was significantly enhanced when irradiated with 808 nm NIR laser, mainly due to the localized

hyperthermal effect of rGO/AuNS. (Figure 10) Thus, the production of AuNS and rGO nanocomposites is an alternative potential photothermal agent for the synergistic killing of bacteria.
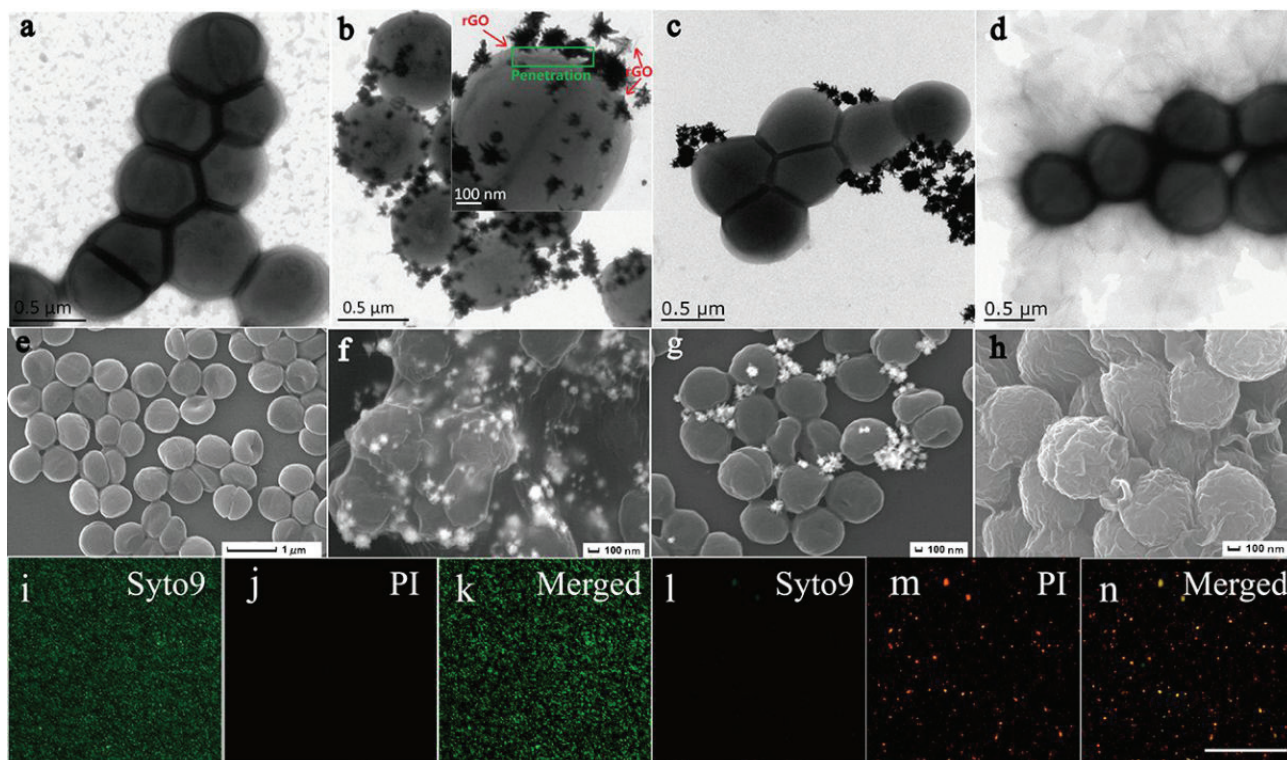

Figure 10. TEM images of MRSA (**a**), MRSA incubated with rGO/AuNS0.02 (**b**) and AuNS (**c**) after 808 nm NIR irradiation for 6 min, and MRSA incubated with rGO (**d**); SEM images of MRSA (**e**), MRSA incubated with rGO/AuNS0.02 (**f**) and AuNS (**g**) after 808 nm NIR irradiation for 6 min, and MRSA incubated with rGO (**h**). Laser power density was 3 W cm^{-2}. Fluorescence microscopy images of MRSA (**i**), (**j**) and (**k**) and MRSA exposed to NIR laser irradiation for 6 min after incubating with 0.26 mM rGO/AuNS0.02 (**l**), (**m**) and (**n**), which were treated with LIVE/DEAD BacLight Bacterial Viability Kit. The scale bar in the figure is 100 μm. The figure has been adapted with permission from Reduced Graphene Oxide Functionalized with Gold Nanostar Nanocomposites for Synergistically Killing Bacteria through Intrinsic Antimicrobial Activity and Photothermal Ablation. *ACS Applied Bio Materials*. 2(2):747-756. Copyright 2019 American Chemical Society.

The works mentioned here provided an innovative treatment for combating bacterial nosocomial infections without the use of antibiotics, opening a new area of clinical application via simple PTT.

Finally, nanodiamonds (NDs) with a bulk diamond-like structure have emerged as promising carbon nanomaterials in biomedical applications mainly due to their high surface area, optical properties, high biocompatibility, nontoxicity, colloidal stability, excellent mechanical strength, and high surface functionality. Generally, NDs have been used as luminescent biomarkers capable of intracellular high-resolution tracking, and recently have been proposed as excellent nanothermometers that can be used for thermal imaging of single cells (Kucsko *et al.* 2013). However, these nanomaterials have not shown high light-to-heat conversion efficiencies; thus, they are not suitable for photothermal applications. Ahn *et al.* deposited polyaniline on diamond nanoparticles (PANI-ND) by polymerizing aniline at the surface of NDs for efficient PTT (Ahn *et al.* 2019). They found that the UV absorbance intensity of PANI-ND increased at the lower pH in the NIR region, as expected for PANI layers, resulting in an enhanced photothermal effect at the tumor site. Notably, the viability of HeLa cells treated with PANI-ND decreased by less than 20%, suggesting the high efficiency of PTT using this functionalized nanodiamons. Therefore, it is likely that NDs act as nanotemplates to form core-shell (ND/PANI) nanoparticles.

3.4. Other nanomaterials and composites using dyes for PTT

As mentioned in previous sections, PTT is now combined with other therapies that also involve a light process in order to enhance efficiency. In this sense, the use of organic dyes facilitates and gives new opportunities to achieve successful

treatment. In this section, some examples of recently published works involving dyes incorporation or conjugation with diverse nanomaterials/composites for combined therapies are described.

Wang *et al.* summarized the research focused on the photothermal generation conjugating organic colorant dyes with different nanostructures (e.g. nanoparticles, polymeric micelles, block copolymers, among others) (Wang *et al.* 2016). The most relevant dyes involve cyanine derivates and the well know IR-780, IR-820, and IR-825 dyes. In all cases, irradiation was applied at 808 nm. Different cancer cell types and animal models for *in vitro* and *in vivo* assays, respectively, were employed. Additionally, using indocyanine, multifunctional nanoparticles based on Pt(II)-meso-tetra-(pentafluoro-phenyl)porphyrine (PtTFPP) and poly(9,9-di-noctylfluorenyl-2,7-diyl) (PFO) loaded with indocyanine green (ICG), a novel material was fabricated (Wang *et al.* 2017). The nanomaterial involves an organic polymer (PFO), a photosensitizer porphyrin (PtTFPP), and a NIR absorbing dye (ICG). This particular design enables a strong photothermal absorption under laser light added to the high singlet oxygen generation, being a very interesting agent for applications on tumoral therapies combining PTT with PDT. The authors remark that a synergistic effect is present, improving the therapeutic efficacy of both individual therapies (PTT or PDT). In the same way, heptamethine cyanines (IR-825, IR-780, IR-808, and IR-2) were proposed as dyes for conjugation with polymeric micelles for PTT activity. The use of these organic compounds was excellently summarized by Jung *et al.* (Jung *et al.* 2018) (Figure 11). In addition, they have shown many other possibilities – for example, the application of diverse croconaine, porphyrins, and diketopyrrolopyrrole-based agents for photothermal effect – with successful results towards new platforms that complement PTT with PAI, NIR fluorescence imaging, and MRI, among others.
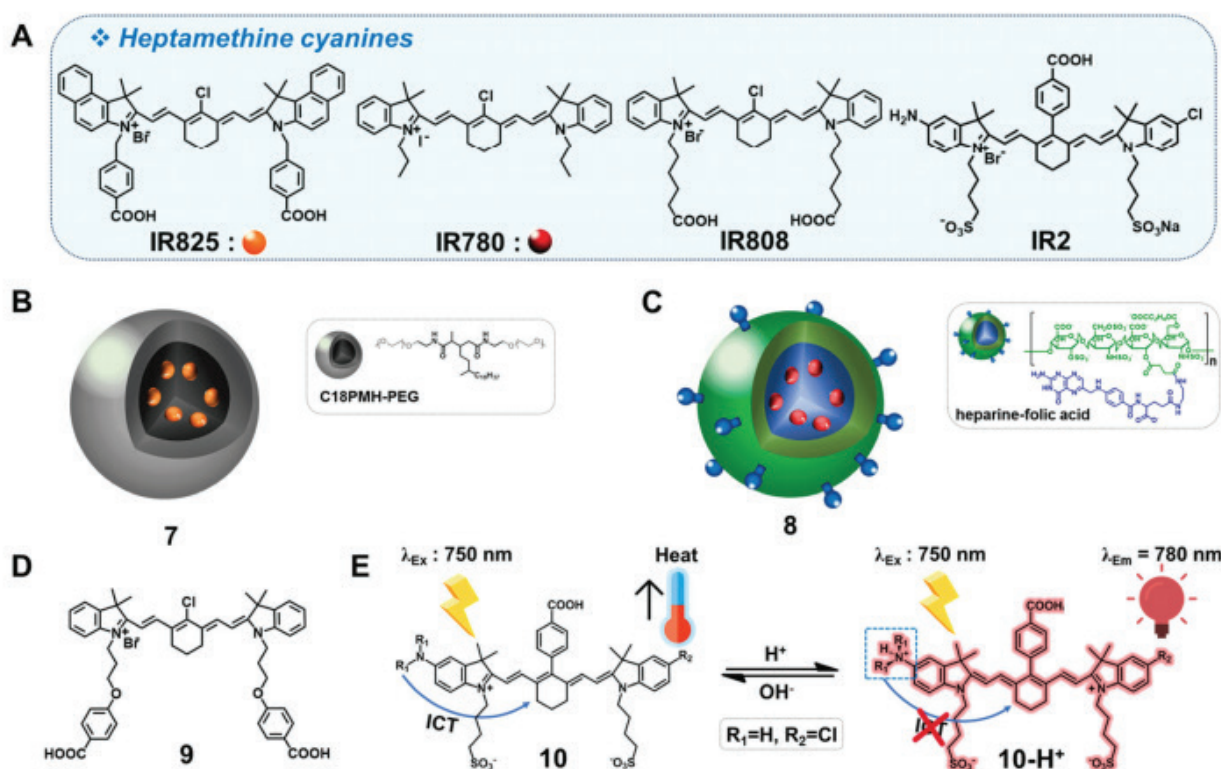

Figure 11. (A) Molecular structures of the heptamethine cyanines: IR825, IR780, IR808, and IR2 and associated PTT systems: (B) IR825/PEGylated micelle 7, (C) IR780/heparine–folic acid system 8, (D) mitochondria-targeted hep-tamethine 9, and (E) pH-switchable theranostic heptamethine dyes 10 and 10-H+. This figure has been reproduced from reference{Jung, 2018 #100} with permission from the Royal Society of Chemistry.

Another material reported for NIR imaging and PTT were heparine-folic acid nanoparticles loaded with IR-780 (HF-IR-780 NPs). The authors affirm that IR-780 exhibits some advantages compared to ICG, such as stability and fluorescence intensity. Dye conjugation was made by ultrasonication process, obtaining monodisperse spherical particles. MCF-7 cells were employed for *in vitro* assays, and it was concluded that nanomaterial does not present cytotoxic effects and is biogradable. The results of these experiments reveal a temperature increase in MCF7 tumor tissues of 20 C, making HF-IR-780 NPs a promising photothermal nanoagent and a potential candidate for theranostics (Yue *et al.* 2013). On the other

side, Calderón and coworkers reported the design of a system that involves a smart thermoresponsive nanogel scaffold that allows obtaining a combination of PDT/PTT. The synthetic approach used the covalent conjugation by amide formation between acrylated polyglycerol amine (dPG-Ac) and the dye (IR-806) for smart nanogel production (tNG-IR-806), exhibiting controlled shape, size, and monodispersity (c.a. 90 nm, PDI: 0.16). By heating on the tNG-IR806 at different concentrations using a NIR irradiation source (wavelength: 785 nm, power density: 0.59 W cm^{-2}), thermal collapse was evidenced by turbidimetric experiments in several cycles. (Figure 12). Upon NIR laser irradiation, a hyperthermia process was observed with the subsequent ablation of ovarian A2728 cancer cells. These nanomaterials have shown very interesting properties for applications on theranostic as well as controlled drug-delivery, taking advantage of NIR light absorption and temperature sensitivity (Asadian Birjand *et al.* 2016).
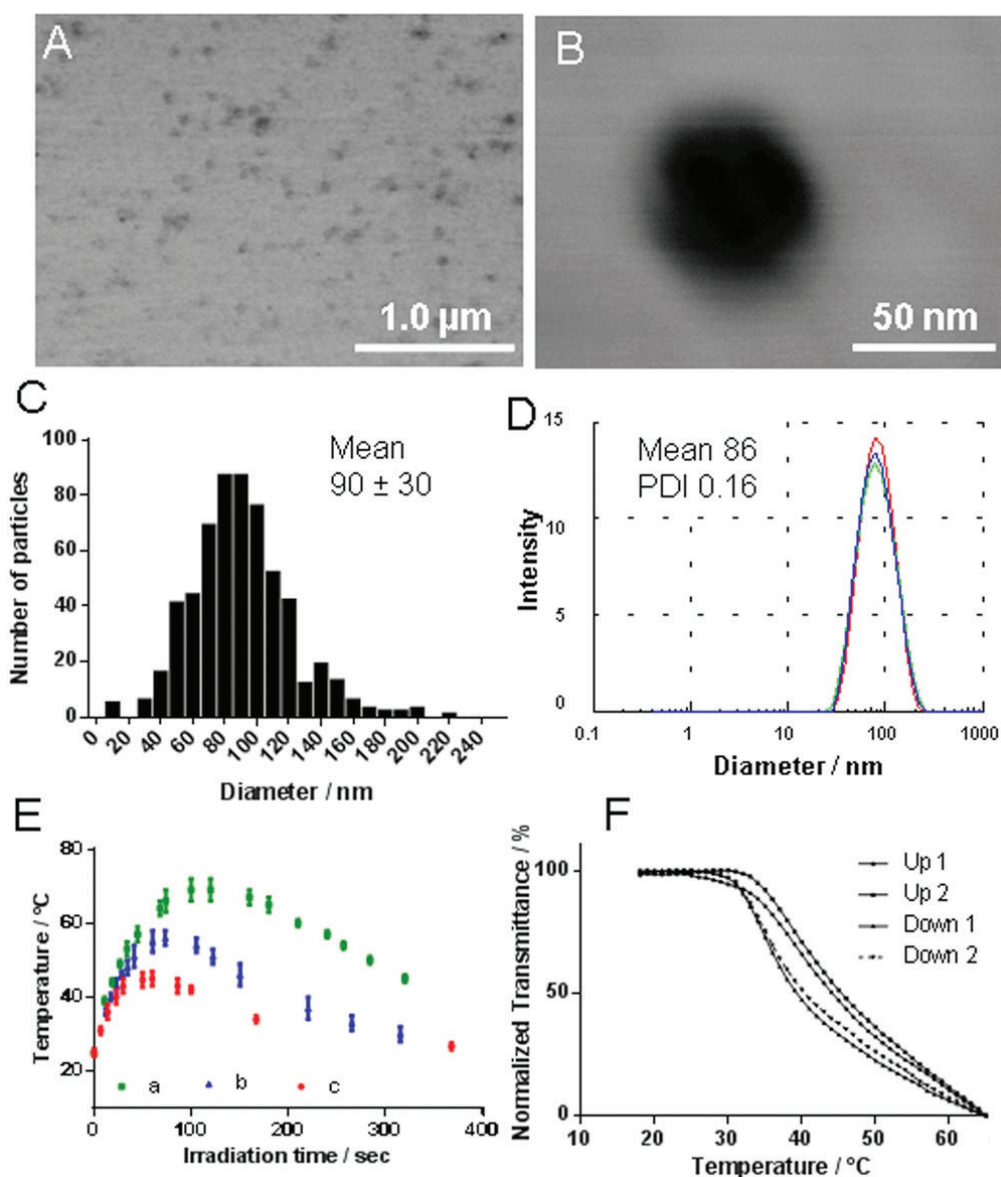

Figure 12. tNG-IR806 characteristics. (A-B) TEM image of uranyl acetate stained tNG-IR806 and zoom. Additional TEM images can be found in Figure S5 in the Supporting Information. (C) Size distribution determined from TEM images by ImageJ software. (D) Hydrodynamic diameter distribution measured by DLS. (E) Heating curves of tNG-IR806 at different aqueous concentrations: a (green) = 12 mg mL -1 , b (blue) = 6 mg mL -1 , c (red) = 3 mg mL -1 upon NIR laser irradiation at a wavelength of 785 nm and power density of 0.59 W cm -2 .Data are expressed as mean ± SD (n = 3). (F) Normalized UV-vis transmittance curves of two heating and cooling cycles in turbidimetry at 450 nm wavelength. This figure has been reproduced from reference (Asadian Birjand *et al.* 2016) with permission from John Wiley and Sons and Copyright Clearance Center.

Diverse functional micelles and lipid-based nanoparticles combined with organic dyes are also employed for PTT. For example, Kuang *et al.* arrive to relevant results referred to as photothermal efficiency by using solid lipid nanoparticles (SLNs) conjugated with c(RGDyK) peptide (cyclo (Arg-Gly-Asp-D-Tyr-Lys)) as a carrier for IR-780 delivery (Kuang *et*

al. 2017). cRGD-IR-780 SLNs were produced by using the solvent-diffusion method. The photothermal performance of the synthesized nanoparticles was studied by exposing different concentrations of the nanomaterial under NIR laser (808 nm) at 1 W cm^{-2}. Whereas the material free of IR-780 in the aqueous solution presented a small increment of temperature, cRGD-IR-780 SLNs showed a clear photothermal effect (an increase of 32°C, at 50 mg L^{-1}). In addition, U87MG cell viability was not affected (no cytotoxicity) and the same cells were killed (viability decrease to 15.1%) by application of NIR light. *In vivo* results using mice reveals a similar photothermal performance as that of *in vitro* assays, showing a total U87MG tumor regression. These studies were complemented with direct observation of cRGD-IR-780 SLNs, making the material a potential candidate for NIR imaging-guided targeted cancer treatment. By loading the same dye (IR-780) into polymeric micelles, a multi-drug delivery system was proposed for the treatment of colorectal cancer by applying PTT. A series of complete chemical characterization of micelles and testing with HCT-116 and SW-620 cell lines, together with animal models, allows confirming that the novel nanomaterial could be used efficiently for PTT (Shih et al. 2017).

Poly(12-(methacryloyloxy)dodecylphosphorylcholine) (PCB-lipid) micellar nanoparticles encapsulating IR-780 dye were recently reported by Rajendrakumar *et al.* (Rajendrakumar *et al.* 2018). The synthesis consists on the addition–fragmentation chain transfer (RAFT) polymerization and self-assembly procedure. The material was developed for the treatment of cervical tumor using PTT combined with NIR-based fluorescence imaging. The photothermal effect of the nanoparticles has shown a high-temperature change (~30°C) under NIR light (808 nm, 2 W cm^{-2}) for only 5 minutes of irradiation. Besides, good viability of PCB-lipid–IR-780 nanoparticles was observed in cytotoxic studies employing TC-1 cells. A concentration-dependent effect was found in the cell viability reduction when the nanomaterial was exposed upon NIR laser irradiation. *In vivo* studies in animal tumor models revealed a significant reduction of the tumor volume by PTT mechanisms, demonstrating excellent heat conversion.

Other nanocomposites based on less common materials employing NIR dyes were developed recently. Ferritin nanocages were proposed as a theranostic platform based on new cyanine green (IR-820). The resulting material (spherical particles of c.a. 20 nm) have shown NIR absorption, which is of interest for PAI/fluorescence multimodal imaging-guided PTT. In this case, *in vitro* photothermal assays were carried out on 4T1 cells, showing a high photothermal conversion efficiency after 5 minutes of NIR irradiation (808 nm) at low powers (0.1, 0.5, and 1 W cm^{-2}). Taking into account the presence of NIR fluorescence and PAI effects, the *in vivo* multimodal imaging-guided PTT was evaluated on mice with subcutaneous 4T1 tumors injected. The changes on tumor temperatures were registered at different laser powers, resulting in 23.8°C (0.5 W cm^{-2}) and 42.2°C (1 W cm^{-2}) with 100% of tumor elimination (Huang *et al.* 2014). Another example shows how it is possible to employ black phosphorus nanosheets (BPs) to build a novel photothermal agent. The material is similar to graphene nanosheets, but it is constituted by phosphorous 2D layers. The aromatic amine group of Nile Blue dye is diazotized, and the aromatic cation reacted with BPs, obtaining an attached dye NB@BPs. The nanosheets show good optical performance, stability, and high NIR fluorescence. Additionally, the nanomaterials show good biocompatibility and no cytotoxicity. Taking advantage of these properties, the PTT effect was evaluated. The exposition of MCF7 cancer cells to NB@BPs at low concentration (50 ppm) and illumination with NIR light (10 minutes) caused a 90% decrease in cell viability. Furthermore, the *in vivo* experiments combining fluorescence imaging and PTT revealed successful tumor ablation by the effect of temperature increasing (~23°C), demonstrating the potential ability of NB@BPs to be applied on nanomedicine (Zhao *et al.* 2017).

Conclusions and future perspectives

In summary, we have presented a review of the different nanoparticles that are currently being studied in PTT. The main objective of these photothermal agents is to be highly efficient and selective for thermal therapies for diverse diseases, mainly cancer and bacterial infections. It has been shown that many nanoparticles (metallic nanoparticles, conductive polymeric nanoparticles, carbon nanotubes, graphene-based nanoparticles, etc.) can be used as photothermal agents, since they present large light-to-heat conversion efficiencies. Among them, carbon-based and conjugated polymers show good PTT properties as well as good biodegradability.

However, there are still some issues to be solved before translating this platform to the clinic. For example, in order to get the deepest tissue penetration, it is necessary to find the best wavelengths within the biological windows. Some nanomaterials (e.g. PANI) show a clear pH effect which decreases NIR absorption in the cytoplasm (neutral pH). However, such property could be altered by chemical functionalization, such as self-doping. Moreover, the combination of conjugated polymers with NIR dyes could also increase photothermal efficiency.

On the other hand, in the case of metallic nanoparticles, additional effects such as localized plasmon have been shown to affect catalysis or even liquid boiling. It is likely that such phenomena have effects on cell or bacteria induced death, but it has not been investigated closely.

As it can be seen in the work reviewed here, the heat production due to NIR light absorption is measured at the macroscopic level as an increase in the temperature of the irradiated zone. However, it is likely that nanomaterial temperature could reach values higher than the mean value of the irradiated zone. Besides, such large temperature changes could be responsible for cell death.

However, there is a lack of real-time and/or local temperature monitoring systems. The best candidate, temperature-dependent fluorescence, does not work, up to now, in the NIR range. On the other hand, thermosensitive polymers have been used to detect local temperature gradients at the nanometric level, but signal detection is somewhat slow.

Hereafter, the development of multifunctional nanoplatforms, which include heating, tracking, and sensing all in one, is expected. This could involve a combination of more than one kind of nanomaterials. The very nature of nanoagents allows combining different materials without undue interactions such as the ones that occur in molecules. We think this will be the main research focus in the field during the next years.

Acknowledgments

References

[1] G. Y. Ahn. Polyaniline-grafted nanodiamonds for efficient photothermal tumor therapy. *Colloids and Surfaces B: Biointerfaces*. 180: 273-280, 2019.

[2] D. I. Andersson and D. Hughes. Antibiotic resistance and its cost: is it possible to reverse resistance? *Nature Reviews Microbiology*. 8: 260, 2010.

[3] M. Asadian Birjand. Near infrared dye conjugated nanogels for combined photodynamic and photothermal therapies. *Macromolecular bioscience*. 16(10): 1432-1441, 2016.

[4] C. Backes and A. Hirsch. Noncovalent Functionalization of Carbon Nanotubes. In *Chemistry of Nanocarbons*. John Wiley & Sons Ltd, United Kingdom, 2010.

[5] E. Birben. Oxidative stress and antioxidant defense. *The World Allergy Organization journal*. 5(1): 9-19, 2012.

[6] E. Boisselier and D. Astruc. Gold nanoparticles in nanomedicine: preparations, imaging, diagnostics, therapies and toxicity. *Chemical Society Reviews*. 38(6): 1759-1782, 2009.

[7] S. Bongiovanni Abel. Photothermal lysis of Pseudomonas aeruginosa by polyaniline nanoparticles under near infrared irradiation. *Biomedical Physics & Engineering Express*. 4(4): 045037, 2018.

[8] S. Bongiovanni Abel. Smart polyaniline nanoparticles with thermal and photothermal sensitivity. *Nanotechnology*. 25(49): 495602, 2014.

[9] S. Bongiovanni Abel. Synthesis of polyaniline (PANI) and functionalized polyaniline (F-PANI) nanoparticles with controlled size by solvent displacement method. Application in fluorescence detection and bacteria killing by photothermal effect. *Nanotechnology*. 29(12): 125604, 2018.

[10] T. Cantu. Conductive polymer-based nanoparticles for laser-mediated photothermal ablation of cancer: synthesis, characterization, and in vitro evaluation. *International journal of nanomedicine*. 12: 615-632, 2017.

[11] Y. Cao. Near-infrared conjugated polymers for photoacoustic imaging-guided photothermal/chemo combination therapy. *Journal of Materials Chemistry B*. 5(27): 5479-5487, 2017.

[12] J. Chen. Nanomaterials as photothermal therapeutic agents. *Progress in materials science*. 2018.

[13] L. Cheng. Functional Nanomaterials for Phototherapies of Cancer. *Chemical Reviews*. 114(21): 10869-10939, 2014.

[14] L. Cheng. Organic Stealth Nanoparticles for Highly Effective in Vivo Near-Infrared Photothermal Therapy of Cancer.

ACS Nano. 6(6): 5605-5613, 2012.

[15] P. Fan. GO@Polyaniline Nanorod Array Hierarchical Structure: A Photothermal Agent with High Photothermal Conversion Efficiency for Fast Near-Infrared Responsive Hydrogels. *Industrial & Engineering Chemistry Research*. 58(9): 3893-3901, 2019.

[16] Y. Feng. Reduced Graphene Oxide Functionalized with Gold Nanostar Nanocomposites for Synergistically Killing Bacteria through Intrinsic Antimicrobial Activity and Photothermal Ablation. *ACS Applied Bio Materials*. 2(2): 747-756, 2019.

[17] D. He. Combined photothermal and antibiotic therapy for bacterial infection via acidity-sensitive nanocarriers with enhanced antimicrobial performance. 12: 415-429, 2018.

[18] L. R. Hirsch. Nanoshell-mediated near-infrared thermal therapy of tumors under magnetic resonance guidance. *Proceedings of the National Academy of Sciences*. 100(23): 13549, 2003.

[19] G. Housman. Drug resistance in cancer: an overview. *Cancers (Basel)*. 6(3): 1769-1792, 2014.

[20] P. Huang. Dye-loaded ferritin nanocages for multimodal imaging and photothermal therapy. *Advanced materials (Deerfield Beach, Fla.)*. 26(37): 6401-6408, 2014.

[21] W.-C. Huang. Functional gold nanoparticles as photothermal agents for selective-killing of pathogenic bacteria. *Nanomedicine*. 2(6): 777-787, 2007.

[22] X. Huang. Cancer Cell Imaging and Photothermal Therapy in the Near-Infrared Region by Using Gold Nanorods. *Journal of the American Chemical Society*. 128(6): 2115-2120, 2006.

[23] L. Ibarra. Near-infrared mediated tumor destruction by photothermal effect of PANI-Np in vivo. *Laser Physics*. 23(6): 066004, 2013.

[24] S. Iijima. Helical microtubules of graphitic carbon. *Nature*. 354(6348): 56-58, 1991.

[25] P. K. Jain. Au nanoparticles target cancer. *Nano Today*. 2(1): 18-29, 2007.

[26] P. K. Jain. Calculated Absorption and Scattering Properties of Gold Nanoparticles of Different Size, Shape, and Composition: Applications in Biological Imaging and Biomedicine. *The Journal of Physical Chemistry B*. 110(14): 7238-7248, 2006.

[27] D. Jaque. Nanoparticles for photothermal therapies. *Nanoscale*. 6(16): 9494-9530, 2014.

[28] X. Jia. Versatile graphene-based photothermal nanocomposites for effectively capturing and killing bacteria, and for destroying bacterial biofilms. *Journal of Materials Chemistry B*. 5(13): 2459-2467, 2017.

[29] H. S. Jung. Organic molecule-based photothermal agents: an expanding photothermal therapy universe. *Chemical Society Reviews*. 47(7): 2280-2297, 2018.

[30] N. W. S. Kam. Carbon nanotubes as multifunctional biological transporters and near-infrared agents for selective cancer cell destruction. *Proceedings of the National Academy of Sciences of the United States of America*. 102(33): 11600-11605, 2005.

[31] Y. Ko. Antibacterial poly (3,4-ethylenedioxythiophene):poly(styrene-sulfonate)/agarose nanocomposite hydrogels with thermo-processability and self-healing. *Carbohydrate Polymers*. 203:26-34, 2019.

[32] C. Korupalli. Acidity-triggered charge-convertible nanoparticles that can cause bacterium-specific aggregation in situ to enhance photothermal ablation of focal infection. *Biomaterials*. 116:1-9, 2017.

[33] Y. Kuang. Hydrophobic IR-780 dye encapsulated in cRGD-conjugated solid lipid nanoparticles for NIR imaging-guided photothermal therapy. *ACS Applied Materials & Interfaces*. 9(14): 12217-12226, 2017.

[34] G. Kucsko. Nanometre-scale thermometry in a living cell. *Nature*. 500:54, 2013.

[35] S. Link and M. A. El-Sayed. Simulation of the Optical Absorption Spectra of Gold Nanorods as a Function of Their Aspect Ratio and the Effect of the Medium Dielectric Constant. *The Journal of Physical Chemistry B*. 109(20): 10531-10532, 2005.

[36] S. Link and M. A. El-Sayed. Size and Temperature Dependence of the Plasmon Absorption of Colloidal Gold Nanoparticles. *The Journal of Physical Chemistry B*. 103(21): 4212-4217, 1999.

[37] X. Liu. Functionalized poly(pyrrole-3-carboxylic acid) nanoneedles for dual-imaging guided PDT/PTT combination therapy. *Biomaterials*. 167: 177-190, 2018.

[38] K. P. Loh. Graphene oxide as a chemically tunable platform for optical applications. *Nature Chemistry*. 2: 1015, 2010.

[39] A. Lombardi. Surface Plasmon Resonance Properties of Single Elongated Nano-objects: Gold Nanobipyramids and Nanorods. *Langmuir*. 28(24): 9027-9033, 2012.

[40] C. Loo. Nanoshell-Enabled Photonics-Based Imaging and Therapy of Cancer. 3(1): 33-40, 2004.

[41] P. A. Mackowiak. Direct Effects of Hyperthermia on Pathogenic Microorganisms: Teleologic Implications with Regard to Fever. *Clinical Infectious Diseases*. 3(3): 508-520, 1981.

[42] D. G. Meeker. Synergistic Photothermal and Antibiotic Killing of Biofilm-Associated Staphylococcus aureus Using Targeted Antibiotic-Loaded Gold Nanoconstructs. *ACS Infectious Diseases*. 2(4): 241-250, 2016.

[43] J. U. Menon. Nanomaterials for photo-based diagnostic and therapeutic applications. *Theranostics*. 3(3): 152, 2013.

[44] N. J. Millenbaugh. Photothermal killing of Staphylococcus aureus using antibody-targeted gold nanoparticles. *International journal of nanomedicine*. 10: 1953-1960, 2015.

[45] M. Molina. Polymeric near-infrared absorbing dendritic nanogels for efficient in vivo photothermal cancer therapy. *Nanoscale*. 8(11): 5852-5856, 2016.

[46] B. Nikoobakht and M. A. El-Sayed. Preparation and Growth Mechanism of Gold Nanorods (NRs) Using Seed-Mediated Growth Method. *Chemistry of Materials*. 15(10): 1957-1962, 2003.

[47] W. H. Organization. *ANTIMICROBIAL RESISTANCE. Global Report on surveillance 2014*. 2014.

[48] J. Y. Pereyra. Photothermally enhanced bactericidal activity by the combined effect of NIR laser and unmodified graphene oxide against Pseudomonas aeruginosa. *Photodiagnosis and Photodynamic Therapy*. 24: 36-43, 2018.

[49] F. Pierini. Polymer-based nanomaterials for photothermal therapy: FROM light-responsive to multifunctional nanoplatforms for synergistically combined technologies. *Biomacromolecules*. 19(11): 4147-4167, 2018.

[50] S. Rajendrakumar. A lipophilic ir-780 dye-encapsulated zwitterionic polymer-lipid micellar nanoparticle for enhanced photothermal therapy and nir-based fluorescence imaging in a cervical tumor mouse model. *International journal of molecular sciences*. 19(4): 1189, 2018.

[51] J. T. Robinson. Ultrasmall Reduced Graphene Oxide with High Near-Infrared Absorbance for Photothermal Therapy. *Journal of the American Chemical Society*. 133(17): 6825-6831, 2011.

[52] M. Shahnawaz Khan. Near infrared (NIR) laser mediated surface activation of graphene oxide nanoflakes for efficient antibacterial, antifungal and wound healing treatment. *Colloids and Surfaces B: Biointerfaces*. 127: 281-291, 2015.

[53] Y.-H. Shih. EGFR-targeted micelles containing near-infrared dye for enhanced photothermal therapy in colorectal cancer. *Journal of Controlled Release*. 258: 196-207, 2017.

[54] S. Singh. Understanding the Mechanism of Bacterial Biofilms Resistance to Antimicrobial Agents. *The open microbiology journal*. 11: 53-62, 2017.

[55] Z. Sobhani. Photothermal therapy of melanoma tumor using multiwalled carbon nanotubes. *International journal of nanomedicine*. 12: 4509-4517, 2017.

[56] J. Song. Sequential Drug Release and Enhanced Photothermal and Photoacoustic Effect of Hybrid Reduced Graphene Oxide-Loaded Ultrasmall Gold Nanorod Vesicles for Cancer Therapy. *ACS Nano*. 9(9): 9199-9209, 2015.

[57] J. Stejskal and I. Sapurina. Polyaniline: Thin films and colloidal dispersions (IUPAC Technical Report). *Pure and Applied Chemistry*. 77(5): 815-826, 2005.

[58] T. Sun. Second Near-Infrared Conjugated Polymer Nanoparticles for Photoacoustic Imaging and Photothermal Therapy. *ACS Applied Materials & Interfaces*. 10(9): 7919-7926, 2018.

[59] L. Tan. Rapid Biofilm Eradication on Bone Implants Using Red Phosphorus and Near-Infrared Light. *Advanced Materials*. 30(31): 1801808, 2018.

[60] V. S. Thakare. Carbon nanotubes in cancer theragnosis. *Nanomedicine*. 5(8): 1277-1301, 2010.

[61] S. Thota and D. C. Crans. *Metal nanoparticles: synthesis and applications in pharmaceutical sciences.* John Wiley & Sons, Wenheim, Germany, 2018.

[62] L. Tong. Gold nanorods as contrast agents for biological imaging: optical properties, surface conjugation and photothermal effects. *Photochemistry and photobiology*. 85(1): 21-32, 2009.

[63] T. Tsuchido. Destruction of the outer membrane permeability barrier of Escherichia coli by heat treatment. *Applied and environmental microbiology*. 50(2): 298-303, 1985.

[64] J. Wang and J. Qiu. *A review of organic nanomaterials in photothermal cancer therapy.* 2016.

[65] J. Wang and J. Qiu. A review of organic nanomaterials in photothermal cancer therapy. *Cancer Research Frontiers*. 2(1): 67-84, 2016.

[66] J. Wang. Controllable Synthesis of Gold Nanorod/Conducting Polymer Core/Shell Hybrids Toward in Vitro and in Vivo near-Infrared Photothermal Therapy. *ACS Applied Materials & Interfaces*. 10(15): 12323-12330, 2018.

[67] X.-H. Wang. Indocyanine green-platinum porphyrins integrated conjugated polymer hybrid nanoparticles for near-infrared-triggered photothermal and two-photon photodynamic therapy. *Journal of Materials Chemistry B*. 5(9): 1856-1862, 2017.

[68] X. Wang. Enhanced photothermal therapy of biomimetic polypyrrole nanoparticles through improving blood flow perfusion. *Biomaterials*. 143: 130-141, 2017.

[69] X. Wang. Fabrication of Ultralong and Electrically Uniform Single-Walled Carbon Nanotubes on Clean Substrates. *Nano Letters*. 9(9): 3137-3141, 2009.

[70] Y. Wang. Comparison Study of Gold Nanohexapods, Nanorods, and Nanocages for Photothermal Cancer Treatment. *ACS Nano*. 7(3): 2068-2077, 2013.

[71] R. Weissleder. A clearer vision for in vivo imaging. *Nature Biotechnology*. 19: 316, 2001.

[72] M.-C. Wu. Graphene-Based Photothermal Agent for Rapid and Effective Killing of Bacteria. *ACS Nano*. 7(2): 1281-1290, 2013.

[73] J.-W. Xu. Nanomaterials with a photothermal effect for antibacterial activities: an overview. *Nanoscale*. 2019.

[74] X. Xu. Controlled-temperature photothermal and oxidative bacteria killing and acceleration of wound healing by polydopamine-assisted Au-hydroxyapatite nanorods. *Acta Biomater*. 77: 352-364, 2018.

[75] K. Yang. Graphene in Mice: Ultrahigh In Vivo Tumor Uptake and Efficient Photothermal Therapy. *Nano Letters*. 10(9): 3318-3323, 2010.

[76] S. Yang. Multifunctional Bi@PPy-PEG Core–Shell Nanohybrids for Dual-Modal Imaging and Photothermal Therapy. *ACS Applied Materials & Interfaces*. 10(2): 1605-1615, 2018.

[77] Y. Yang. Nonchemotherapic and Robust Dual-Responsive Nanoagents with On-Demand Bacterial Trapping, Ablation, and Release for Efficient Wound Disinfection. *Advanced Functional Materials*. 28(21): 1705708, 2018.

[78] E. I. Yslas. Polyaniline nanoparticles for near-infrared photothermal destruction of cancer cells. *Journal of Nanoparticle Research*. 17(10): 389, 2015.

[79] C. Yue. IR-780 dye loaded tumor targeting theranostic nanoparticles for NIR imaging and photothermal therapy. *Biomaterials*. 34(28): 6853-6861, 2013.

[80] Z. Zha. Polypyrrole Hollow Microspheres as Echogenic Photothermal Agent for Ultrasound Imaging Guided Tumor Ablation. *Scientific Reports*. 3: 2360, 2013.

[81] Z. Zha. Uniform Polypyrrole Nanoparticles with High Photothermal Conversion Efficiency for Photothermal Ablation of Cancer Cells. *Advanced Materials*. 25(5): 777-782, 2013.

[82] B. Zhang. Fibrin-targeting peptide CREKA-conjugated multi-walled carbon nanotubes for self-amplified photothermal therapy of tumor. *Biomaterials*. 79: 46-55, 2016.

[83] Y. Zhao. Stable and Multifunctional Dye-Modified Black Phosphorus Nanosheets for Near-Infrared Imaging-Guided Photothermal Therapy. *Chemistry of Materials*. 29(17): 7131-7139, 2017.

[84] Z. Zhao. Bacteria-Activated Theranostic Nanoprobes against Methicillin-Resistant Staphylococcus aureus Infection. *ACS Nano*. 11(5): 4428-4438, 2017.

[85] V. P. Zharov. Photothermal Nanotherapeutics and Nanodiagnostics for Selective Killing of Bacteria Targeted with Gold Nanoparticles. *Biophysical Journal*. 90(2): 619-627, 2006.

[86] Y. Zhou. Photoresponsive Drug/Gene Delivery Systems. *Biomacromolecules*. 19(6): 1840-1857, 2018.

Bios

Emma Antonia Cuello

Emma Antonia Cuello obtained her B. Sc. in Chemistry from the National University of Río Cuarto (Argentina) in 2018. For her bachelor thesis she worked on the synthesis and characterization of smart materials for bacterial growth inhibition under supervision of Prof. Diego Acevedo. She is currently a second year PhD student under supervision of Prof. Cesar Barbero (National University of Río Cuarto). Her research program is focused on the development of actuators based on gel matrix nanocomposites for different technological applications.

Silvestre Bongiovanni Abel

Silvestre Bongiovanni Abel obtained both his B.Sc. (2013) and Ph.D. in Chemistry (2018) from the National University of Rio Cuarto (Argentina). He was a CONICET Postdoctoral fellow at INTEMA (CONICET-UNMdP) working in electrohydrodynamic techniques for the obtention of polymeric structures with controlled 3D architecture, under the supervision of Prof. Gustavo Abraham. In 2020, he joined the Responsive Polymer Therapeutics Group (POLYMAT, Basque Center for Macromolecular Design and Engineering, Spain) as a Postdoctoral Researcher. Recently, he was named Assistant Researcher of CONICET. His research interests include the synthesis and development of nanomaterials based on conducting and smart polymers for biomedical applications.

César Barbero

Dr. César Barbero received his B.Sc (1984, s.c.l.) and Ph.D. (1988, hons) in Chemistry from the National University of Rio Cuarto (UNRC, Argentina). After a postdoctoral stay (1988-1994) at Paul Scherrer Intitute (Switzerland), he returned to the UNRC to become an Assistant Professor. At present, he is Full Professor in Chemistry and Superior Researcher of the National Science Council (CONICET), Argentina. He is the Director of the Research Institute on Energy Technologies and Advanced Material (UNRC-CONICET). He has advised 13 Ph.D. thesis, published over 180 manuscripts (h=34) and holds 6 patents. He received the Tajima Prize of the International Society of Electrochemistry (1997).

Inés Yslas

Dr. E. Inés Yslas received a degree in Microbiology from the National University of Río Cuarto (UNRC, Argentina) in 2000. In 2002, she obtained a CONICET Fellowship to undertake her PhD studies working on photodynamic therapy in cancer. From 2006 to 2008 she was a CONICET postdoctoral fellow, working on photothermal therapy in cancer. Since 2008, she is a scientific researcher of CONICET at the UNRC working in photothermal therapy in bacterial infections and antibacterial surfaces.

María Molina

Dr. María Molina received her BSc (Hons) in Chemistry from the Universidad Nacional de Rio Cuarto (UNRC, Argentina) in 2007. Also in 2007, she obtained a CONICET Fellowship to undertake her PhD studies (2011) in Prof. Cesar Barbero's group (UNRC) working on the preparation of smart hydrogels as drug delivery systems. From 2012 to 2015, she was an Alexander von Humboldt postdoctoral fellow at Freie Universität Berlin, under the supervision of Prof. M. Calderón and Prof. R. Haag. Since 2017, she is a research scientist of CONICET at the UNRC. She received the International Rising Talents Awards from Loreal-UNESCO For Women in Science program in 2019.

Block Copolymer Micelles Generated by Crystallization-Driven Self-Assembly in Polymer Matrices

Jessica Gutiérrez González,[1] Ruth N. Schmarsow,[1] Úrsula M. Montoya Rojo,[2,3] Julieta Puig,[1] Walter F. Schroeder,[1] and Ileana A. Zucchi[1]*

[1] *Instituto de Investigaciones en Ciencia y Tecnología de Materiales (INTEMA), Universidad Nacional de Mar del Plata (UNMdP)-Consejo Nacional de Investigaciones Científicas y Técnicas (CONICET), Argentina.*
[2] *Grupo de Biotecnología y Biosíntesis. Instituto de Tecnología en Polímeros y Nanotecnología (ITPN-UBA-CONICET), Facultad de Ingeniería, Universidad de Buenos Aires, Argentina*
[3] *Departamento de Tecnología Industrial, Facultad de Ingeniería, Universidad de Buenos Aires, Argentina*
* Corresponding author. E-mail: ileanazu@yahoo.com.ar

Abstract

In this review, we show how Crystallization-Driven Self-Assembly (CDSA), a method originally employed for the self-assembly of block copolymers in solution, was extended to the synthesis of elongated micellar nanostructures in polymer matrices. By highlighting some of the works published by our group in this area, the conditions to synthesize nanostructured polymers by CDSA are discussed. The knowledge of these conditions will allow developing a new generation of nanomaterials with tailored architecture based on a given application.

Keywords:
block copolymer, epoxy, micelles, nanoribbons, self-assembly, vesicles
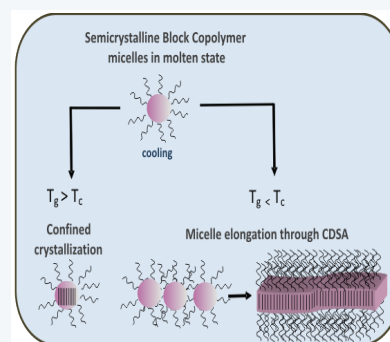
Introduction

The ability of block copolymers (BCP) to form a variety of nanoscale periodic patterns through self-assembly offers a powerful tool for the 'bottom-up' fabrication of nanostructures with different levels of ordering. A BCP consists of two or more polymeric chains (blocks), which are chemically different and covalently attached to each other. If the constituent polymers are immiscible, phase separation is induced on a scale that is directly related to the size of the copolymer chains and results in ordered structures with a domain spacing in the range of 10 to 100 nm. The order/disorder transition temperature and the specific pattern formed by a given BCP are functions of the molecular weight, the strength of interaction between the blocks (represented by the Flory–Huggins interaction parameter,χ), and the volumetric composition. In particular, volumetric composition strongly influences microphase morphology. For example, diblock copolymers with segments of comparable volume exhibit a lamellar morphology. Increasing the degree of compositional asymmetry leads to the gyroid, cylindrical, and finally, spherical phases.

When a BCP is dissolved in a selective solvent, *i.e.*, a good solvent for one of the blocks but poor solvent for the other, the BCP self-assembles into micelles. The immiscible block forms the core, while the miscible block forms the corona. The micellar morphology obtained depends on several factors such as length of the blocks, concentration, thermodynamic compatibility between block-solvent and block-block, and temperature (Bang *et al.* 2009; Wu *et al.* 2005). When the blocks forming the BCP are amorphous, typical micelle structures include spheres, cylinders, lamellar bilayers

and vesicles (Hayward and Pochan, 2010; Mai and Eisenberg, 2012). However, it is possible to access to other type of micellar morphologies when the immiscible block is able to crystallize. In this case, crystallization competes with microphase separation in the self-assembly process. (He and Xu, 2012a) When crystal packing forces dominate, a morphological transformation into a novel structure is triggered through a reorganization mechanism called crystallization-driven self-assembly (CDSA). This mechanism normally leads to elongated nanostructures, either with planar cross-sections (nanoribbons or platelet-like structures) or with circular cross-sections (fibers, cylinders). The morphology developed is affected by crystallization temperature and time, solvent quality, core/corona volume ratio and composition (Crassous *et al.* 2015). Thus, a large variety of morphologies can be prepared by adjusting the crystallization conditions under which semi-crystalline micelles are obtained. Based on this concept, CDSA has emerged as a powerful method for the preparation of well-defined micellar structures with controlled dimensions. A significant number of articles describing the preparation of these elongated nanostructures in solution has been published in recent years. For example, Winnik and Manners found that poly(ferrocenylsilane) (PFS)-based block copolymers self-assemble into cylindrical micelles (Guerin *et al.* 2014; Shen *et al.* 2008; Wang *et al.* 2007) or tape-like nanostructures (Cao *et al.* 2002) when they are dispersed in alkane solvents. Due to their remaining active ends, these micelles can be elongated, in a controlled manner, through the addition of further block copolymer unimers. It was argued that the process is driven by epitaxial crystallization of the core-forming PFS block on the preformed seed micelles (Boott *et al.* 2018; Guerin *et al.* 2018). In other examples, analogous elongated structures with crystallizable organic cores based on poly(ethylene oxide) (PEO) (Mihut *et al.* 2010), poly(ε-caprolactone) (PCL), (He *et al.* 2012b) and poly(ethylene) (PE) (Yin *et al.* 2012), were prepared in a controlled way by regulating parameters such as cooling rate and crystallization temperature.

The extension of the original concept of BCP self-assembly in solution to the preparation of nanostructured polymer materials involves the replacement of the selective solvent by reaction precursors. The premise that systems based on blends of diblock or triblock copolymers and reaction precursors must meet to avoid macro phase separation is that at least one of the blocks of the BCP must remain miscible with the matrix during the reaction or it is expelled only on a local scale. Two mechanisms have been identified for the formation of nanostructures depending on the miscibility of the non-affine block of the copolymer with the matrix before and after curing: initial self-assembly and reaction induced microphase separation (RIMPS). With the first mechanism, self-assembled nanophases are present before curing. This occurs when the non-affine block is immiscible in reaction precursors and, consequently, it is phase-separated from the start of the polymerization process. In this case, the role of curing is to "freeze" the existing nanostructure. A variety of BCP architectures have been used to obtain ordered (or disordered) nanostructures through this strategy (Guo *et al.* 2003a; Lipic *et al.* 1998a; Wu *et al.* 2005). However, in many instances the blocks are miscible in reaction precursors. With the second mechanism, RIMPS, the BCP is initially dissolved in the reactive solvent and the non-affine block phase separates during the polymerization generating the self-assembled nanophases (Meng *et al.* 2006a).

During the synthesis of nanostructured polymers from a crystallizable BCP, either by initial self-assembly or through the RIMPS mechanism, the nanostructure generated could undergo a morphological transformation to a novel structure through CDSA. This possibility is strictly related to the mobility of the matrix at the time when the crystallization of the immiscible block occurs (Montoya Rojo *et al.* 2019; Schmarsow *et al.* 2019). For example, when polymerization occurs *above* the melting temperature of the immiscible block, crystallization takes place during the final cooling step. Guo *et al.* (Guo *et al.* 2003b) analyze this situation. They employed PE-*b*-PEO (M_n = 1400; 50 wt % PEO) dispersed in a matrix based on diglycidyl ether of bisphenol A (DGEBA). The cure was performed in steps from 120 ºC to 180 ºC (above the melting temperature of PE, which is around 100ºC). For contents up to 30 wt% BCP, spherical micelles were present during curing, while confined crystallization took place by homogeneous nucleation inside the spherical micelles during the cooling step. Similar results were reported by other authors employing PE-*b*-PEO (Tercjak *et al.* 2006) or PCL-*b*-PE-*b*-PCL (M_n = 31000 with 35 wt % PE, where PCL was the miscible block) (Zhang *et al.* 2013). In all these previous studies, epoxy networks with high glass transition temperature (T_g) were selected. As a result, vitrification of the epoxy matrix took place before crystallization during the cooling step. This fixed the nanostructure generated at high temperatures and enabled crystallization to occur in confined domains with rigid boundaries. A different and less studied situation occurs when the T_g of the epoxy network is lower than the crystallization temperature of the immiscible block. (Puig *et al.* 2016; Schmarsow *et al.* 2019) In this case, there is a temperature gap between the crystallization and the glass transition of the matrix where CDSA may take place. The size of such temperature gap, which is a measure of the mobility of the matrix, will determine the effect of CDSA on the morphology generated during the cooling step, as will be discussed in this manuscript.

The scenario is different when polymerization occurs *below* the crystallization temperature of the immiscible block. In this case, two situations could occur. First, if the non-affine block is completely immiscible in reaction monomers, the initial blend will consist of a dispersion of crystalline nanostructures stabilized by the miscible block. In this case, nanostructures are formed through CDSA in the initial blend (Zucchi and Schroeder, 2015; Sinturel *et al.* 2007, 2009). Sinturel *et al.* (Sinturel *et al.* 2007, 2009) employed this mechanism to obtain PE-*b*-PEO platelets with a high aspect ratio (6 nm thick, 500 nm to 1 m long) constituted of a crystalline PE core, bordered by PEO domains dispersed in cross-linked unsaturated polyester. The second situation occurs when both blocks of the BCP are miscible in reaction monomers and

nano-structuration takes place by RIMPS. At the moment, this case remains practically unexplored. Here, the core-forming block can crystallize during polymerization and different nanostructures can be generated depending on the mobility of the matrix when crystallization occurs (Montoya Rojo *et al.* 2019). The competition between crystallization and polymerization kinetics defines the micellar morphology that develops. This case is particularly interesting since morphologies can be precisely tailored by manipulating curing conditions.

From the discussion above, it is clear that the incorporation of crystallizable polymers as the immiscible core-forming block provides opportunities toward nanostructures with additional structural features. The crystallization energy from the core is responsible for this behavior. The aim of this paper is to review some recent works related to BCP self-assembly in polymer matrices in which the crystallization of the immiscible block plays a critical role in micellar morphology development.

1. PE-*b*-PEO self-assembly in an epoxy matrix

We will begin by showing the results obtained when 10 wt % of polyethylene-*block*-poly(ethylene oxide) (PE-*b*-PEO, Mn = 1400 and 50 wt% ethylene oxide content) was dispersed in a polymer matrix based on diglycidyl ether of bisphenol A (DGEBA). In this case, the PE block is immiscible with DGEBA and can easily crystallize (Guo *et al.* 2003b), whereas the PEO block is completely miscible with DGEBA before and after the curing reaction (Meng *et al.* 2006b). Consequently, BCP nanostructures are formed through the *initial self-assembly* mechanism.

Firstly, the neat BCP was thermally characterized. Figure 1 shows the DSC cooling scan from the melt and the subsequent heating scan for the pure PE-*b*-PEO. The DSC cooling scan displays a broad distribution of exothermic events with a main peak at 95.9 °C attributed to the crystallization of the PE blocks, and an exothermic peak at 16.4°C attributed to the crystallization of the PEO blocks. This crystallization behavior of the PE blocks is commonly observed in PE-based copolymers obtained via polybutadiene hydrogenation. The DSC subsequent heating scan shows the melting peak of the PEO crystals as an endothermic peak at 30.4 °C, and the melting behavior of the PE crystals as a wide endothermic peak with the minimum at 103.8 °C.

As we previously mentioned, the PE block is immiscible while the PEO block is completely miscible with DGEBA. This marked amphiphilicity induces the formation of micelles with PE core and PEO corona when the BCP is dispersed in DGEBA. The polymerization of DGEBA transfers the obtained micellar dispersion to a cross-linked epoxy matrix. However, the micellar architecture adopted in the thermoset is deeply determined by the conditions in which crystallization occurred. Two different situations can occur. When curing is performed above the melting temperature of the PE block, nanostructures are formed in the molten state during curing, and crystallization occurs during the subsequent cooling step. On the contrary, when curing is carried out at a temperature below the melting transition of the PE block, a dispersion of micelles with already crystallized PE core is present in the initial mixture. These two different scenarios were explored and are summarized below.
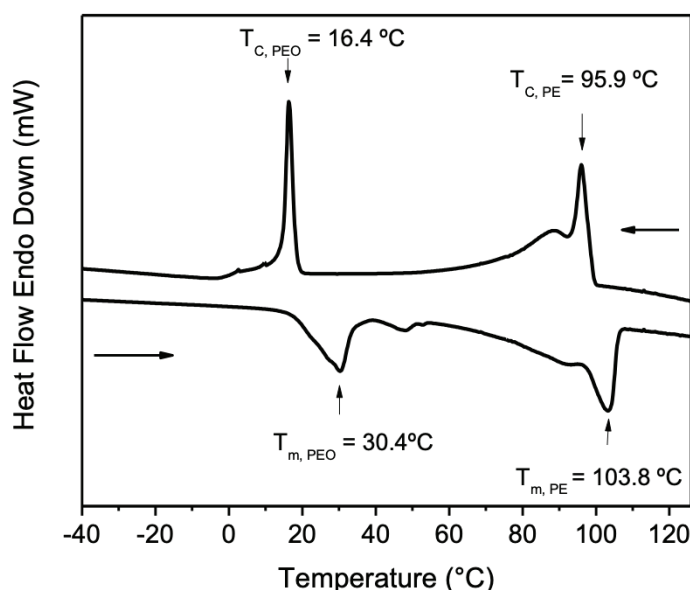

Figure 1. DSC scans at 10 °C/min of the cooling (above) and subsequent heating (below) for the pure PE-*b*-PEO block copolymer.

1.1. Thermal curing of DGEBA at 120 ºC

To investigate the morphologies obtained when curing was performed above the melting temperature of the PE block, DGEBA was homopolymerized by an anionic mechanism using a tertiary amine benzyldimethylamine (BDMA) as initiator (in a molar ratio with respect to epoxy groups equal to 0.06). The reaction was carried out at 120 °C. At this temperature, 2 hours of reaction were sufficient to achieve complete conversion. Figure 2(a) shows a TEM image of RuO_4-stained sample of the fully cured blend containing 10 wt % BCP. The presence of micelles with ellipsoidal contours of approximately 20 nm in length is observed in the TEM image. PEO blocks are preferentially stained by RuO_4, compared to the PE cores and the epoxy matrix (Trent et al. 1983), therefore PEO-rich regions (contour of the micelles) appear darker in the TEM image.
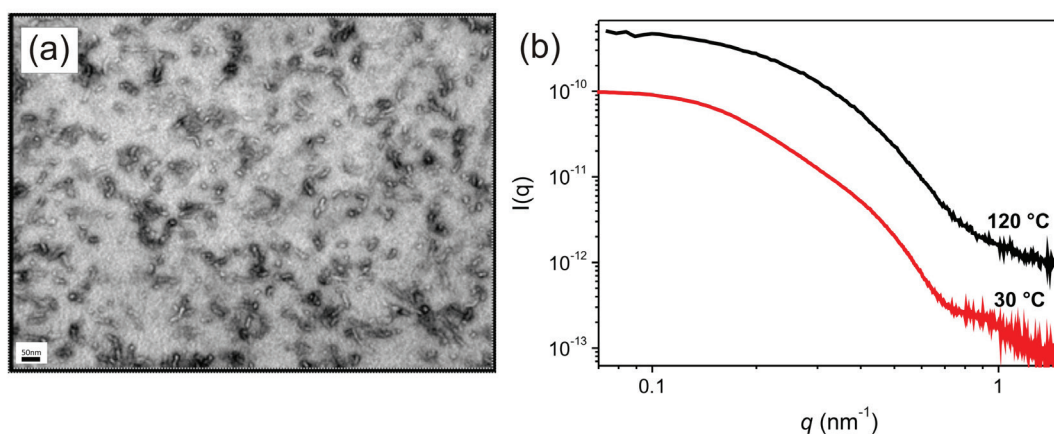

Figure 2. (a) TEM image of the fully cured blend containing 10 wt % PE-*b*-PEO, scale bar 50 nm. **(b)** SAXS data obtained after polymerization at 120 °C and subsequent cooling to 30ºC of 10 wt % PE-*b*-PEO/epoxy blend. [Puig, J.; Zucchi, I. A.; Ceolín, M.; Schroeder, W. F.; Williams, R. J. J. *RSC Adv* **2016**, *6* (41), 34903-34912] Reproduced by permission of The Royal Society of Chemistry.

The SAXS curve recorded at 120 °C, after the reaction and before the cooling step, is displayed on Figure 2(b) (top curve). Curves were fitted using the SASfit software package, in the region from 0.08 to 0.5 nm^{-1} (where the contribution of the neat matrix showed a negligible intensity). The analysis of SAXS data required a population of short cylinders with an average diameter of 8 nm and average length of 23 nm. These cylinders, which are one of the typical nanostructures generated when polymerization is carried out above the melting temperature of the immiscible block, were generated during thermal curing at 120ºC.

Then, it was investigated whether the crystallization-driven self-assembly of PE blocks produced any change in the morphology when cooling the cured material from 120 ºC to room temperature. The bottom curve in Figure 2(b) displays the SAXS curve of the fully cured blend after cooling to 30 ºC. The fitting required to assume the presence of a polydisperse distribution of planar objects (disk-like micelles) with an average diameter d_{disks} = 23.1 nm and thickness h = 6.7 nm. The thickness is close to the theoretical value of fully extended PE chains (Parikh et al. 1999). IR spectroscopy confirmed the *all-trans* conformation of PE chains. Therefore, crystals were formed by interdigitated PE chains, with PEO blocks tethered at both planar interfaces in an alternating way. SAXS analysis together with TEM image (Figure 2(a)), allowed to conclude that planar nanostructures can be described as disk-like micelles with ellipsoidal contours that preserve the original size of the cylinders. Cooling led to a change in shape of the individual micelles, from nano-rods to disk-like objects, promoted by the crystallization of PE chains.

As it was mentioned before, during the crystallization of the immiscible block the matrix should have enough molecular mobility to allow the CDSA mechanism to operate. A measure of such molecular mobility is given by the temperature gap between the crystallization of PE blocks and the glass transition of the matrix $(_{Tc,PE}-T_{g,matrix})$. The DSC heating and cooling scans of the fully cured blend containing 10 wt % PE-*b*-PEO allow measuring such temperature gap, see Figure 3. The heating scan showed the T_g of the plasticized epoxy at 58 ºC (onset value), which was significantly lower than the value for neat epoxy (81 ºC, not shown) due to PEO plasticization. PE crystals melted at 98 ºC (minimum of the endothermic peak). The cooling scan showed a crystallization peak at 65 ºC. Therefore, this blend exhibited a very narrow temperature gap, from about 70 ºC (onset of crystallization) to 58 ºC, to produce CDSA. This temperature gap only allowed flattening of the domains, but not elongation of the nanostructure.
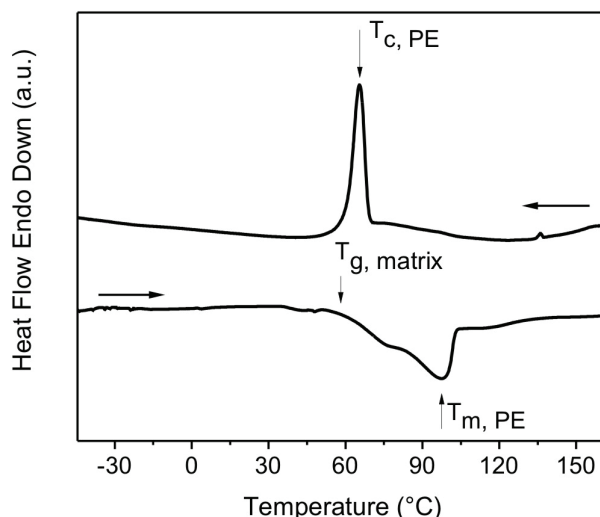
Figure 3. DSC thermogram in heating and cooling scans at 10 ºC/min for the cured blend with 10 wt % PE-*b*-PEO. [Puig, J.; Zucchi, I. A.; Ceolín, M.; Schroeder, W. F.; Williams, R. J. J. *RSC Adv* **2016**, *6* (41), 34903-34912] Reproduced by permission of The Royal Society of Chemistry.

1.2. Photopolymerization of DGEBA at room temperature

To investigate the morphologies obtained when curing temperature is below the melting transition of the PE block, epoxy monomers were photocured at room temperature by photoinitiated cationic ring-opening polymerization. The resin was activated for visible light polymerization by adding a three-component photoinitiating system based on *p*-(octyloxyphenyl) phenyliodonium hexafluoroantimonate (Ph_2ISbF_6, 2 wt %), camphorquinone (CQ, 1 wt %) and ethyl-4-dimethyl aminobenzoate (EDMAB, 1 wt %). Under these conditions, DGEBA undergoes very slow polymerization at room temperature. Between three and four days of irradiation were required to reach a high enough conversion level.
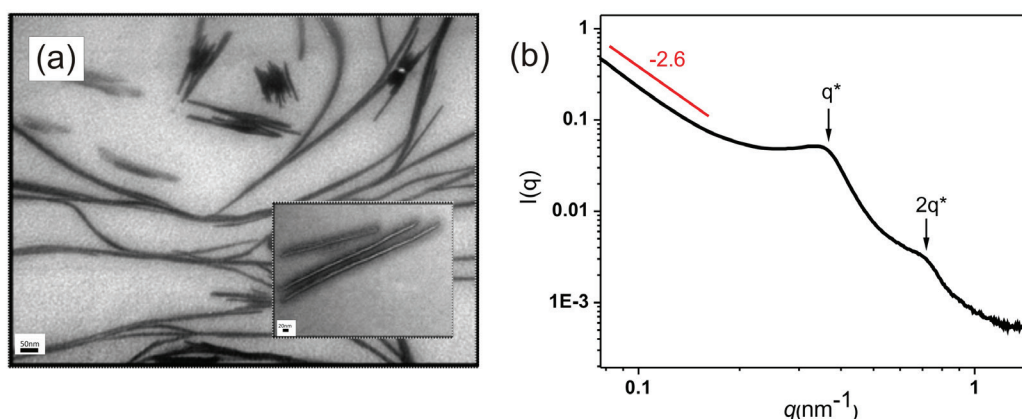

Figure 4. (a) TEM images of RuO_4-stained section of the photocured blend with 10 wt % PE-*b*-PEO, scale bar 50 nm. Inset: TEM image of the same sample at a higher magnification, scale bar 20 nm. **(b)** SAXS profile of the photocured blend with 10 wt % PE-*b*-PEO.

Figure 4(a) shows TEM images of RuO_4-stained sections of the photocured sample containing 10 w% BCP. A dispersion of nanoribbons with semi-crystalline core dispersed in the epoxy matrix was obtained. As explained above, PEO is preferentially stained by RuO_4 compared to PE and DGEBA; therefore, PEO-rich regions look darker in the TEM image (Trent *et al.* 1983). Furthermore, the staining technique allows clearly distinguishing the location of the blocks in the structure. The TEM image at higher magnification (inset in Fig. 4(a)) shows micelles viewed edge-on exhibiting the PEO corona as darker lines surrounding the PE core (lighter line). An interesting feature of these ribbon-like micelles was their tendency to aggregate, resulting in the formation of face-to-face stacking of micelles as shown in Figure 4(a). This

association effect may be driven by the attractive van der Waals interaction between different nanoribbons. SAXS measurement was carried out to extract complementary structural information, Figure 4(b). The first interesting feature is the low-q slope, which was equal to -2.6, evidencing the presence of elongated planar nanostructures. The pattern presented a main peak located at a value of the scattering vector $q^* = 0.38$ nm^{-1}, corresponding to an average spacing of 16.5 nm. This main peak was accompanied by a well-defined higher order reflection located at $q_i/q^* = 2$, where q^* is the primary peak position. Such a sequence is characteristic of a lamellar arrangement. The results from the combination of TEM and SAXS allow to conclude that the ribbon-like micelles adopted face-to-face packing into lamellar arrangements with an average period of 16.5 nm.
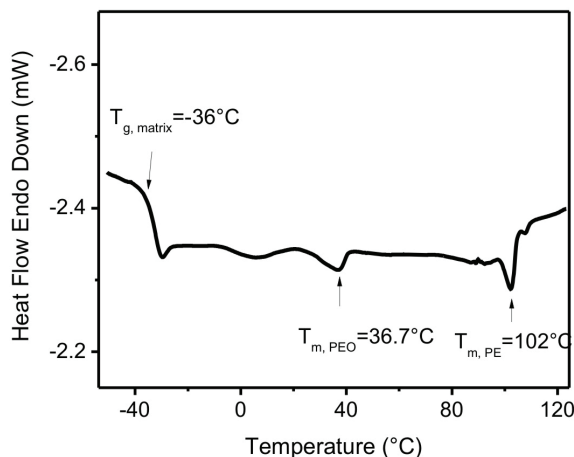

Figure 5. DSC thermogram in heating scan at 10ºC/min of the initial 10 wt % PE-*b*-PEO/DGEBA blend.

In the mixture that was photopolymerized at room temperature, crystallization of PE blocks took place in the reactive monomers before polymerization, while the subsequent curing preserved the crystalline structure of the generated micelles. In this case, the temperature gap for crystallization-driven self-assembly ($T_{c,PE}$ - $T_{g,matrix}$) was 138°C, which corresponds to the difference between the crystallization temperature of PE blocks (102°C) and the glass transition of the monomers (-36°C), as shown in Figure 5. For this large temperature gap, long crystalline nanoribbons of several microns in length were obtained in the initial mixture. These nanoribbons were subsequently frozen by the photocuring reaction of the matrix.

1.3. Combined Thermal- and Photo-Curing

The results presented in these two previous sections highlight the crucial role of matrix mobility during immiscible PE blocks crystallization in the elongation process of the planar nanostructures, where the temperature gap ($T_{c,PE}$ - $T_{g,matrix}$) provides a measure of such mobility.

On the basis of this finding, it was proposed to obtain a dispersion of nanoribbons with precisely controlled length by regulating the temperature gap ($T_{c,PE}$ - $T_{g,matrix}$) during PE blocks crystallization. For this, a dual thermal- and photo-curing system was adopted, which allowed initiating the epoxy polymerization at 120 ºC until a certain degree of conversion, stopping the reaction by cooling to induce micellar elongation and crystallization, and then continuing the polymerization process at room temperature by visible-light irradiation. In this way, PE blocks crystallization took place in a matrix whose mobility was controlled by the degree of conversion reached at 120 ºC. Figure 6 shows the temperature gap between the main peak crystallization temperature of PE blocks ($T_{c,PE}$) and glass transition temperature of the epoxy matrix ($T_{g,matrix}$) measured from DSC scans, as a function of the conversion degree reached during the thermal polymerization step (xt) for a sample with 10wt% BCP. As observed in Figure 6, matrix mobility can be effectively manipulated by regulating the degree of conversion reached at 120°C.
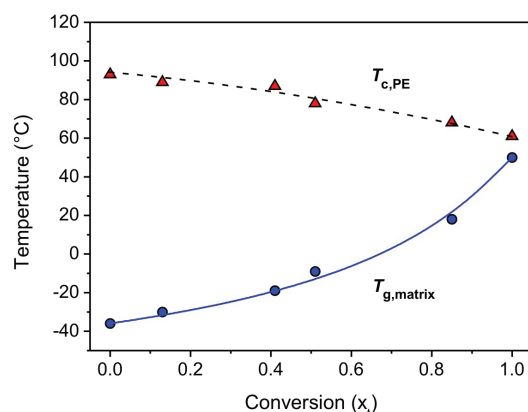
Figure 6. Main peak crystallization temperature of PE blocks ($T_{c,PE}$, red triangles) and glass transition temperature of the epoxy matrix ($T_{g,matrix}$, blue circles) obtained from DSC scans versus conversion. The blue solid line represents the evolution of $T_{g,matrix}$ predicted by equation $(T_g - T_{g0})/(T_{g\infty} - T_{g0}) = \lambda x/[1 - (1 - \lambda)x]$, with $\lambda = 0.348$, $T_{g0} = -36$ °C and $T_{g\infty} = 50$ °C. The dashed line was drawn to guide the eye. [Schmarsow, R. N.; Ceolín, M.; Zucchi, I. A.; Schroeder, W. F. *Soft Matter* 2019, 15, 4751-4760] Reproduced by permission of The Royal Society of Chemistry.

Figure 7 shows TEM images of the materials obtained with different conversion degrees reached during the thermal polymerization step. For comparison purposes, the images are shown at the same magnification. The sectioned specimens were stained with RuO_4 prior to TEM observation. As it can be seen, average micelle length decreased progressively as x_t increased. These results confirmed that average micelle length decreased as the difference between $T_{c,PE}$ and $T_{g,matrix}$ decreased, which was a consequence of medium mobility loss during the crystallization process. The dimensions obtained by TEM analysis were consistent with the visual appearance of the samples. Figure 7 (insets) shows photographs of the prepared materials. As it can be observed, the fully photocured sample ($x_t = 0$) was opaque due to the presence of ribbon-like micelles with lengths at the micron scale. With increasing x_t, there was a gradual decrease in opacity, indicating that micelle size progressively decreased below the wavelength of visible light. For $x_t = 0.85$ and 1, the samples were fully transparent, as expected for a dispersion of nanoscale objects.
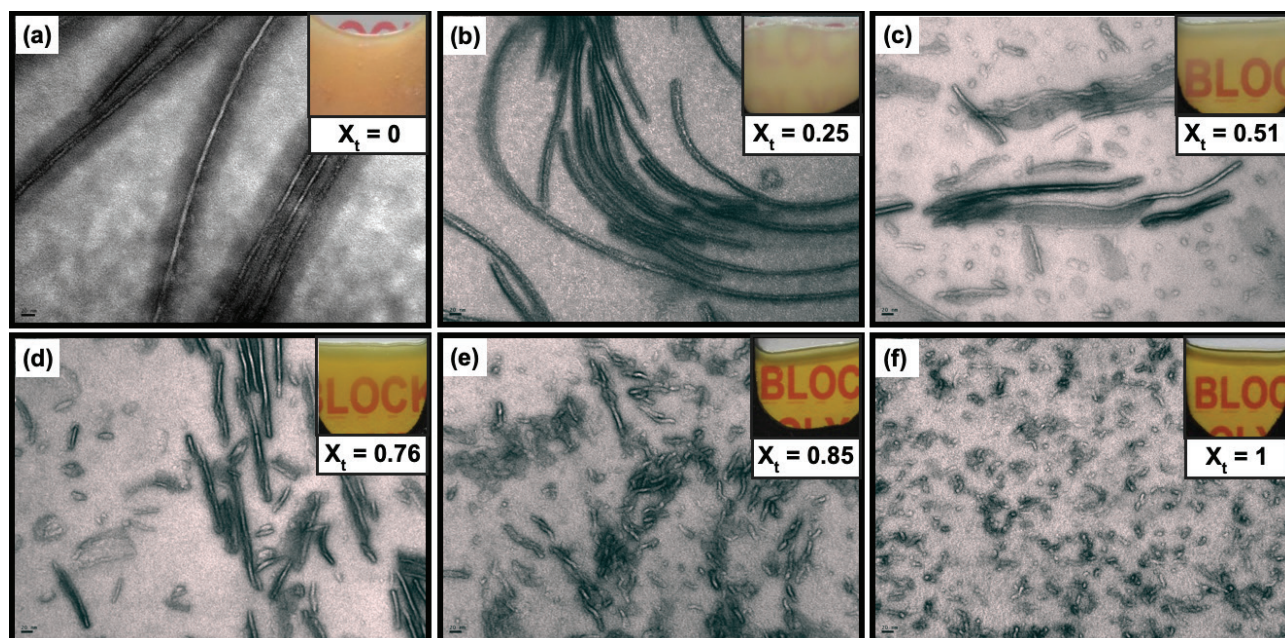

Figure 7. TEM images of materials with 10 wt % PE-*b*-PEO obtained with different conversion degrees achieved during the thermal polymerization step (x_t). Sectioned specimens were stained with RuO_4 prior to the TEM observations. In all the images, the scale bar represents 20 nm. The insets show photographs of the corresponding materials. (a) $x_t = 0$; (b) $x_t = 0.25$; (c) $x_t = 0.51$; (d) $x_t = 0.76$; (e) $x_t = 0.85$; and (f) $x_t = 1$. [Schmarsow, R. N.; Ceolín, M.; Zucchi, I. A.; Schroeder, W. F. *Soft Matter* 2019, 15, 4751-4760] Reproduced by permission of The Royal Society of Chemistry.

These results showed that ribbon-like micelles with precisely controlled length can be obtained through a crystallization-driven self-assembly mechanism. Micellar length can be precisely tailored by regulating $T_{c,PE}$-$T_{g,matrix}$. Figure 8 summarizes the preparation conditions that lead to the length-controlled planar nanostructures.
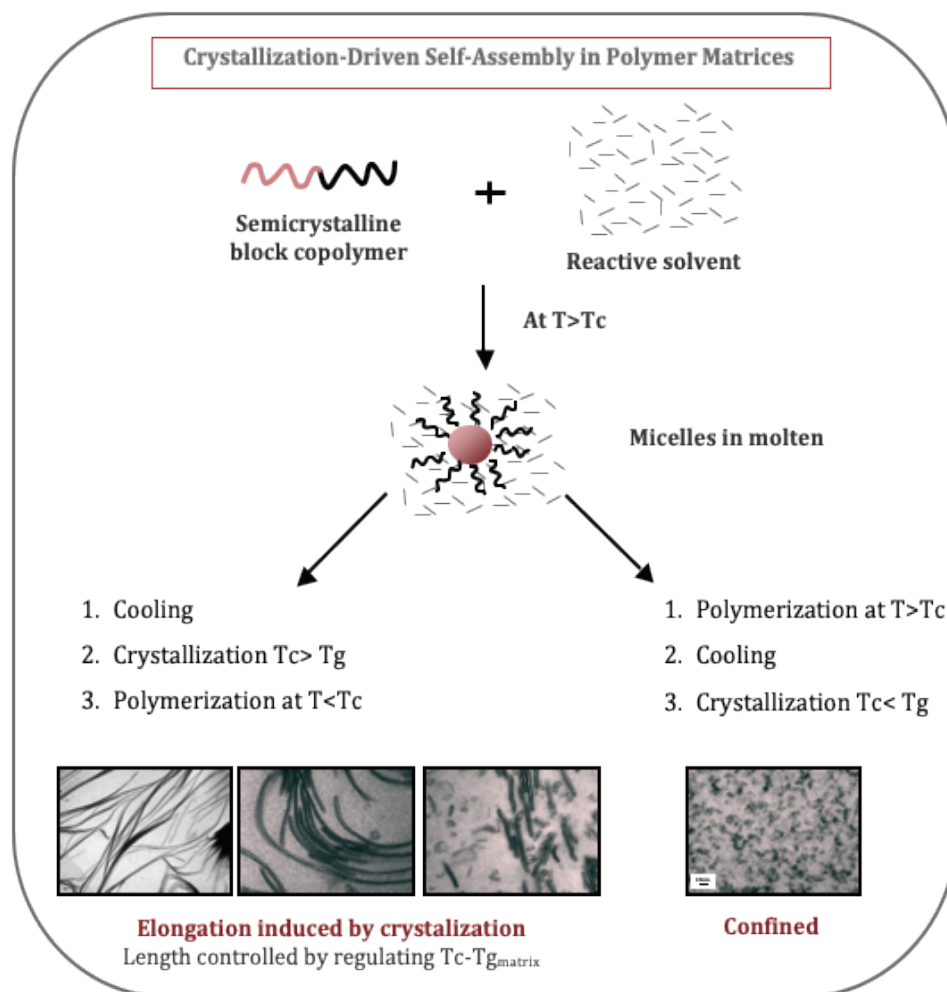

Figure 8. Schematic representation of the different pathways followed for the preparation of the elongated micelles.

2. PS-*b*-PCL self-assembly in a polystyrene matrix

We will continue by analyzing a completely different scenario. In this case, with the goal of reducing the crystallization ability of the immiscible block, PCL was used as core-forming block in an amphiphilic combination with PS. The BCP employed was Poly(styrene-block-ε-caprolactone) (PS-*b*-PCL) with 38 wt % PCL and Mn= 47,000 g/mol (Mw/Mn = 1.02). Consequently, the reactive solvent must be non-affine with PCL to cause its de-mixing and therefore the self-assembly. Taking this into account, the selected reactive solvent was styrene (St), which was a good solvent for both blocks before reaction, but became a poor solvent for the PCL block during the polymerization. This condition shows that the system will be nanostructured by the *RIMPS* mechanism. Samples were prepared at two different temperatures of polymerization, 90 and 20 °C, i.e. above and below the melting temperature of the PCL block.
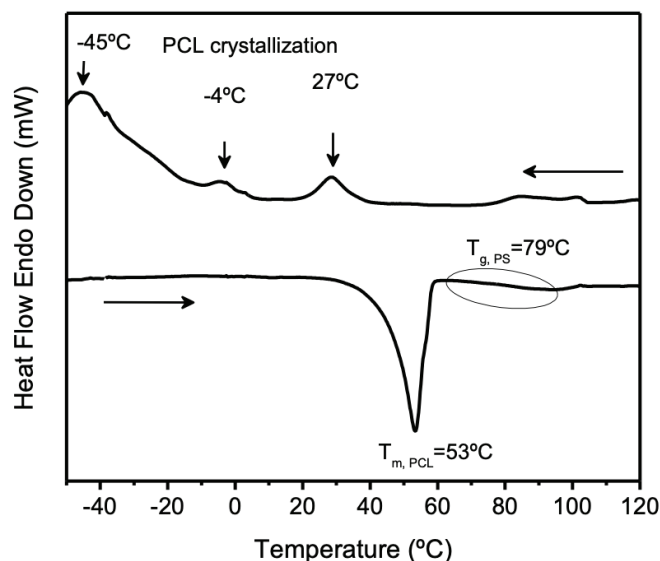
Figure 9. DSC scans at 10 ℃/min of the cooling phase (top) and subsequent heating (down) for the pure PS-*b*-PCL block copolymer. Reprinted from *Eur. Polym. J.*, *112*, Montoya Rojo, Ú. M.; Riccardi, C. C.; Ninago, M. D.; Ciolino, A. E.; Villar, M. A.; Ceolín, M.; Zucchi, I. A.; Schroeder, W. F., Photopolymerization-Assisted Self-Assembly as a Strategy to Obtain a Dispersion of Very High Aspect Ratio Nanostructures in a Polystyrene Matrix, 704–713, Copyright (2019), with permission from Elsevier.

As a reference, DSC curves for the neat PS-*b*-PCL were first analyzed, see Figure 9. According to its volumetric composition, this block copolymer self-assembles into cylinders of PCL dispersed in a matrix of PS. In the cooling DSC scan shown in Figure 9, several crystallization exotherms were observed, with distinguishable peaks at 27, -4 and -45 ℃. This behavior was ascribed to a fractionated crystallization phenomenon produced by the confinement of PCL into isolated cylindrical microdomains and by the existence of different nucleation events within such microdomains (Michell and Müller, 2016). Typically, this phenomenon occurs when the number of microdomains is larger than the number of heterogeneities available to produce nucleation. Therefore, the exothermic peak at 27 ℃ was assigned to the crystallization of microdomains containing highly active heterogeneities (those commonly present in bulk PCL), while the exothermic peak at -4 ℃ was related to the crystallization of microdomains with less active heterogeneities, which required a higher degree of supercooling. The peak at -45 ℃ was ascribed to the heterogeneity-free microdomains that crystallized by a homogeneous nucleation process. Note that the homogeneous nucleation should occur at the maximum degree of supercooling just before vitrification (T_g of PCL is approximately -60 ℃). (Tiptipakorn *et al.* 2015) DSC subsequent heating scan (Figure 9) presented an endothermic peak at 54 ℃ due to the melting of PCL crystals, followed by the T_g of PS blocks at 79 ℃ (onset value).

2.1. Thermal Polymerization at 90 ℃

Firstly, the self-assembly behavior of the PS-b-PCL during St polymerization at 90 ℃ was examined. The polymerization was carried on employing benzoyl peroxide (2 wt %) as thermal initiator. Under the selected polymerization conditions, almost full conversion of vinyl double bonds was achieved after 70 min reaction.

Previous studies performed using a PCL homopolymer with a molar mass similar to that of the PCL block in the BCP, confirmed that PCL was initially miscible in St monomer and phase separated during polymerization at a conversion degree between 0.1 and 0.2. Consequently, in the blend containing 10 wt % PS-*b*-PCL, although both blocks (PCL and PS) were initially miscible with the St monomer, the PCL block will phase separate during St polymerization, resulting in self-assembled structures driven by the RIMPS mechanism. Figure 10(a) shows a RuO$_4$-stained TEM micrograph of the sample with 10 wt% PS-*b*-PCL polymerized at 90 ℃. As it can be seen, the micrograph reveals the presence of a population of nanorods dispersed in the PS matrix, with the PS blocks forming the corona of the micelles and the PCL blocks forming the core. The contour length of these micelles ranged from 30 to 220 nm.
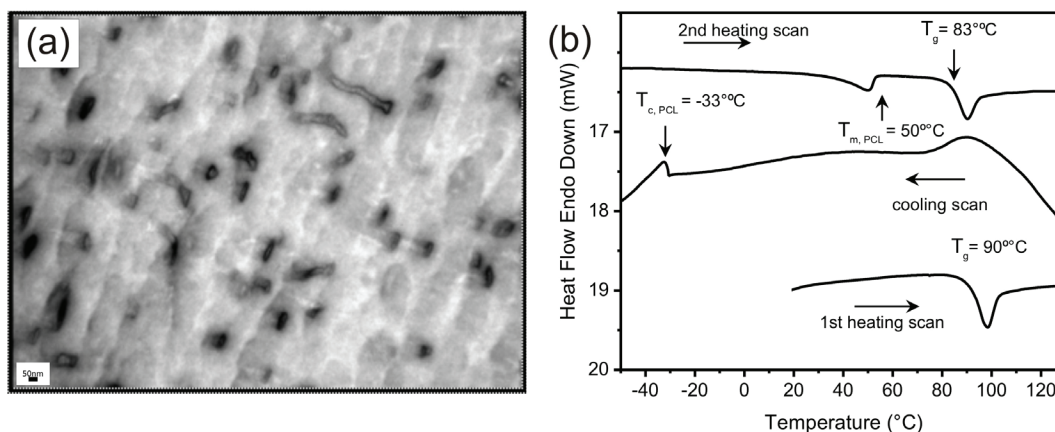
Figure 10. (a) TEM image of the blend with 10 wt % PS-*b*-PCL cured at 90ºC. The specimen was stained with RuO$_4$ prior to the TEM observation. Scale bar 50 nm. **(b)** DSC heating and cooling scans of the fully cured blend with10 wt % PS-*b*-PCL. Reprinted from *Eur. Polym. J.*, *112*, Montoya Rojo, Ú. M.; Riccardi, C. C.; Ninago, M. D.; Ciolino, A. E.; Villar, M. A.; Ceolín, M.; Zucchi, I. A.; Schroeder, W. F., Photopolymerization-Assisted Self-Assembly as a Strategy to Obtain a Dispersion of Very High Aspect Ratio Nanostructures in a Polystyrene Matrix, 704–713, Copyright (2019), with permission from Elsevier.

Figure 10(b) shows DSC runs of the cured sample. The first heating scan (at 10ºC/min), performed from room temperature to 130 ºC, exhibited only a thermal transition associated to the glass transition of the matrix (T$_g$=90ºC). The absence of a melting peak corresponding to phase-separated PCL blocks indicated that the crystallization of these blocks did not occur during cooling of the sample to room temperature after polymerization. In fact, DSC tests were periodically performed in order to investigate whether confined crystallization of PCL cores took place during sample annealing at room temperature, but crystallization was not detected after four months of annealing. However, PCL crystallization was detected when the sample was subjected to large undercoolings during the subsequent cooling scan. On the basis of these results, it can be understood that PCL blocks were purified by recrystallization during the RIMPS process, resulting in heterogeneity-free microdomains that crystallized by a homogeneous nucleation phenomenon. Consequently, the crystallization peak at 27ºC was suppressed and crystallization occurred at -33ºC. Rod-like micelles with an amorphous PCL core dispersed in a PS matrix were the result of thermal curing at 90°C. A different situation occurred when the reaction was performed at a temperature below the melting temperature of the core-forming block. In this case, the immiscible block was able to crystallize during the polymerization reaction and crystal packing forces played a dominant role in determining the morphology of the nanostructures that were formed. This case is analyzed in the following section.

2.2. Photopolymerization at Room Temperature

When polymerization is carried out below melting transition of the demixing block, it can crystallize during the reaction. This is a particularly interesting case because the morphology could be manipulated by controlling the curing conditions.

A blend containing 10 wt % PS-*b*-PCL was photocured at room temperature (i.e. below the melting temperature of the PCL block, which is 53ºC; see Figure 9) by free radical polymerization. The monomer was activated for visible light polymerization by the addition of CQ (2 wt %) and EDMAB (2 wt %). A vitrification conversion of 0.88 was reached after four days of irradiation. As in the case of thermal curing, PCL was initially miscible with St monomer and phase-separated during photopolymerization at room temperature at a conversion degree between 0.1 and 0.2. Figure 11(a) shows a TEM image of the sample with 10 wt% PS-*b*-PCL photopolymerized at room temperature. Elongated micelles with lengths ranging from 300 nm to more than 2 μm, coexisting with much shorter micelles of about 60 nm in length, were observed. It was also noted that elongated micelles tended to be parallel to each other, resulting in face-to-face stacking into lamellar arrangements. This feature evidenced the planar nature of these structures, which can be described as ribbon-like micelles. Further information on these nanostructures was obtained by analyzing the SAXS profile recorded on the cured material (Figure 11(b)). The magnitude of the slope in the low-*q* region (Guinier regime) was equal to -2.2., which indicated the presence of planar nano-objects (Nakano *et al*. 1999). The scattering profile displayed a main maximum of spatial correlation at $q^* = 0.14$ nm^{-1}, and a secondary maximum located at $2q^*$. Such a sequence corresponds to a lamellar arrangement featuring an average distance between nano-objects of 44.9 nm ($2\pi/q^*$), which was in accordance with the lamellar period estimated from the TEM image.
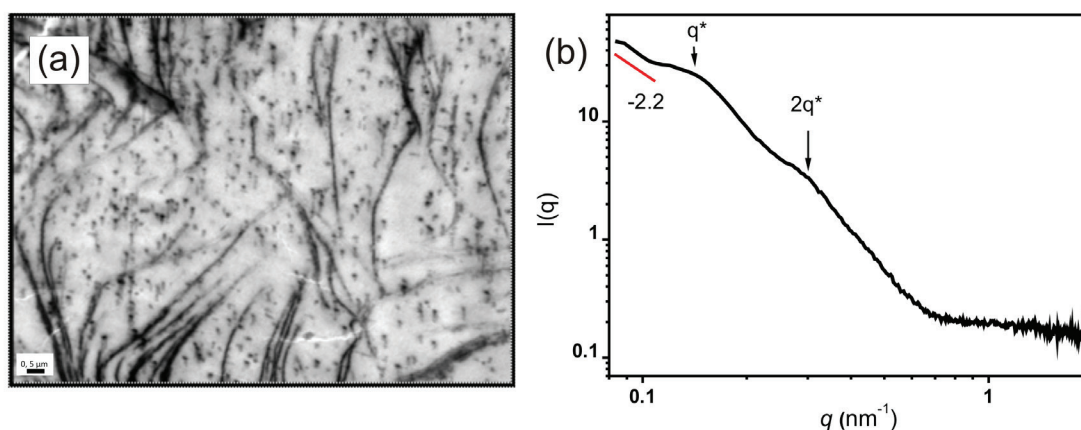
Figure 11. (a) TEM image of the blend with 10 wt % PS-*b*-PCL photocured at room temperature. The specimen was stained with RuO$_4$ prior to TEM observation. Scale bar 0.5 μm. **(b)** SAXS profile of the blend with 10 wt % PS-*b*-PCL photocured at room temperature. Reprinted from *Eur. Polym. J.*, *112*, Montoya Rojo, Ú. M.; Riccardi, C. C.; Ninago, M. D.; Ciolino, A. E.; Villar, M. A.; Ceolín, M.; Zucchi, I. A.; Schroeder, W. F., Photopolymerization-Assisted Self-Assembly as a Strategy to Obtain a Dispersion of Very High Aspect Ratio Nanostructures in a Polystyrene Matrix, 704–713, Copyright (2019), with permission from Elsevier.

To investigate the nanostructuration process of PS-*b*-PCL during the photopolymerization of St, *in-situ* SAXS and XRD experiments were performed. The results showed that, during the first 41 hours of irradiation, no events occurred except for the demixing of PCL blocks, which took place at 15 minutes of reaction. PCL cores crystallization occurred after 41 hours of irradiation. This process was evidenced as a marked raise in the intensity of SAXS profiles caused by the increase in phase contrast when one of phases crystallizes. It should be clarified that the T$_g$ of the matrix corresponding to 41 hours of irradiation was approximately 0 ºC (as determined by DSC, data not shown), which is below the crystallization temperature of PCL (27 ºC). Under these conditions, the temperature gap ($T_{c,PCL}$ - $T_{g,matrix}$) at the beginning of the crystallization process was 27ºC. This temperature window was sufficient for the CDSA mechanism to cause micelle elongation. This micellar elongation process took place during the time elapsed between matrix crystallization and vitrification. Note that if the polymerization kinetics had not been slow enough, matrix vitrification could have occurred before micellar crystallization, resulting in amorphous rod-like micelles frozen in the PS matrix, similar to the sample polymerized at 90 °C. Consequently, it was stated that under *slow* photopolymerization at room temperature, a blend consisting of 10 wt% PS-*b*-PCL dissolved in St monomer led to a population of long crystalline nanoribbons dispersed in a PS matrix.

3. PEB-*b*-PEO self-assembly in an epoxy matrix

Lastly, to explore the effect of suppressing immiscible block crystallization, poly(ethylene-co-butene)-*block*-poly(ethylene oxide) (PEB-*b*-PEO, M_n = 2700, PDI = 1.09, 45 wt% PEB) was chosen as block copolymer and DGEBA as the reactive monomer. In this case, PEB block is completely immiscible with DGEBA, while PEO is miscible before and after the curing reaction. Consequently, nanostructures were obtained from the initial blend through the *self-assembly* mechanism. Samples were prepared at two different temperatures of polymerization, 80°C and room temperature (20°C).
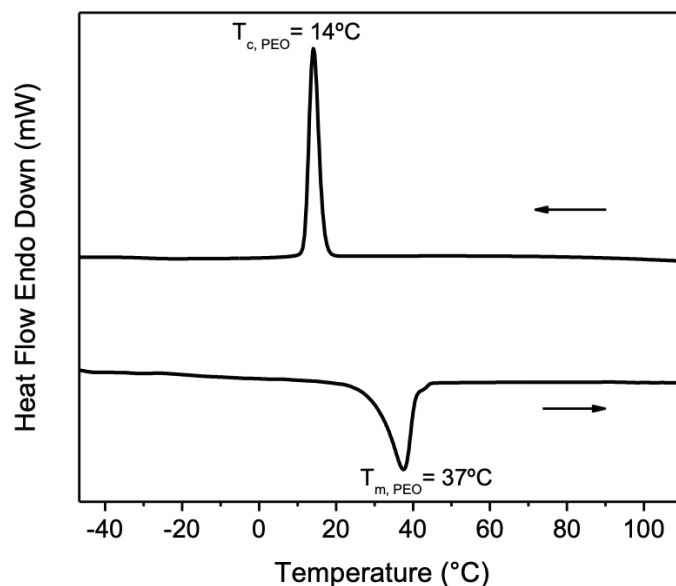
Figure 12. DSC scans at 10 ºC/min of the cooling (above) and subsequent heating (below) for the pure PEB-*b*-PEO block copolymer.

The DSC analysis of the neat PEB-*b*-PEO allowed to corroborate the absence of crystallinity of the immiscible block (PEB). As it can be seen in Figure 12, only one thermal transition was observed during cooling and heating scans, assigned to crystallization and melting of PEO crystals, respectively. The location of such transitions was in agreement with the molecular weight of PEO blocks (Leonardi *et al.* 2015). The DSC analysis confirmed that the PEB block was amorphous, and its glass transition temperature was located below the temperature range explored.

3.1. Curing at 80 ºC

First, the case in which a 10 wt% of PEB-*b*-PEO/DGEBA blend was thermally cured at 80°C is discussed. Here, BDMA was used as thermal initiator for epoxy homopolymerization. Under these conditions, the reaction was completed after 3 hours (Puig *et al.* 2017). Figure 13(a) shows a TEM image of the material obtained after curing. A dispersion of spherical micelles partially arranged in micellar columns and some cylindrical micelles were observed. In order to get information about the evolution of such nanostructures along polymerization, *in situ* SAXS spectra were acquired during polymerization at 80 °C (Figure 13 (b)). No significant change in spectra was found throughout the reaction, except for a small shift of the position of the main peak towards lower *q* values. These results indicated that the resulting morphology corresponded to that present in the initial blend (before curing) but with an increased distance between nano-objects. As Figure 13(b) shows, all SAXS diagrams presented a slope of −4 in the high-*q* region (Porod regime). This indicated that the dispersing objects had a smooth surface (Glatter and Kratky, 1982). The analysis showed that the spherical and cylindrical micelles were present in the initial blend, and were then frozen by the polymerization reaction.
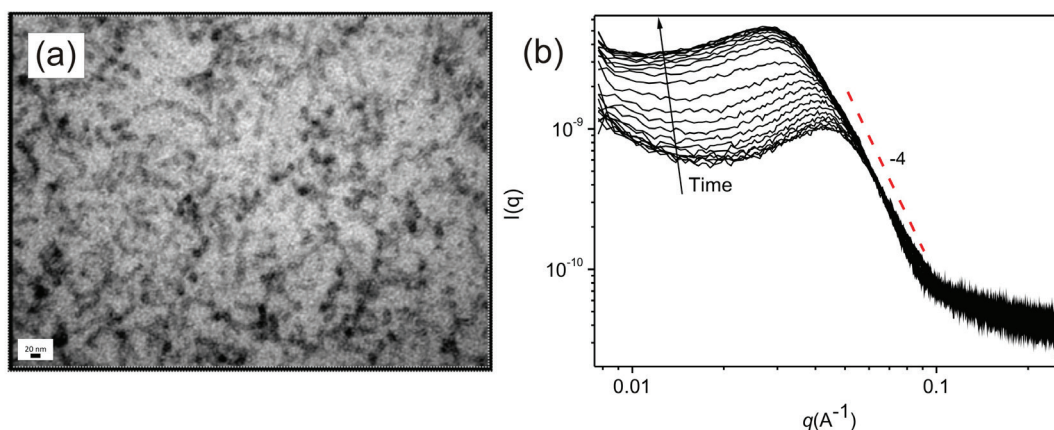
Figure 13. (a) TEM image of the epoxy blend with 10 wt % PEB-*b*-PEO fully cured at 80ºC. The specimen was stained with RuO_4 prior to TEM observation. Scale bar 20 nm. **(b)** *In situ* SAXS data obtained during curing at 80ºC of the epoxy blend with 10 wt % PEB-*b*-PEO. [Puig, J.; Ceolín, M.; Williams, R. J. J.; Schroeder, W. F.; Zucchi, I. A. *Soft Matter* **2017**, *13* (40), 7341–7351] Reproduced by permission of The Royal Society of Chemistry.

3.2. Photocuring at room temperature

The blend containing 10 wt% PEB-*b*-PEO was also cured at room temperature by visible-light cationic photopolymerization. The mixture was activated for visible light irradiation by the addition of a photoinitiating system based on two components: Ph_2ISbF_6 (2 wt%) and CQ (1 wt%). Under these conditions, a vitrification conversion of 0.62 was reached after 4 hours of irradiation. The morphology of the resulting thermoset was characterized by transmission electron microscopy (TEM) and small-angle X-ray scattering (SAXS). Figure 14 (a) shows a TEM micrograph of the photo-cured sample stained with RuO_4. Bilayer vesicles encapsulating the matrix can be observed, where the PEO corona is seen as darker lines surrounding the PEB core (lighter line). Mean vesicle diameter was 78.6 ± 27.7 nm, as determined from the analysis of several images.

To investigate whether the resulting vesicles were already present in the initial blend or formed during the reaction, *in situ* SAXS measurements were performed. Figure 14(b) shows the SAXS curves as a function of irradiation time. Contrary to the results obtained when curing was performed at 80ºC, in this case a continuous change in the SAXS pattern with reaction time was observed, indicating that the vesicular structure was the result of a polymerization-induced morphological transition. Information about the evolution of the micellar structure as a function of irradiation time was obtained from the slope of the low-*q* region (Guinier regime) of the scattering profiles. At the beginning (t=0 min), the scattering profile showed a maximum at q_{max} = 0.44 nm^{-1} indicating that the reactive blend was initially phase separated. This is in agreement with a nanostructured blend obtained through the *self-assembly* mechanism. As reaction progressed, the maximum reduced and finally disappeared at 75 min of reaction. At that time the low-q slope became equal to 0, then it decreased to -1 close to 105 min, and finally to -2 near 145 min. According to theory, a low-q slope of 0 in the Guinier regime can be assigned to spheres, a slope of -1 to rigid rods and a slope of -2 to planar structures (like vesicles) (Glatter and Kratky, 1982). The results obtained from the Guinier analysis are in agreement with the commonly observed sequence of morphologies (*i.e.*, sphere-to-cylinder-to-vesicle) derived from the increase in the segregation strength between the BCP and the epoxy matrix as polymerization progresses. SAXS data were analyzed using the SASfit software package in the *q*-region from 0.1 to 0.7 nm^{-1}. The analysis showed that during the first 100 min of reaction, the system tended to reduce the total interfacial area by increasing micellar size while reducing the total number of micelles. As the reaction progressed, the spherical micelles converted into cylindrical micelles of smaller diameter, thus reducing system's total free energy. As polymerization progressed further, an analogous tendency to reduce the total free energy of the system forces a cylinder-to-vesicle transformation. The morphological transition (Sphere-Cylinder-Vesicle) was triggered by the change in the quality of the epoxy solvent during polymerization. The epoxy monomer, which acts as a selective solvent for the PEO block, produced a swollen "wet" PEO brush at the beginning of the reaction. During polymerization, the continuous increase in the size of epoxy oligomers decreased the miscibility of PEO through a reduction in the entropic contribution to the free energy of mixing. Under this circumstance, the polymerizing epoxy expelled the PEO brushes, creating conformational strains that induced a reduction of the local interfacial curvature. This is known as *wet to dry* brush transformation (Lipic *et al.* 1998). The appearance of vesicles was the response of the system to the conformational strain caused by the polymerization.
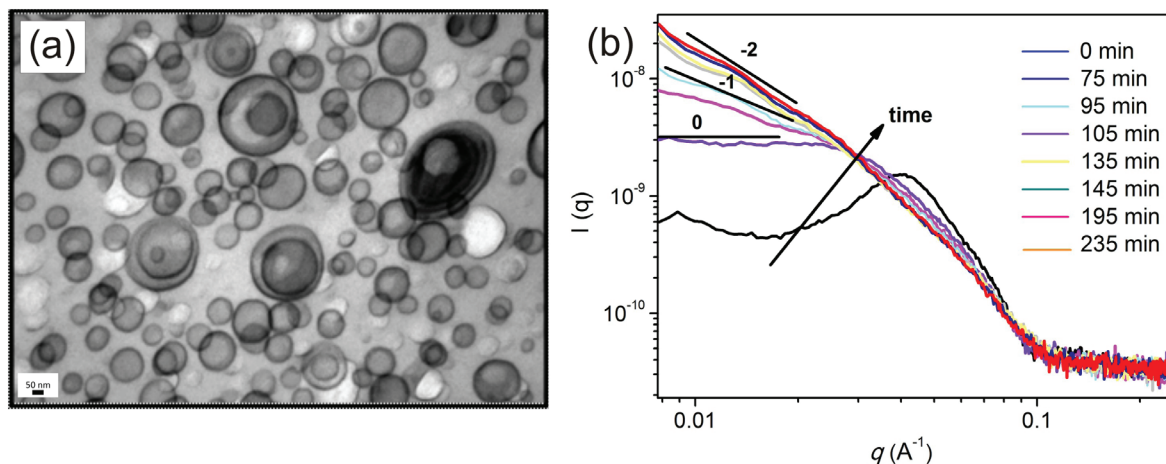
Figure 14. (a) TEM image of the epoxy blend with 10 wt % PEB-*b*-PEO photocured at room temperature. The specimen was stained with RuO$_4$ prior to TEM observation. Scale bar 50 nm. **(b)** *In situ* SAXS data obtained during photo-polymerization at room temperature of the epoxy blend with 10 wt % PEB-*b*-PEO. [Puig, J.; Ceolín, M.; Williams, R. J. J.; Schroeder, W. F.; Zucchi, I. A. *Soft Matter* **2017**, *13* (40), 7341–7351] Reproduced by permission of The Royal Society of Chemistry.

A question arises: why was the nanostructure obtained by curing at 80ºC so different from that obtained at room temperature? The difference between the resulting morphologies (spheres vs. vesicles) was explained by comparing reaction kinetics. Figure 15 shows conversion vs. time curves for thermal cure at 80 ºC and photocuring at room temperature. As it can be seen, both curves were identical until a conversion value of approximately 0.1. After this conversion, reaction rate at 80 ºC was markedly accelerated with respect to that at room temperature. It is evident that, under conditions of slow photopolymerization, the system could evolve from spheres to vesicles due to the high mobility of the matrix when transitions were triggered. On the contrary, when the cure was carried out at 80 ºC, the initial spherical structures were kinetically trapped by diffusion constraints imposed by the fast polymerization of the matrix and the system could not evolve.

Once again, the critical role played by matrix mobility at the moment in which nanostructures evolved was evidenced. In this case, mobility could not be measured as a temperature gap between crystallization and T$_g$, since no crystallization of the immiscible block occurred. However, it was measured in terms of the diffusional constraints imposed by the conversion degree of the matrix at the moment of the morphological transition.
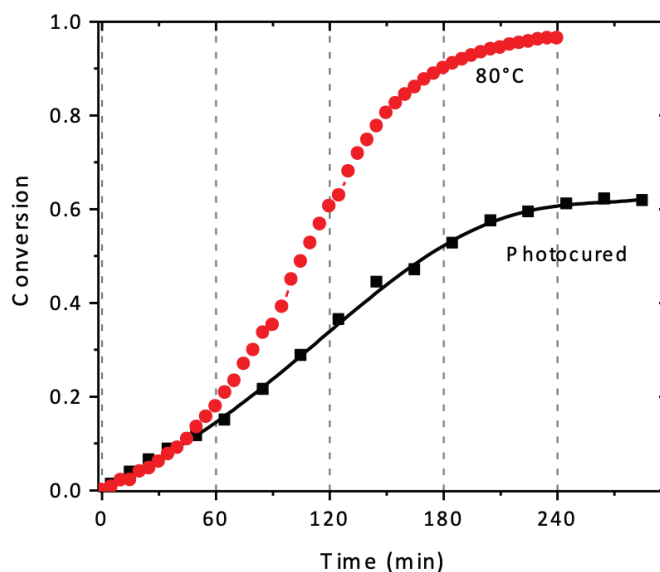

Figure 15. Conversion vs. time curves for the epoxy blend with 10 wt% PEB-*b*-PEO, during thermal polymerization at 80 °C (circles) and photocuring at room temperature (squares). [Puig, J.; Ceolín, M.; Williams, R. J. J.; Schroeder, W. F.; Zucchi, I. A. *Soft Matter* **2017**, *13* (40), 7341–7351] Reproduced by permission of The Royal Society of Chemistry.

Conclusions

This review described different approaches reported to obtain novel block copolymer nanostructures dispersed in polymer matrices. It was demonstrated that the glass transition temperature (T_g) of the matrix at the moment of the morphological transformation plays a decisive role determining the architecture of the nanostructure obtained.

Planar structures with precisely controlled length (ribbon-like micelles) can be obtained through a crystallization-driven self-assembly mechanism. In this case, micellar length can be tailored by regulating the temperature gap between the crystallization and the T_g of the matrix. By this approach, structures ranging from discotic micelles to nanoribbons of very high aspect ratio can be obtained. In contrast, when crystallization is suppressed by matrix vitrification, amorphous rod-like micelles are obtained. On the other hand, when the core-forming block is an amorphous polymer, vesicles dispersed in an epoxy matrix can be generated through sphere-to-cylinder-to-vesicle morphological transition under slow photopolymerization conditions. It was demonstrated that matrix mobility, once again, plays a crucial role in allowing such transitions.

Acknowledgments

References

[1] J. Bang, U. Jeong, D.Y Ryu, T.P. Russell, and C.J. Hawker. Block Copolymer Nanolithography: Translation of Molecular Level Control to Nanoscale Patterns. *Adv. Mater.*, 21: 4769–4792, 2009.

[2] C.E. Boott, E.M. Leitao, D.W Hayward, R.F. Laine, P. Mahou, G. Guerin, M.A. Winnik, R.M. Richardson,C.F. Kaminski,G.R. Whittell, G.R., et al.. Probing the Growth Kinetics for the Formation of Uniform 1D Block Copolymer Nanoparticles by Living Crystallization-Driven Self-Assembly. *ACS Nano*, 12: 8920–8933, 2018.

[3] L. Cao, I. Manners, and M.A. Winnik. Influence of the Interplay of Crystallization and Chain Stretching on Micellar Morphologies: Solution Self-Assembly of Coil−Crystalline Poly(isoprene-block-ferrocenylsilane). *Macromolecules*, 35: 8258–8260, 2002.

[4] J.J. Crassous, P. Schurtenberger, M. Ballauff, and A.M. Mihut. Design of block copolymer micelles via crystallization. *Polymer* 62: A1–A13, 2015.

[5] O.Glatter and O. Kratky. Small Angle X-ray Scattering, Academic Press, London, 1982.

[6] G. Guerin, G. Cambridge, M. Soleimani, S. Mastour Tehrani, I. Manners, and M.A. Winnik. Form Factor of Asymmetric Elongated Micelles: Playing with Russian Dolls Has Never Been so Informative. *J. Phys. Chem. B*, 118: 10740–10749, 2014.

[7] G. Guerin, P.A. Rupar, I. Manners and M.A. Winnik. Explosive dissolution and trapping of block copolymer seed crystallites. *Nat. Commun.*, 9: 1158, 2018.

[8] Q. Guo, J.M. Dean, R.B. Grubbs, and F.S. Bates. Block copolymer modified novolac epoxy resin. *J. Polym. Sci. Part B Polym. Phys.*, 41: 1994–2003, 2003a.

[9] Q. Guo, R. Thomann, W. Gronski, R. Staneva, R. Ivanova, and B. Stühn. Nanostructures, Semicrytalline Morphology, and Nanoscale Confinement Effect on the Crystallization Kinetics in Self-Organized Block Copolymer/Thermoset Blends. *Macromolecules,* 36: 3635–3645, 2003b.

[10] R.C. Hayward and D.J. Pochan. Tailored Assemblies of Block Copolymers in Solution: It Is All about the Process. *Macromolecules*, 43: 3577–3584, 2010.

[11] W.-N. He and J-T. Xu. Crystallization assisted self-assembly of semicrystalline block copolymers. *Prog. Polym. Sci.*, 37: 1350–1400, 2012a.

[12] W.-N. He, B. Zhou, J.-T. Xu, B-Y. Du and Z.-Q. Fan. Two Growth Modes of Semicrystalline Cylindrical Poly(ε-caprolactone)-b-poly(ethylene oxide) Micelles. *Macromolecules*, 45: 9768–9778, 2012b.

[13] A.B. Leonardi, I.A. Zucchi and R.J.J. Williams. Generation of large and locally aligned wormlike micelles in block copolymer/epoxy blends. *Eur. Polym. J.*, 65: 202–208, 2015.

[14] P.M Lipic, F.S. Bates and M.A. Hillmyer. Nanostructured Thermosets from Self-Assembled Amphiphilic Block Copolymer/Epoxy Resin Mixtures. *J. Am. Chem. Soc.* ,120: 8963–8970, 1998.

[15] Y. Mai and A. Eisenberg. Self-assembly of block copolymers. *Chem. Soc. Rev.* ,41 :5969–5985, 2012.

[16] F. Meng, S. Zheng, H. Li, Q. Liang and T. Liu. Formation of Ordered Nanostructures in Epoxy Thermosets: A Mechanism of Reaction-Induced Microphase Separation. *Macromolecules*, 39: 5072–5080, 2006a.

[17] F. Meng, S. Zheng and T. Liu. Epoxy resin containing poly(ethylene oxide)-block-poly(ε-caprolactone) diblock copolymer: Effect of curing agents on nanostructures. *Polymer*, 47: 7590–7600, 2006b.

[18] R.M. Michell and A. J. Müller. Confined crystallization of polymeric materials. *Prog. Polym. Sci.*, 54–55: 183–213, 2016.

[19] A.M. Mihut, M. Drechsler, M. Möller and M. Ballauff. Sphere-to-Rod Transition of Micelles formed by the Semicrystalline Polybutadiene-block-Poly(ethylene oxide) Block Copolymer in a Selective Solvent. *Macromol. Rapid Commun.*, 31: 449–453, 2010.

[20] Ú.M. Montoya Rojo, C.C. Riccardi, M.D. Ninago, A.E. Ciolino, M.A. Villar, M. Ceolín, I.A. Zucchi and W.F. Schroeder. Photopolymerization-assisted self-assembly as a strategy to obtain a dispersion of very high aspect ratio nanostructures in a polystyrene matrix. *Eur. Polym. J.*, 112: 704–713, 2019.

[21] M. Nakano, K. Matsumoto, H. Matsuoka and H. Yamaoka. Characterization of Micellization Behavior of Amphiphilic Polymer Having Octadecyl Group by Small-Angle X-ray and Neutron Scattering. *Macromolecules*, 32: 4023–4029, 1999.

[22] A.N. Parikh, S.D. Gillmor, J.D. Beers, K.M. Beardmore, R.W. Cutts and B.I. Swanson. Characterization of Chain Molecular Assemblies in Long-Chain, Layered Silver Thiolates: A Joint Infrared Spectroscopy and X-ray Diffraction Study. *J. Phys. Chem. B* , 103: 2850–2861, 1999.

[23] J. Puig, I.A. Zucchi, M. Ceolín, W.F. Schroeder and R.J.J. Williams. Evolution of morphologies of a PE-b-PEO block copolymer in an epoxy solvent induced by polymerization followed by crystallization-driven self-assembly of PE blocks during cooling. *RSC Adv.*, 6: 34903–34912, 2016.

[24] J. Puig, M. Ceolín, R.J.J Williams, W.F. Schroeder and I.A. Zucchi. Controlling the generation of bilayer and multilayer vesicles in block copolymer/epoxy blends by a slow photopolymerization process. *Soft Matter*, 13: 7341–7351, 2017.

[25] D. Richter, D. Schneiders, M. Monkenbusch, L. Willner, L.F. Fetters, J.S. Huang, M. Lin, K. Mortensen and B. Farago. Polymer Aggregates with Crystalline Cores: The System Polyethylene−Poly(ethylenepropylene). *Macromolecules*, 30: 1053–1068, 1997.

[26] R.N. Schmarsow, M. Ceolín, I.A. Zucchi and W.F. Schroeder. Core-crystalline nanoribbons of controlled length via diffusion-limited colloid aggregation. *Soft Matter*, 15:4751-4760, 2019.

[27] L. Shen, H. Wang, G. Guerin, C. Wu, I. Manners and M.A. Winnik. A Micellar Sphere-to-Cylinder Transition of Poly(ferrocenyldimethylsilane-b-2-vinylpyridine) in a Selective Solvent Driven by Crystallization. *Macromolecules*, 41: 4380–4389, 2008.

[28] C. Sinturel, M. Vayer, R. Erre and H. Amenitsch. Nanostructured polymers obtained from polyethylene-block-poly(ethylene oxide) block copolymer in unsaturated polyester. *Macromolecules*, 40: 2532–2538, 2007.

[29] C. Sinturel, M. Vayer, R. Erre and H. Amenitsch. Thermal induced mobility of self-assembled platelets of polyethylene-block-poly(ethylene oxide) in liquid precursors of unsaturated polyester thermoset. *Eur. Polym. J.*, 45: 2505–2512, 2009.

[30] A. Tercjak, M. Larrañaga, M.D. Martin and I. Mondragon. Thermallyreversible nanostructured thermosetting blends modified with poly(ethylene-b-ethyleneoxide) diblock copolymer. *J. Therm. Anal. Calorim.*, 86: 663–667, 2006.

[31] S.Tiptipakorn, N. Keungputpong, S. Phothiphiphit and S. Rimdusit. Effects of polycaprolactone molecular weights on thermal and mechanical properties of polybenzoxazine. *J. Appl. Polym. Sci.* 132 (11pp), 2015.

[32] Trent, J.S., Scheinbeim, J.I., and Couchman, P.R. (1983). Ruthenium tetraoxide staining of polymers for electron microscopy. *Macromolecules*, 16:589–598, 1983.

[33] Wang, X., Guerin, G., Wang, H., Wang, Y., Manners, I., and Winnik, M.A. Cylindrical Block Copolymer Micelles and Co-Micelles of Controlled Length and Architecture. *Science*, 317 :644–647, 2007.

[34] J. Wu, Y.S. Thio and F.S. Bates. Structure and properties of PBO–PEO diblock copolymer modified epoxy. *J. Polym. Sci. Part B Polym. Phys.*, 43: 1950–1965, 2005.

[35] L.Yin, T.P. Lodge and M.A. Hillmyer. A Stepwise "Micellization–Crystallization" Route to Oblate Ellipsoidal, Cylindrical, and Bilayer Micelles with Polyethylene Cores in Water. *Macromolecules*, 45: 9460–9467, 2012.

[36] C.Zhang, L. Li and S. Zheng. Formation and Confined Crystallization of Polyethylene Nanophases in Epoxy Thermosets. *Macromolecules*, 46, 2740–2753, 2013.

[37] I.A. Zucchi and W.F. Schroeder. Nanoribbons with semicrystalline core dispersed in a visible-light photopolymerized epoxy network. *Polymer*, 56, 300–308, 2015.

Bios

Jessica Gutiérrez González

Jessica Gutiérrez González received her B.Sc. degree in Chemistry from University of Quindío, Colombia. From 2013 to 2016, she participated in biological sciences projects at the National University of La Plata (UNMdP, Argentina). She is currently a Ph. D student in Material Sciences at the UNMdP. Her main research interests include the study and characterization of nanostructured materials obtained by the self-assembly of semi-crystalline block copolymers.

Ruth N. Schmarsow

Ruth N. Schmarsow received her B.Sc. degree in Chemistry from the National University of Mar del Plata (UNMdP , Argentina) in 2017. She is a teaching associate at the Department of Chemistry of the UNMdP. She is currently a Ph.D student in Material Sciences at the School of Engineering of the UNMdP. Her main research interest is the synthesis and characterization of functional materials obtained by semi-crystalline block copolymer self-assembly in different polymer matrices.

Úrsula Montoya Rojo

Úrsula Montoya Rojo is an assistant professor at the School of Engineering of the University of Buenos Aires (UBA, Argentina). She has a degree on Agroindustrial Engineering from University Pontificia Bolivariana (Colombia). She received her PhD in Materials Science from the National University of Mar del Plata (UNMdP, Argentina) in 2017. She is currently a postdoctoral fellow at the Biotechnology and Biosynthesis Group (ITPN-UBA-CONICET, Argentina). She has been active in the field of nanostructures of biopolymers based on vegetable and bacterial cellulose nanofibers as well as on self-assembly as a strategy to obtain nanostructures in different polymeric networks.

Julieta Puig

Julieta Puig obtained her B.Sc. in Chemistry (2009) and PhD in Materials Science (2014) from the National University of Mar del Plata (UNMdP, Argentina). Her PhD focused on different tailor-made polymeric matrices and their modification using several types of hydrophobic modifiers for the development of functional materials with technological properties. For her postdoc, she worked in the generation of novel nanostructures of block copolymers in an epoxy monomer via photo- and thermal polymerization. She is currently working as an Assistant Researcher at INTEMA-CONICET. Her main research interest is the preparation of functional nanostructured materials with special optical and thermal properties for the development of Smart Windows.

Walter F. Schroeder

Walter F. Schroeder obtained his B.Sc and Ph.D. degrees at University of Mar del Plata (UNMdP, Argentina). He was a postdoctoral fellow in the Department of Chemistry at the University of Toronto (Canada), where he studied polymer diffusion by Fluorescence Resonance Energy Transfer (FRET). He is currently a scientific researcher for CONICET and a professor at the Department of Chemical Engineering of the UNMdP. His main research interest is the study of the kinetic and thermodynamic aspects involved in the formation of nano-structured materials obtained by self-assembly of block copolymers in polymer matrices.

Ileana A. Zucchi

Ileana A. Zucchi obtained her B.Sc. and Ph.D. degrees from the National University of Mar del Plata (UNMdP, Argentina). She was a postdoctoral fellow at the Institute for Microelectronics and Microsystems of the National Research Council of Italy, studying the generation of block copolymer templates for advanced nanolithography applications. Since 2008, she is a researcher scientist for CONICET and teaching assistant at the Department of Chemical Engineering of the UNMdP. Her research focuses on the development of functional materials through the self-assembly of block copolymers.

Emerging Experimental Strategies for Studies on Inhomogeneous Nanomaterials. Exploring Electronics, Atomic Structure and Properties by Synchrotron X-Ray-Based Techniques

Félix G. Requejo

Instituto de Investigaciones Fisicoquímicas Teóricas y Aplicadas (INIFTA), CONICET y FCE, UNLP, La Plata, Argentina.
E-mail: requejo@inifta.unlp.edu.ar

Abstract

Through representative examples, we illustrate the strategic value of synchrotron X-ray-based techniques for nanomaterial characterization, especially for inhomogeneous nanomaterials. These examples are used to describe opportunities, motivations for new questions and possible reexamination of older topics, not only due to the proven success of the scientific instrumentation, but also because the extraordinary specific advantages offered by the new X-ray micro and nanoprobes techniques.

Keywords:

synchrotron radiation, microprobes and nanoprobes, nanomaterials, nanoparticles
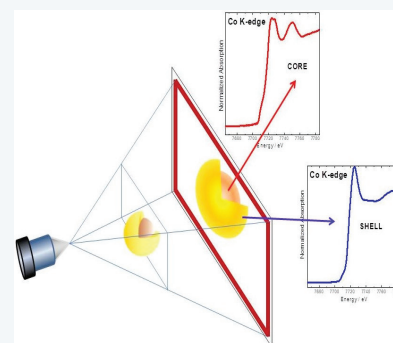
Focus of the review

This present review is aimed at describing recent improvements for nanomaterial characterizations strategies using a meaningful set of scientific cases related to the demanding understanding of inhomogeneous nanomaterials structure and electronics. We present a set of emerging techniques based on X-ray interaction with matter, paying special attention to X-ray micro and nanoprobes tools, discussing their impact in the nanoscience research field.
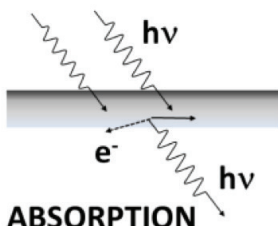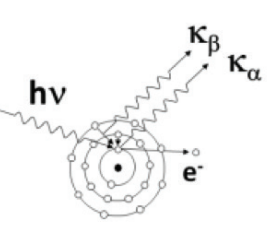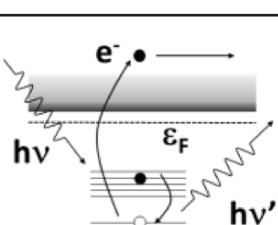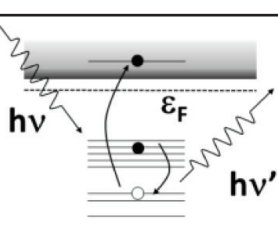
Introduction

Nanomaterial characterizations and synchrotron radiation-based studies

The demand for advanced characterization in nanomaterials is a neck of the bottle for the increasing challenge in the rational design of new nanomaterials and nanocomposites. Typical limitations are, in general, associated with chemical speciation at different regions of nanomaterials (distinguishing surface from volume contributions), *in situ* determinations controlling the environment at very low time-scales, and/or sensitivity for the detection of small concentrations of the species (atomic clusters or individual atoms). Undoubtedly, no single experimental approach can be enough to elucidate any relevant question about atomic and electronic structure, responsible for chemical, mechanical, magnetic or any other physical properties. Different "cocktails" of experimental strategies became mandatory for that purpose, where new and fascinating instrumental developments are being successfully applied. At this point, the synchrotron-based techniques emerge as one of the more relevant solutions to attend the growing demand for advanced nanomaterial characterizations.
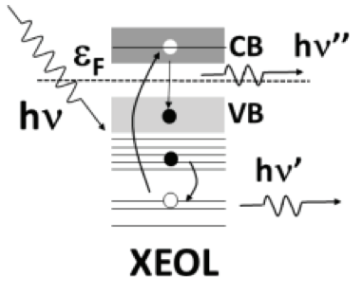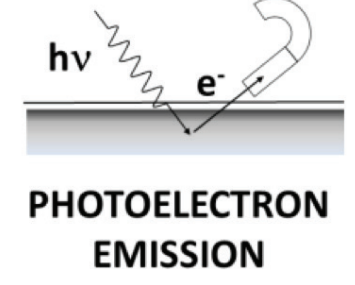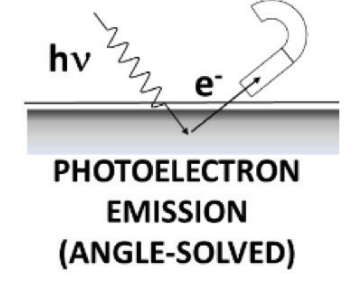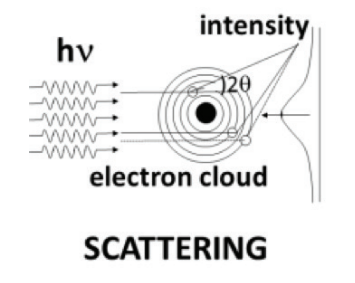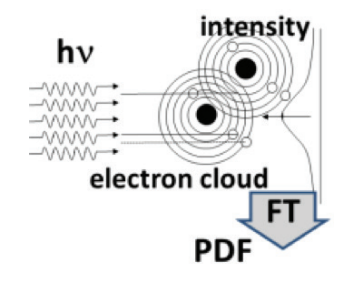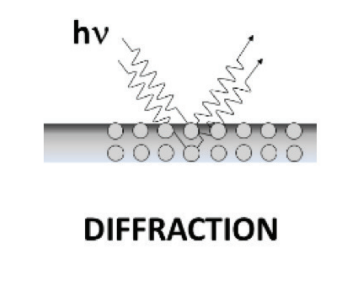
In particular, the progress of synchrotron sources for X-rays not only evolves in higher brilliance, but also in emittance and coherence, in addition to drastic improvements for insertion devices and scientific instrumentation at end-stations (like detectors or electronics and new architecture for data acquisition). From the beginning, synchrotron facilities for scientific research constitute an attractive opportunity to look for new solutions, and to turn on the imagination for new experimental challenges, pushing beyond the limit of the scientifically known.

Many aspects in nanomaterials can be analyzed taking into account different physical process associated with the interaction of X-rays with matter. X-ray scattering is useful for studying the shape and size of nanomaterials; X-ray absorption is used to determine the electronic structure of empty levels and the local atomic environment of the absorbing atoms; the emission of the excited atoms is associated with the density of occupied electronic levels; selective absorption – considering the spin state – is employed for magnetism studies; and electronic photoemission is very sensible for surface and interphases probing. All these physical processes are being taken into account for the increasing development of advanced instrumentation and techniques (Table 1). An outstanding example for recent advances in instrumentation is the *in situ* or *operando* detection modes, in particular to bridge the pressure gap in the XPS technique, represented by the already well-established NAP-XPS technique (Salmeron *et al.*, 2018). Additional developments are being achieved, more recently, devoted to improve time and spatial resolution, which are necessarily associated with 4th generation synchrotron machines (Kwiatek *et al.*, 2019). This review deals precisely with the most recent and emerging improvements, associated with micro and nano-focus progresses.

Table 1. Different X-ray-based synchrotron techniques, their associated physical processes, and their applications for material characterizations.

Process	Technique	Information provided
ABSORPTION	- X-ray absorption near-edge spectroscopy -Extended X-ray absorption fine structure (EXAFS)	XANES is strongly sensitive to formal oxidation state and the coordination chemistry of the absorbing atom, while EXAFS is used to determine the distances, coordination number, and species of the neighbors of the absorbing atom
FLUORESCENCE	- X-ray fluorescence (XRF)	It can be used for the qualitative and quantitative determination of the elemental composition of a material sample, as well as for measuring coatings and coating systems.
EMISSION	- X-ray emission spectroscopy (XES)	It is used to elucidate electronic structures, providing information about electron energies, local geometry, spin, and valence state.
RESONANT EMISSION	- Resonant Inelastic X-ray Scattering (RIXS)	It probes valence electrons behavior, both local and collective. It probes both occupied and unoccupied states.

XEOL	- X-ray Excited Optical Luminescence (XEOL) - Time-Resolved XEOL (TRXEOL)	It allows extracting information about the real amount of luminescent sites, or their location in the sample.
PHOTOELECTRON EMISSION	- X-ray photoelectron spectroscopy (XPS) - Near Ambient Pressure XPS (NAP-XPS)	It allows quantitative measurements of the elemental composition, atomic concentrations and chemical states of elements present on the surface of a sample. The NAP version can probe chemical interactions on the atomic level for vapor/solid interfaces.
PHOTOELECTRON EMISSION (ANGLE-SOLVED)	Angle-Resolved Photoemission Spectroscopy (ARPES)	It has the unique capability to directly resolve in energy-momentum space and hence image electronic structures of materials.
SCATTERING	- Small-angle X-ray scattering (SAXS)	It quantitatively measures electronic density differences in a sample. Thus, it can determine nanoparticle size distributions, the size and shape of macromolecules, pore sizes, characteristic distances of partially ordered materials.
PDF	Pair Distribution Function (PDF)	It can be used to study the local structure of materials at the atomic scale.
DIFFRACTION	- X-ray diffraction (XRD)	It provides information about structures, phases, preferred crystal orientations (texture), and other structural parameters, such as average grain size, crystallinity, strain, and crystal defects.

Inhomogeneous nanostructures: interest and characterization

Among the numerous types of inhomogeneous nanomaterials, core@shell-type (CS) nanostructures are worthy of attention. Those sort of nanoparticles (NPs) present challenges not only because of their synthesis complexity, but also because of their novelty for properties associated with their heterogeneity in composition and/or structure. SC structures can be considered as the simplest possible model to describe inhomogeneity at the nanoscale. Thus, all the efforts in CS characterization represent a progress for understanding more complex structures.

CS NPs are a class of preferred inhomogeneous nanomaterials due to their interesting properties and broad range of applications in catalysis (Guo *et al.*, 2013), biology (Hoskins *et al.*, 2012), materials chemistry (Acebrón *et al.*, 2017), magnetism (Wu L. *et al.*, 2016), energy (Cui *et al.*, 2013) and sensors (Vera *et al.*, 2017). By rationally tuning the cores, as well as the shells, a range of CS NPs can be produced with tailorable properties to play important roles in different physicochemical processes, offering solutions for present technological demands. In general, the definition of the CS NPs can be extended to nanomaterials having different boundary covering (either fully or partially) the inner component, as long as they can be separately identified. At times, they cannot be simply described as a single material surrounded by a homogeneous, different one. In reality, it is possible to find, through few nanometers, a *dégradé* of compositions and mixtures of chemical elements, structures and species, not easily ascribed to bulk version because of the short periodicity of the atomic arrangements. That peculiar atomic arrangement, finally defines the desired properties for the CS NPs. Thus, the detailed characterization becomes crucial to understand the origin of their properties.

An overview of the available techniques for characterizing CS nanostructures typically includes X-ray diffraction (XRD), scanning electron microscopy (SEM) and transmission electron microscopy (TEM) (Manoj *et al.*, 2015). Even though all these techniques are usually used to determine the size, morphology and homogeneity of the NPs, the first one requires the crystallinity of the phases, while the last two can detect both phases simultaneously. Additionally, SEM usually involves collecting secondary electrons and therefore generates only a surface image, and it is difficult to distinguish the core from the shell. High resolution TEM (HRTEM) enables the simultaneous observation, but not trivial, of lattice borders with different spacing in the core and shell from a single particle. The energy dispersive spectrometry (EDS), as a TEM accessory, provides one of the most powerful methods for determining the chemical distribution of elements with high spatial resolution, including the limitation of the adequate environment for electron detection. Complementary techniques, with high spatial resolution, can be found in electron energy loss spectroscopy (EELS). A variation of those methodologies is represented by high angle annular dark-field STEM (HAADF-STEM), where elements with important contrast in atomic number are required for successful determinations. More recently, images with atomic-resolution can be obtained by aberration-corrected STEM. In another set of more common techniques, we can find different spectroscopies such as UV-Vis that can be employed in specific cases for indirect determinations, which are the most commonly used type of spectroscopy, especially capable of absorbing in the UV-Vis region of the electromagnetic radiation. Infrared spectroscopy is particularly useful for the identification of organic molecules (for organic types of CS nanostructures). Additionally, Raman spectroscopy is widely used for surface characterization, and surface enhanced Raman spectroscopy (SERS) for studying CS NPs containing SERS active metals (Au, Ag, and Cu).

Synchrotron-based techniques applied to CS NP characterization have been successfully used in recent years. The competence of X-rays to analyze the structure and dynamics of almost all forms of matter has been largely demonstrated. X-rays analysis covers range of lengths that is of interest for nanomaterial characterizations between 10^{-3} to about 100 nm, and the time resolution to explore dynamic process from about 10^{-16} to 10^3 s. Several techniques based on scattering, diffraction, spectroscopy and imaging (Table 1) are available nowadays at end-stations in different synchrotrons around the world. The improvements for the different techniques are associated with the increase in intensity, collimation and focusing of the beam, as well as in wavelength tuning. In a synchrotron, charged particles (electrons or positrons) are accelerated and injected into a storage ring, where they get energies from 500 MeV to 8 GeV depending on the size of the ring. As the charged particles are bent around the ring (by magnetic devices), energy is dissipated by electromagnetic radiation, emitted from infrared to X-rays. Essentially, X-ray interacts with most materials, and if the experiment is conducted in a nondestructive way, they can interact selectively with surfaces or penetrate deeply into samples. In addition to this selective region analysis or sensitivity, chemical selectivity is a salient characteristic, which really makes a big difference among the different experimental methodologies, especially in the field of nanoscience. Techniques based on X-ray absorption or emission processes can selectively interact with specific chemical elements just by choosing the correct incident photon energy and/or the regions in which to detect the emitted fluorescence photons. For higher photon energies than the corresponding to the UV region, the radiation produced allows studies under real or extreme conditions of temperature, pressure, and magnetic or electric fields. This is a characteristic that has been already exploited in the last decade for *in situ* or *operando* studies (Dong *et al.*, 2018). At the synchrotron sources, radiation is highly intense, highly focused, and strongly polarized. The radiation that can be obtained includes very low energies, even lower than 0.1 keV (considered "soft" X-rays up to about 2 keV), up to 100 keV (considered as "hard" X-rays from few keV). The intermediate region between 2 and 5 keV is known as the "tender" X-ray window.

X-ray Absorption spectroscopies (XAS) are a particularly privileged set of techniques, since they allow exploring both electronic and atomic structure in very atomically confined (local) regions. Based on the local scattering of the free electrons produced after the photoelectric effect, the atomic structural aspects around the absorbing atom can be explored by extended X-ray absorption fine structure technique (EXAFS). On the other hand, the electronic structure of the same absorbing element, in particular the density of unoccupied states, is greatly probed in the same process, in the closest energy region to the absorption edge, by X-ray absorption near edge structure (XANES) spectroscopy. Because of the lower energy of the photoelectrons produced in this absorption region, the final estate of the corresponding electronic transition is given by allowed unoccupied electronic states of the same atom or molecule. In contrast to XRD, XAS can also be used for liquid samples or even for gaseous phase characterization, since it does not rely on any long-range order. Thus, XAS provides a very robust methodology for the screening of the crystallization mechanism of amorphous NPs. Phase transformation can be also monitored by XAS experiments from both *ex situ* and *in situ* configurations. Additionally, being only sensitive to the local geometrical arrangement of neighboring atoms that surround the absorbing atom, it is possible to study the interaction of the capping agent with the surface of the NP. In particular, EXAFS is appropriated for the screening of the initial crystallization behavior of amorphous NPs by probing structural changes at the atomic-level. EXAFS allowed the precise demonstration of the changes of bond lengths and the stress state of their materials on the basis of a thermal expansion mismatch. The evaluation of the EXAFS data of small NPs provides a decreased coordination number, which involves more sensitivity for parameter analysis for the CS-NP. Thus, the interface effects between core and shell regions, dilatation or contraction of the lattice, Debye-Waller factor, together with an increased static and/or thermal disorder can be examined. Importantly, in contrast to other experimental techniques based on electronic detection (like conventional XPS or TEM), XAS experiments do not necessarily require operation under ultra-high vacuum. Structural information can be obtained from EXAFS measurements, even though sometimes with lower precision and difficulty in comparison with XRD, it can also be used to distinguish two phases even having similar structure and lattice constants, like in perfectly miscible metals where both phases possess an fcc structure. Considering the symmetry of the different atomic environments, XANES is a technique more sensitive to coordination and bonding environment than, for instance, XPS, since it probes the unoccupied electronic states of atoms and therefore can provide information about the crystal field (octahedral, square pyramidal or tetrahedral) occupied by cations. The complementary use of both XPS and XANES is handy for nanostructures with complex compositions and various possible valence states.

Inhomogeneous nanomaterials characterization using synchrotron X-ray-based techniques

There is a variety of literature with studies of nanomaterials properties and performance. In particular for NP, because their properties rely heavily on their size, morphology, structure and composition, all those aspects are in general analyzed in depth following a multi-technique approach (Mourdikoudis *et al.*, 2018). The literature specifically devoted to CS-NP seems to be less abundant, where the combination of the inner core and outer shell, dispersion of species and structures on the surface of the NP and interaction at the interface have crucial effects on their properties as well as optical and catalytic activity mainly.

Many advantages and characteristics of X-ray absorption techniques for CS-NP studies were previously described for already installed facilities at synchrotron laboratories (National Nanotechnology Initiative, 2005). More specifically, we will refer now to specific aspects for the direct and indirect determination of relevant parameters, which characterize the fundamental structural and electronic aspects of such nanomaterials, responsible for their physical and chemical properties. Finally, we will refer to general concepts exemplified by a selection of significant applications of x-ray microbeams and nanobeams to materials science research, in particular for emerging challenges in the nanoscience field.

The XANES and EXAFS analyses of the atomic structure and electronic properties of NP sometimes allow discovering spontaneous or unexpected CS-NPs. This is the case, for instance, when the sulfidation of small Pd NP is caused by the capping thiol molecules present not only on the surface but also in the bulk (Ramallo-López *et al.*, 2007). Since it is an average technique, EXAFS alone cannot be used to characterize the size, structure or composition of NPs, without independent data of their distributions, especially in the case of multi-component NPs. The use of different complementary techniques and/or simulations is crucial for an accurate structural characterization of CS NPs. *In situ* XRD and EXAFS were used at the same time to monitor the oxidation process of the Co cores after thermal treatment at 800 °C, either in air or under an inert atmosphere for Co@SiO$_2$ CS NP (Zhang *et al.*, 2015). The findings allowed establishing that Co was oxidized in three steps no matter if air or N$_2$ gas was employed during the annealing treatment. In another example, Leveneur *et al.* (2011) studied the nucleation and growth of Fe NPs in SiO$_2$ by TEM, XPS and XANES. It was demonstrated that, using the ion implantation method, the entities initially resulted in the formation of dilute cationic Fe^{2+} species, while at higher dissolved iron concentrations, the formation of small metallic clusters was observed, which seed the particle growth during prolonged implantation or annealing. As already mentioned, XANES is a technique sensitive to coordination and bonding environment and it probes the unoccupied electronic states. Thus, this technique provides information

about the crystal field (octahedral, square pyramidal or tetrahedral) that iron cations occupy. XANES complements the use of XPS, and it is particularly appropriate for nanostructures with complex compositions and various possible valence states for the iron.

Multicomponent NPs became an important class of materials due to their fascinating properties, electronic properties, synergistic effects, material-specific ensemble effects and ability to carry out multiple functions from the individual constituents. They are rich in capabilities and generate novel properties as a result of the interplay between their building blocks (Frenkel *et al.*, 2012). These properties are directly affected by the details of the NP design – size, composition, homogeneity, structure, shape, surface morphology, reaction-driven restructuring, including the inorganic and organic constituent's effects, since the nature of capping ligands, solvent and nonsolvent are all contributing factors (Wang *et al.*, 1997; Tao *et al.*, 2008; Krylova *et al.*, 2012). Understanding the modification of chemical composition during NP processing is also critical for the ability to design advanced, highly-performing heterostructures as multicomponent NPs. In particular, understanding the compositional uniformity and stability of CS NP is fundamental for further progress in the design of highly efficient catalysts, since the NP surface characteristics are critical for their performance (Stamenkovic *et al.*, 2006). Additionally, regardless of the important progress in the synthesis of binary metal alloy NPs, there is still no clear understanding of the correlation between "bulk" composition and surface structure.

For all these reasons, one of the main interests is the precise and atomistic characterization of the nature of complex NPs, like multicomponent NPs or CS NPs; the measurement of geometric and compositional details with sufficient spatial resolution being one of the most challenging tasks. At present, without additional assistance of X-ray micro and nano-probes (see next section), different experimental and complementary strategies are being devoted for such purposes, with the intrinsic limitations in each particular case. Thus, structural details rapidly diminish as the size of coherent scattering region decreases to a few nm in XRD, or advanced microscopy techniques (HRTEM, SEM, etc) are seriously limited to perform structural analysis out of the UHV, i.e. under controlled environmental conditions at elevated temperatures or moderate high pressure. Among available X-rays based techniques, many of them have shown indubitable contributions to these goals (Table 1). In effect, in addition to the more widely known EXAFS and XANES techniques, inner shell X-ray spectroscopies like X-ray emission spectroscopy (XES), high energy resolution fluorescence detection (HERFD), resonant inelastic X-ray scattering (RIXS), scattering (X-ray diffraction Pair Distribution Function (XRD/PDF) and small and wide angle X-ray scattering (SAXS/WAXS)) techniques have emerged as powerful research methods for investigations on inhomogeneous nanomaterials (Alayoglu *et al.*, 2005; Singh *et al.*, 2010; Glatzel *et al.*, 2005).

Demanding efforts can be found in recent literature, combining X-ray based synchrotron techniques, in order to approach the problem of characterization of CS NP. Recently, M.D. Mizrahi at al. (2018) used small angle X-ray scattering, X-ray fluorescence and extended X-ray absorption fine structure spectroscopy to probe the structure of chemically synthesized CoPt3 NPs after ligand removal. They show that surface purification results in the considerable leaching of the Co atoms from the CoPt3 NPs, converting them into CoPt3@Pt core@shell structures with a thick Pt shell of half of nanometer. These results are also compatible with the improved catalytic activity of extensively purified NPs in octyne hydrogenation reaction found for the same samples.
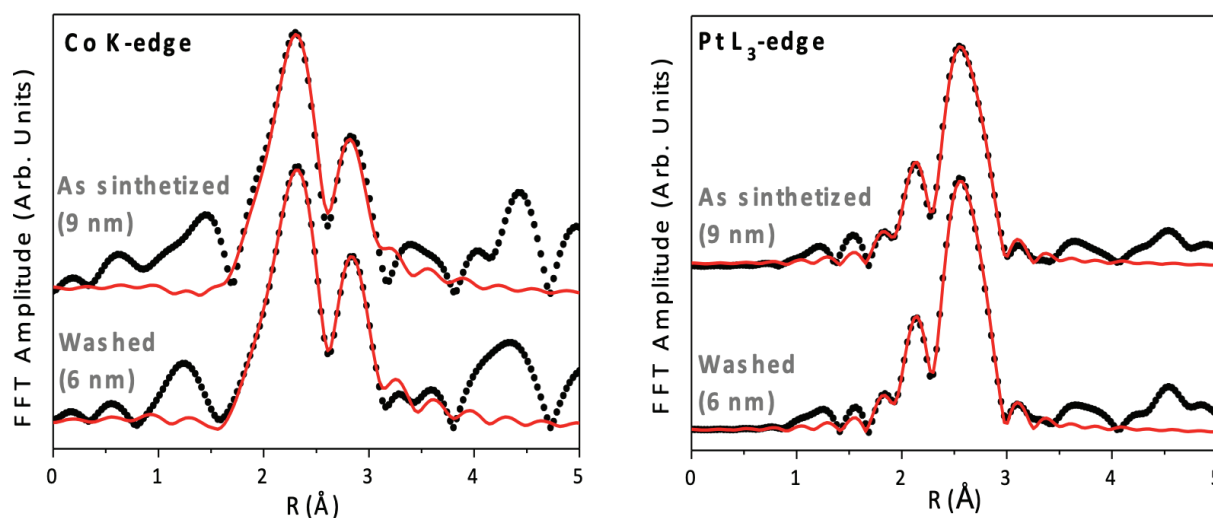

Figure 1. Experimental and fitted EXAFS Fourier Transform of fresh and washed NP samples at Co K and Pt L3-edges (left and right panels, respectively). Red lines correspond to the EXAFS fitting (see Table 2 for fitted parameters).

NPs of alloys of Pt with transition metals present exceptional catalytic properties (Jiang *et al.*, 2017; Li *et al.*, 2015). The determination of the thin external shell is not evident in polycrystalline Pt alloyed with 3d-transition metals. However, the advanced catalytic properties of Pt-based alloy films were often attributed to the formation of Pt-skin (van der Vliet *et al.*, 2012). The authors also demonstrate that drastic compositional and structural transformation occurs during the removal of native ligands via the solvent/non-solvent approach, leaching cobalt atoms in aqueous media. This kind of effect at surface of bimetallic NPs, experimenting complex transformations upon their exposure to different media, was reported previously. Thus, experimental studies on 10 to 12 nm Co-Pt alloy NPs showed the migration of Co atoms and the formation of a strained epitaxial CoO film upon their high temperature exposure to oxygen, while in a reducing hydrogen atmosphere, Co atoms migrated back to the bulk, leaving a monolayer of platinum atoms on the surface (Xin *et al.*, 2014).

In their work, Mizrahi *et al.* (2018) focus on understanding the effects of NP purification on surface composition and structure of bimetallic Pt-based alloy NPs synthetized in organic solvent. Many techniques are conjugated for that purpose: Transmission Electron Microscopy (TEM), Small Angle X-ray Scattering (SAXS), X-ray fluorescence (XRF) and Extended X-ray Adsorption Fine Structure spectroscopy (EXAFS), and all together provide a detailed analysis of the structure of chemically synthetized CoPt3 NPs after ligand removal. The purification process is applied on 9.3 nm CoPt3 NPs sample (in the following "as prepared" sample) to obtain 5.9 nm CoPt3 NPs sample (in the following "washed" sample) with the formation of 0.5 nm thick Pt shell. Thus, they demonstrate that the phase transfer of CoPt3 NPs and their prolonged exposure to water can result in the formation of thick Pt shell during extensive surface purification implemented for effective ligand exchanges and phase transfer.

Table 2. EXAFS Fitted parameters for both NPs as synthetized and washed samples at the K-Co edge (left) and L3-Pt edge (right). Parameters for CoPt and CoPt3 reference compounds are also included for comparison.

	K-Co					L$_3$-Pt					
Sample	N_{CoPt}	$R_{Co\text{-}Pt}$ (Å)	$\sigma^2_{Co\text{-}Pt}$ (Å²)	N_{CoCo}	$R_{Co\text{-}Co}$ (Å)	N_{PtPt}	$R_{Pt\text{-}Pt}$ (Å)	$\sigma^2_{Pt\text{-}Pt}$ (Å²)	N_{PtCo}	$R_{Pt\text{-}Co}$ (Å)	$\sigma^2_{Pt\text{-}Co}$ (Å²)
As sinthetized	11.4_{10}	2.72_3	0.009_1	--	--	8.7_4	2.74_2	0.007_1	1.9_3	2.70_2	0.009_1
Washed	10.6_{10}	2.70_3	0.008_1	--	--	8.3_4	2.73_1	0.006_1	1.7_3	2.69_1	0.007_1
CoPt	8	2.65		4	2.69	4	2.69		8	2.65	
CoPt$_3$	12	2.71		0	--	8	2.71		4	2.71	

EXAFS was specially employed to analyze the local environment of Pt and Co separately in water-transferred NPs. Specifically, different phases or species segregation can be analyzed considering the fitted average coordination value <N>, correlating it with the size of the cluster domain (Frenkel *et al.*, 2011). Figure 1 shows the Fourier transforms of the EXAFS oscillations obtained at the Co-K and Pt-L3 edges, as well as the corresponding fitting curves for as-synthetized and washed samples. A model with two coordination shells with Co and Pt atoms as scatters in each shell is used to fit Pt-L3 EXAFS data, while only one coordination shell of Pt is enough to fit Co-K edge EXAFS data. EXAFS results at the Co K-edge revealed the Co-Pt interatomic distance of about 2.72(3) Å, similar to 2.71, characteristic of the CoPt3 massive alloy. Only a Pt coordination shell was found around Co atoms, which is indicative of CoPt3 structure. Fitting of the EXAFS data obtained at Pt L3-edge also indicated that the Co-Pt interatomic distances are similar to those of CoPt3 alloy. Even though a contraction of Pt-Pt distances is expected (Nepijko *et al.*, 1980) due to the enhancement of surface tension in NP, the interatomic Pt-Pt distances derived from Pt-L3 EXAFS fitting curve are greater than those in both CoPt3 and CoPt alloys. These EXAFS results can be explained by the coexistence of bimetallic and metallic phases. In effect, EXAFS fitting data indicate a higher number of the Pt atoms coordinated to other Pt atoms (8.7(4) vs. 8, characteristic to CoPt3 alloy) and lower number of Pt atoms coordinated to Co atoms (1.9(3) vs. 4, characteristic to CoPt3 alloy) (see Table 2). Thus, by double checking, EXAFS can probe, by both the interatomic distance and the average coordination numbers, the presence of two Pt-containing phases: metallic Pt and Pt-Co alloy, most likely CoPt3. Since NPs had spherical shape (probed by HRTEM and SAXS), it is reasonable to assume spherical CoPt3@Pt core@shell structure.

The effect of washing (purification) can also be inspected by XANES. In effect, the presence of a CoPt3 phase is also supported by Co K-edge XANES experiments (Figure 2). The positions of the characteristic features and the intensity of the white line in the Co K-edge XANES spectrum of extensively washed CoPt3 NPs are nearly the same as those of theCoPt3 bulk alloy reference (Figure 2) (the pre-edge feature at 7709 eV and the bump at 7725 eV that correspond to transitions from 1s to 3d and 1s to 4d orbitals in Co atoms, respectively). As regards as-synthesized 9.3 nm CoPt3 NPs, the CoPt3 XANES spectrum is clearly different, suggesting some differences, in average, in the local coordination of the Co atoms between as-synthetized and extensively purified CoPt3 NPs. The Co K-edge EXAFS study on as-synthetized

CoPt3 NP indicates the presence of additional coordination shells for Co with Co-Co and Co-O contributions (not shown here), consistent with the presence of oxidized Co atoms at the surface of the as-synthetized NPs.
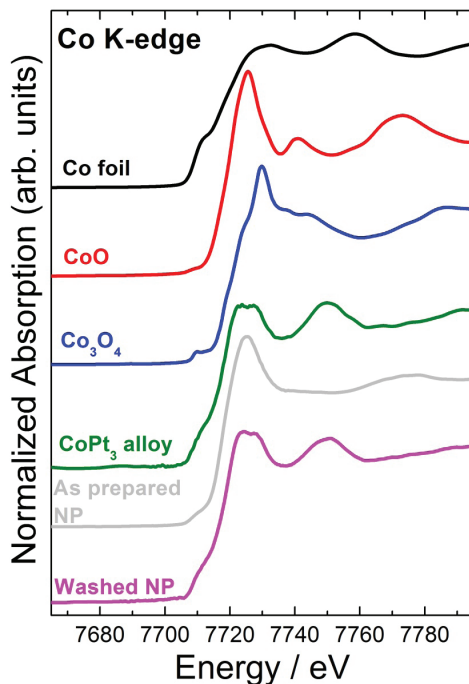

Figure 2. XANES spectra at the Co-K edge of as-prepared and washed samples compared to metallic Co foil, CoO, Co3O4 and CoPt3 alloy reference compounds. Note the energy edge position of samples coincident with metallic Co foil reference and the similarity between the washed sample and the CoPt3 alloy reference compound.

Since the average coordination number <N> is directly associated with the geometry in the solid, sensitivity increasing as particle size decreases, the fitted <N> value from EXAFS experiments can be used to infer the size of the particle (assumed spherical). With this goal, we can calculate the theoretical average coordination numbers N_{Pt-Pt} and N_{Pt-Co} (Figure 3, red and blue curves, respectively) for CoPt3@Pt core@shells NPs with different CoPt3 core radii, keeping the external radius of NPs fixed to 4.65 nm as it follows from the TEM data. These findings will allow the estimation of the alloy core in water transferred NPs. In Figure 3, the horizontal green bars represent the average coordination numbers N_{Pt-Pt} and N_{Pt-Co} determined by the EXAFS experiments. Then, the area of intersection between the grey bars and the calculated curves (Figure 3, vertical bar) shows that the radius of the CoPt3 core was in the range between 3.8 nm and 4 nm (corresponding to a larger thickness of the Pt shell of about 0.75 nm, estimated by the analysis of the concentration of the leached ions) (Krylova *et al.*, 2010). Figure 4 shows the representation of the possible structure for as-prepared and washed NPs.
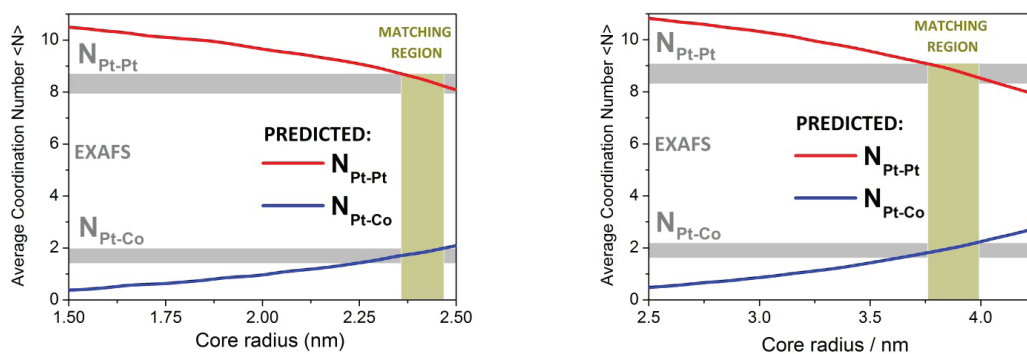
Figure 3. Calculated average coordination numbers, N_{Pt-Pt} (red line) and N_{Pt-Co} (blue line) as a function of CoPt3 core radius NP as prepared and washed (left and right panel respectively). The grey horizontal bars represent the average coordination numbers derived from the EXAFS fits. The vertical bar indicates range of the CoPt3 core radius NP that allows obtaining the coordination numbers matching the experimental data.
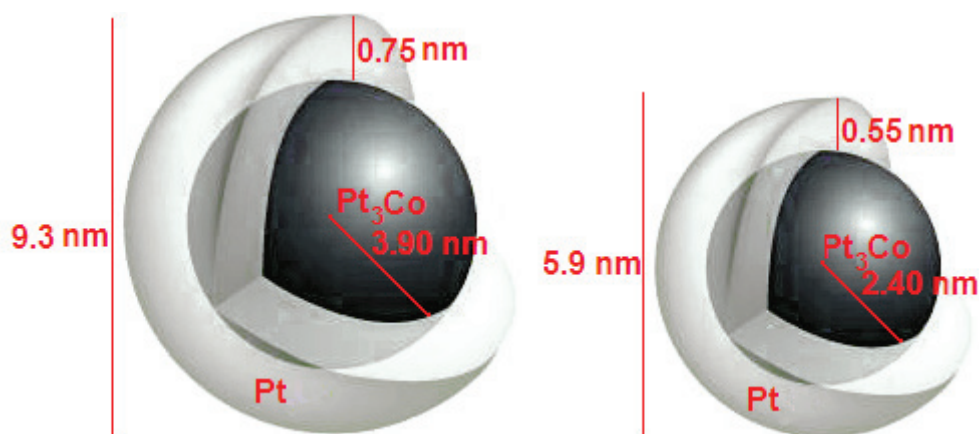
Figure 4. Representation of the proposed core@shell structure for as-synthetized and washed NPs (left and right respectively) derived from EXAFS fittings and XANES spectra, compatible with calculated averaged coordination number for determined structures.

XRF data allows confirming the derived estimation of the Pt-to-Co atoms ratio, based on the core@shell model with about 0.75 nm shell. The estimated value is 5.7(6), in good agreement with the ratio of 5.4 calculated based on the model. On the contrary, when the alternative configuration, such as Pt@CoPt3 and a random distribution of Pt and Co atoms, is calculated, a value of 4.8 is obtained, which does not match experimental florescence experiment results. These findings are also in agreement with EXAFS predictions, making the hypothesis even more robust.

An additional and direct experimental validation of the CoPt3@Pt core@shell model was performed by SAXS on the same samples under the same conditions (in water solution at room temperature). The corresponding fitting with a core of CoPt3 alloy and Pt atoms shell model is shown in Figure 5. The mean core radius and shell thickness values obtained by SAXS fittings are in good agreement with EXAFS results. The advantage of SAXS with respect to TEM determinations is not only the fact the experiments can be performed on liquid samples, but also that SAXS provides information averaged over a large volume of NPs. This is much more representative of the general state of the sample, while TEM is limited to the analysis of hundreds of NPs.
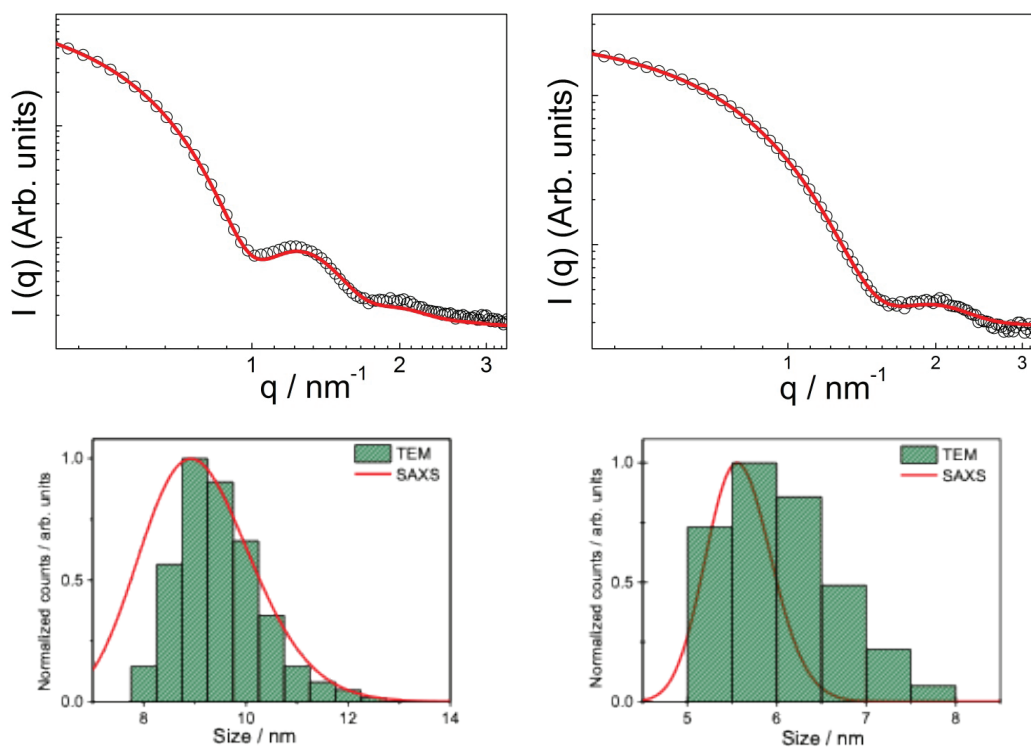

Figure 5. Experimental SAXS data (intensity vs. wave vector q - open symbols) for as-prepared and washed NPs (upper left and right panels, respectively) and the fitting curve obtained based on a spherical core/shell model. The size distributions reconstructed from fitting curve were overlapped with size distribution data obtained based on TEM data (lower panels).

In conclusion, X-ray-based techniques EXAFS, XANES, XRF and SAXS consistently support the same model for the core@shell structure of water transferred NPs. Based on this, the authors suggest that cobalt atoms leached only from the surface of CoPt3 NPs based on the analysis of the concentrations of the leached Co (+2) ions to the water by zero explains the suppression of CoPt3@Au dumbbells formation when extensively washed alloy NPs were used as seeds (Krylova *et al.*, 2012). These findings, summarized in Table 3, also contribute to enlighten the control mechanism, by the solvent/non-solvent approach, to regulate the properties of multicomponent, transition metal based NPs for wanted applications.

Table 3. Comparative summary indicating the contribution from each X-ray technique for the characterization of core@shell NPs.

Technique	Data/Parameters	Information provided
EXAFS	- Average coordination number - Interatomic distances Pt-Pt, Pt-Co, Co-Pt and Co-Co	- Pt and Co-species, core@shell model - Pt and Co species
XANES	- Absorption spectrum - Energy edge position	- Chemical speciation - Average oxidation state for Co and Pt
XR Fluorescence	- Intensity of Co-$K_{\alpha 1}$ and Pt-$L_{\alpha 1}$ fluorescence lines (not shown in this work)	- Co/Pt relative atomic concentration - Pt and Co stoichiometry of species
SAXS	- Radii of gyration (considering the whole particle)	- Size distribution, shape, core@shell model, core radius, shell thickness

X-rays micro and nanoprobes: background, technical aspects and opportunities in nanoscience

Characteristics of X-rays micro and nanoprobes

X-rays micro and nanoprobes (XMNP) represent an unbeatable opportunity for pioneering research, both for basic investigation and in close relation to practical industrial applications. The scientific projects planned to be performed at these types of beamlines at synchrotron laboratories cover different fields, where spatial resolution and chemistry (or electronics) play a fundamental role.
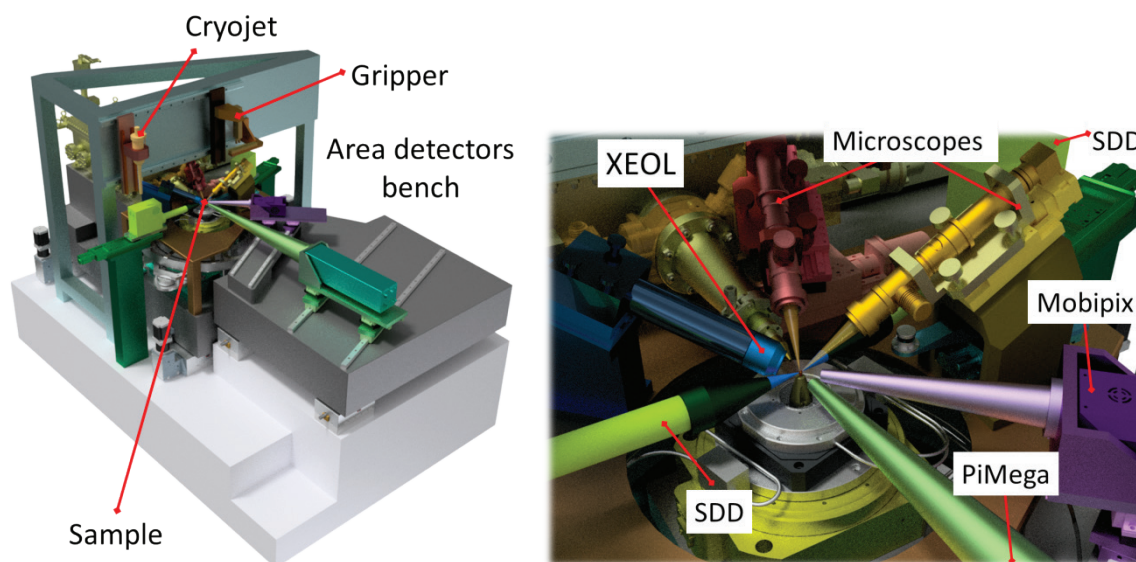
Figure 6. Scanning probe TARUMÃ at CARNAUBA nano and microprobe beamline. SIRIUS synchrotron laboratory in Campinas, Brazil. (Figure by courtesy of H. Tolentino, SIRIUS, Campinas, Brazil (H.C.N. Tolentino, R.R. Geraldes, 2019).

At these new XMNP end-stations, it is feasible to find opportunities for X-ray fluorescence (XRF), X-ray absorption fine structures (XAFS), and X-ray excited optical luminescence (XEOL). The primary enabling experimental technology

for focusing X-rays to such small spots has been the development of X-ray optics. Their applications, however, have been limited by the trade-off between useful flux and resolution. In general, to satisfy the diverse requirements of various X-ray techniques, several design criteria are set for modern XMNP beamlines: (1) minimum number of beamline optical elements to preserve source coherence; (2) nano-focusing optics with a diffraction-limited spot; (3) high throughput optics; (4) achromatic optics; (5) large working distance; and (6) minimum mechanical and ground instabilities. The technical qualities of different beamlines for XNMP are outlined in Table 4.

Representative scientific cases that can be specially afforded by XMNP beamlines cover, in general, a diverse field of research, such as material science, MEMS/NEMS device characterization, cultural heritage, *in vivo* and *in vitro* bio-materials and cells, geology, etc. In the following section, specific examples are reported, in particular in the field of material science characterization.

Table 4. Characteristic parameters of recent and planned and constructed X-ray nano-probe beamlines.

Beamline/Syncrotron	Energy range [keV]	Energy resolution [$\Delta E/E$]	Beam size [nm] (focal point)	Photon flux [photons/s]	Emittance [nm·rad] (synchrotron ring)
XNP, Taiwan Photon Source (Hsinchu, Taiwan) (Yin *et al.*, 2016)	$4 - 15$	$\leq 1.5 \times 10^{-4}$ Si (111)	40 (@ 10 keV)	$1\text{-}10 \times 10^{10}$	1.6 @ 3 GeV
Carnauba, SIRIUS Campinas, Brazil (Tolentino *et al.*, 2017; Tolentino *et al.*, 2019)	$2.05 - 15$	1.0×10^{-4}	TARUMÃ (sub-Microprobe) $500 - 100$ SAPOTI (Nanoprobe) $120 - 30$	3.5×10^{12} (2 keV) 2.5×10^{12} (4 keV) 1×10^{12} (10 keV)	0.25 @ 3 GeV
ID16B, ESRF Grenoble, France. (Martínez *et al.*, 2016)	$6 - 65$	10^{-2} (PM#) 10^{-4} (MM##)	50 x 50 (PM) 80 x 100 (MM)	$10^{11}\text{-}10^{12}$ (PM) $10^{8}\text{-}10^{9}$ (MM)	3.8 @ 6 GeV
HXN, NSLS II Brookhaven, USA. (Nazaretski *et al.*, 2017)	$6 - 25$	1.3×10^{-4}	10×10 (MLL*) 30×30 (FZP**)	$> 5 \times 10^{8}$ (10 keV)	< 0.5 (H) $\times 0.008$ (V) @ 3 GeV

pink mode, ## monochromatic mode, * Multilayer Laue Lens, ** Zone Plate Focussing

Present and future of X-ray probes in nanoscience

Third-generation synchrotrons start the revolution in scientific instrumentations over the past decade. In particular, the development of advanced imaging micro and nanoprobes constitutes a technology breakthrough in the field of x-ray optics (De Andrade *et al.*, 2011; Nazaretski *et al.*, 2015; Shapiro *et al.*, 2014; Winarski *et al.*, 2012). Different unique characteristics of X-rays, such as resolution, sensitivity and speed, and their ability to penetrate matter, constitute an important opportunity for the future for scientific research in nanoscience. The varying ability of different probes compared with X-rays still needs to be bridged in terms of spatial resolution. This is a very challenging field where the spatial resolution limit is pushed constantly. However, the ability of spatial resolution must be weighed integrally comparing different probes, considering pros and cons, for a realistic assessment. In effect, among photons, different probes can be considered to obtain space-resolved structural or compositional information, including photons obtained from laser sources, electrons, neutrons, and ions (Mino *et al.*, 2018). Even if laser and x-ray microprobes have similar characteristics (they are both based on photons), the main differences between them are their wavelength range (while laser microprobes operate within a wavelength range of a few microns to around 200 nm, x rays work within a 10-0.01 nm range) and the much higher coherence of laser beams compared to synchrotron x-ray sources. Having a lot more versions of different methodologies to approach different topics, the comparison between electron and X-rays microprobes deserves more comments

and comparisons: XRD versus electron diffraction, XAS versus electron energy loss spectroscopy (EELS), XRF versus energy-dispersive x-ray (EDX) spectrometry, x-ray emission spectroscopy (XES) versus electron probe microanalysis (EPMA). Our aim in this section is not focusing on an in-depth discussion of all these comparisons, but mentioning the ones that can be applied to relevant aspects of nanomaterials characterization.

It is already well known and already spread in most of the laboratories that a single electron microscope offers multiple characterization techniques, combined with an outstanding spatial resolution. Despite the well-known capabilities of electron microscopes based-techniques, there are many disadvantages that limit their use for the characterization of several samples. In particular, sample preparation could be a strong limitation in electron microscope studies, which can be challenging and could even modify the intrinsic properties of the samples to be studied – the requirement of very thin samples ($\leq$100 nm), sometimes the need to prepare sample using sophisticated procedures such as focused ion beam (FIB) setups. As the reverse of the surface selectivity of electron probe methods, there is a strong limitation for a bulk characterization or for the analysis of buried or embedded volume portions. Regarding sample damage during experiments, the intense electron beams or higher energies required to increase penetration depth can result in significant radiation damage, mainly because electrons are capable of transferring relatively large momenta to the sample (García de Abajo *et al.*, 2010). Another critic disadvantage for techniques based on electron probes is the need to operate under high vacuum, with the obvious limitations for reproducing different in situ environment setups for many types of research topics. As regards the known chemical selectivity of X-rays, unless XRF or Auger spectroscopies are used as probes, electron microscopes present an important drawback compared to x rays. On the other hand, ion probes have the significant particularity, as opposed to photons or electrons probes, that they deposit extremely localized densities of energy to the target in a very short time (from the kinetic energy of ions) (Ziegler *et al.*, 1985; Avasthi *et al.*, 2011). However, the size of the spot in this case can be a very small region of about 10 nm with advanced focusing and/or collimation (Yao *et al.*, 2015). Finally, neutron probes, extensively employed, include many advantages compared to the rest of probes, and they can complement the advantages of X-rays probes. Among them, we can distinguish sensitivity to hydrogen (Neumann, 2006), isotope specificity, and magnetic interaction (Fitzsimmons *et al.*, 2004). Finally, the strong penetration depth makes it ideal for bulk probes. Nevertheless, a major obstacle in the (sub)micrometric characterization of materials with neutrons, besides the technical limitation in manufacturing the focusing devices, currently located in the range of fraction of mm, is the relatively low flux provided by present neutron sources. To obtain a similar brightness of x rays produced by third- and fourth-generation synchrotron, for neutron sources it necessary to increase the production of neutrons about 2 orders of magnitude.

Let us consider the x-ray-based methods and their opportunities with the micro and nanoprobes versions in more detail. X-ray probes can offer outstanding possibilities for nondestructive characterization at the (sub)micrometric scale, overcoming many limitations already described by other probes like ions, neutrons or electrons. In general, their advantages include the availability of several, often complementary, physical process or magnitudes (e.g., absorption, emission, scattering, diffraction, phase contrast, and polarization), simple sample preparation procedures, and due to the long mean free path of energetic photons, the possibility to perform experiments at *in situ* or *operando* conditions. In effect, energetic x rays (hard-x-rays) have low cross sections for their interaction with matter, allowing nondestructive characterization experiments, applicable at pressures around atmospheric conditions, liquid media like water, and any other non-strong absorbing or dispersive environments. These low cross-section values also involve high penetration depths through volume matter, offering the opportunity of 3D analysis. At this time, the available or programmed 4th generation synchrotrons, with high brilliance and low emittance beams facilitates high density of data, with reasonable signal-to-noise ratio, even at the (sub)micrometric scale with relatively short acquisition times.

Different micro and nano-spectroscopic techniques are currently in constant development. Thus, we can find x-ray absorption for micro- and nano-XAS (XANES) (Cotte *et al.*, 2011), EXAFS (Martínez-Criado *et al.*, 2014) and polarization-dependent methods, e.g. micro- and nano-XMCD (Suzuki, 2014) (x-ray magnetic circular dichroism), or very advanced spectroscopic approaches such as RIXS (resonant inelastic x-ray scattering). Still more established microspectroscopic techniques are micro-XRF (Provis *et al.*, 2009), micro-XEOL (Villanova *et al.*, 2012) x-ray-excited optical luminescence and micro(nano)-XPS (Kolmakov *et al.*, 2008) (x-ray photoelectron spectroscopy).

Diversity of scientific cases with X-ray micro and nano-probes studies

Typically, X-ray based synchrotron techniques are presented as ensemble averages, and sometimes this characteristic is complementary to traditional microscopic ones, which probe objects individually. Currently, due to recent advances in X-ray sources, X-ray optics and X-ray methods, XMNP emerges as unprecedented and possible tools to image crystalline structure distributions in materials science. Thus, nanobeams combined with diffraction have made possible imaging parameters in individual nanocrystals, and coherent nanobeams offer the opportunity to image nanomaterials in three dimensions with a resolution far smaller than that of the traditional focused beam size. Thus, the traditional requirement about sample homogeneity for X-ray absorption techniques can be omitted nowadays. This "old" precept can be abandoned since the allowed spatial resolution allows studying homogeneous regions in highly heterogeneous samples.

Combining of advanced X-ray characterization tools with higher-resolution imaging techniques facilitates further breakthroughs. In the field of technological applications, the synchrotron microanalysis technique applied to potential photovoltaic materials is one of the examples with high impact. New characterization tools allow developing advanced materials for solar cells (Villanova *et al.*, 2012), unraveling the structure-property relationship thanks to the large penetration depths, high throughput and good tunability (energy, spot size, photon flux, polarization, etc.). One important aspect is the possibility of *operando* and *in-situ* studies – hard X-ray beam intensities allow simultaneous signal acquisition and analysis of buried structures and mechanism process studies under realistic thermodynamic conditions. Different methodologies already demonstrated their efficiency on solar-cells characterization – X-ray diffraction (XRD) and small-angle X-ray scattering (SAXS) techniques have provided structural information at the atomic and mesoscopic scales (Schorr, 2011; Chiu *et al.*, 2008), and X-ray absorption spectroscopy (XAS) has delivered information on local phenomena helping identify degradation and failure mechanisms (Buonassisi *et al.*, 2005). X-ray microprobe beams can also be applied for material characterization of MEMS/NEMS devices (Bleuet *et al.*, 2009). In effect, the structure of microsensors or micro-actuators must be nondestructively evaluated. TEM/SEM are frequently used because of their better resolution compared to X-ray microscopy, X-ray microprobe being better for probing deeper regions into the sample. Additional advantages are found for X-ray imaging due to the possibility of working under non-high vacuum conditions, the absence of special requirements for sample conductivity, and less tedious sample preparation procedure, especially for non-conductive samples. Innovative applications of synchrotron X-ray nano-probes in the field of cultural heritage can also be found. This modern, non-destructive application of nano-beams can produce high-spatial-resolution information on fragmented samples in historical or model artworks and constitutes a unique opportunity to revisit those fields of research (Cotte *et al.*, 2018). Different techniques, such as nano-X-ray fluorescence, can be applied to probe elements. Nano-X-ray diffraction is useful to identify crystalline phases, and nano X-ray absorption spectroscopy is a sensitive tool for speciation. More challenging, computed tomography-based techniques can provide additional information about the morphology and porosity of materials.

A special chapter can be devoted to bio-metals imaging and speciation in cells using proton and synchrotron radiation X-ray microspectroscopy. XMNP allows chemical element analysis in subcellular compartments. Indeed, the imaging and quantification of trace elements in single cells can be obtained using particle-induced X-ray emission (PIXE). The combination of PIXE with backscattering spectrometry and scanning transmission ion microscopy provides a high accuracy in elemental quantification of cellular organelles. On the other hand, synchrotron radiation X-ray fluorescence provides chemical element imaging with less than 100 nm spatial resolution. High resolution multi-element analysis techniques are especially relevant because they allow simultaneous mapping of essential elements. In this context, two promising techniques for characterizing the sub-cellular distribution of metallodrugs are secondary ion mass spectrometry (SIMS) and synchrotron-based X-ray fluorescence (SXRF). *In vivo* and *in vitro* studies are possible by micro-SXRF studies (for instance, for anticancer metal compounds), determining metal distribution inside cells for many elements at the same time (Morrison *et al.*, 2014; Wu, L.E. *et al.*, 2016). Additionally, synchrotron radiation offers the unique capability of spatially resolved chemical speciation using micro-X-ray absorption spectroscopy (Sanchez-Cano *et al.*, 2019).

Micro and nanoprobes for nanomaterials characterization

Clearly, nanoscience and nanotechnology are two of the research and technology fields that benefited the most – from advanced electronics to energy harvesting, energy storage and catalysis. A wide range of actions became a reality – creation and manipulation of structural features such as defects, connections with other structural and size effects, metastable structural phases, precisely strained materials, and precisely designed nanoscale configurations of magnetic and electronic order (Hofmann *et al.*, 2017; Ice *et al.*, 2011; Holt *et al.*, 2013). Constant and challenging issues in the field of nanoscience find today a new opportunity to be solved – understanding macroscopic materials through their nanoscale structural properties, the ability to characterize the resulting structure with high structural precision and in an appropriate timescale. In summary, the general study of the effects of structure, environment, and time-evolution of defects, interfaces, and domains at nanometric scale on material properties can be boarded by new micro- and nanoprobe-based techniques.

X-ray diffraction in isolated nanocrystals reveals details of their specific mechanical and chemical properties in comparison to their bulk counterparts. The sensitivity of the technique to interatomic distances, combined with the spatial resolution (between 10 to 1000 nm), both reveals and corroborates the presence of microstructural heterogeneities that, from traditional X-ray diffraction experiments, were previously only described by averaged information. Thus, this emerging approach allows to reveal the mechanisms through which the enhanced properties of nanomaterials emerge in great detail in a vast number of hard condensed matter systems. It covers basic and applied areas, such as ceramics or metals, where their macroscopic mechanical properties are defined at the mesoscale by the interaction of defects and crystallites. Magnetic or multiferroic materials are additional examples where domain structures can now be resolved, up to technological fields ranging from catalysis to batteries, where the local influence of dislocations on damage mechanisms, during charge and discharge cycles of Li-ion batteries, can be imaged with coherent X-ray nanobeams (Ulvestad *et al.*, 2015) or discern-

ing strain fields in semiconductor devices during process at relevant temperatures (Vianne *et al.*, 2015). More specifically, the information concerning the local structures and electronic structures surrounding the dopants and constituent atoms in nanostructures is essential to understand the fundamental mechanism leading the favorable properties. Indeed, it has been demonstrated that nanocrystals of semiconductors with different shapes present widened bandgaps, ultra-fast transitions, and photoluminescence efficiencies due to the quantum confinement effects, which can be explained based on their unique physical properties (Yan *et al.*, 2015).

The cocktail of chemical selective techniques like nano-EXAFS, nano-XANES and nano-XEOL, using focused X-ray beam on isolated nanostructured semiconductors, can be used to distinguish different regions, like surfactants or substrates. Moreover, in the case of nanoscaled functional materials, it becomes essential to correlate structural and optical properties by applying different techniques sensitive to the structure and chemistry to the same nano-object (where the use of non-destructive and contact-less techniques is convenient). The traditional techniques employed for the study of the core@shell NPs, up to this moment, had been the high resolution scanning transmission electron microscopy (HR-STEM) (Koester *et al.*, 2011), with the already described limitations or constraints.

Micro and nanoprobes for inhomogeneous nanomaterials characterizations

Recently, Secco *et al.* (2019) performed a detailed study of GaN/InGaN nanowire (NW) heterostructures. Individual NWs were dispersed on 200 nm-thick SiN windows for measurement at the nanoimaging station ID16B of the European Synchrotron Radiation Facility (ESRF, Grenoble, France). The authors claimed that such InGa-based nanowires forming core@shell structures, typically present inhomogeneities in their elemental composition, defect concentration, and strain fields at the nanoscale. Being their characterization very complex and costly by conventional techniques, the synchrotron X-ray nanoprobe emerges as an alternative multi technique approach. Thus, it is possible to follow the elemental composition and distribution by X-ray fluorescence (XRF), strain fields and crystal quality by X-ray diffraction (XRD), and local order effects and elemental segregation by X-ray absorption near edge structure (XANES) spectroscopy.

The distribution of Ga and In in the NWs could be elucidated from the XRF intensity maps (Figure 7), showing that Ga is homogeneously distributed along the NW axis. Complementarily, the intensity of In shows an increment from the bottom to the top end of the NW (the higher intensity of In at the top of the NW does not correspond to the formation of polar MQWs, which is demonstrated by EDS). Au and Ag maps (see Figure 8) lead to the conclusion that no catalyst atoms are disseminated in the NWs. Additional evidences are achieved from longitudinal and radial scans of the XRF (see Figure 7). These profiles confirm that there is an InGaN shell structure with an increasing concentration of In towards the top of the NW. Ga atoms, on the other hand, are more evenly distributed.
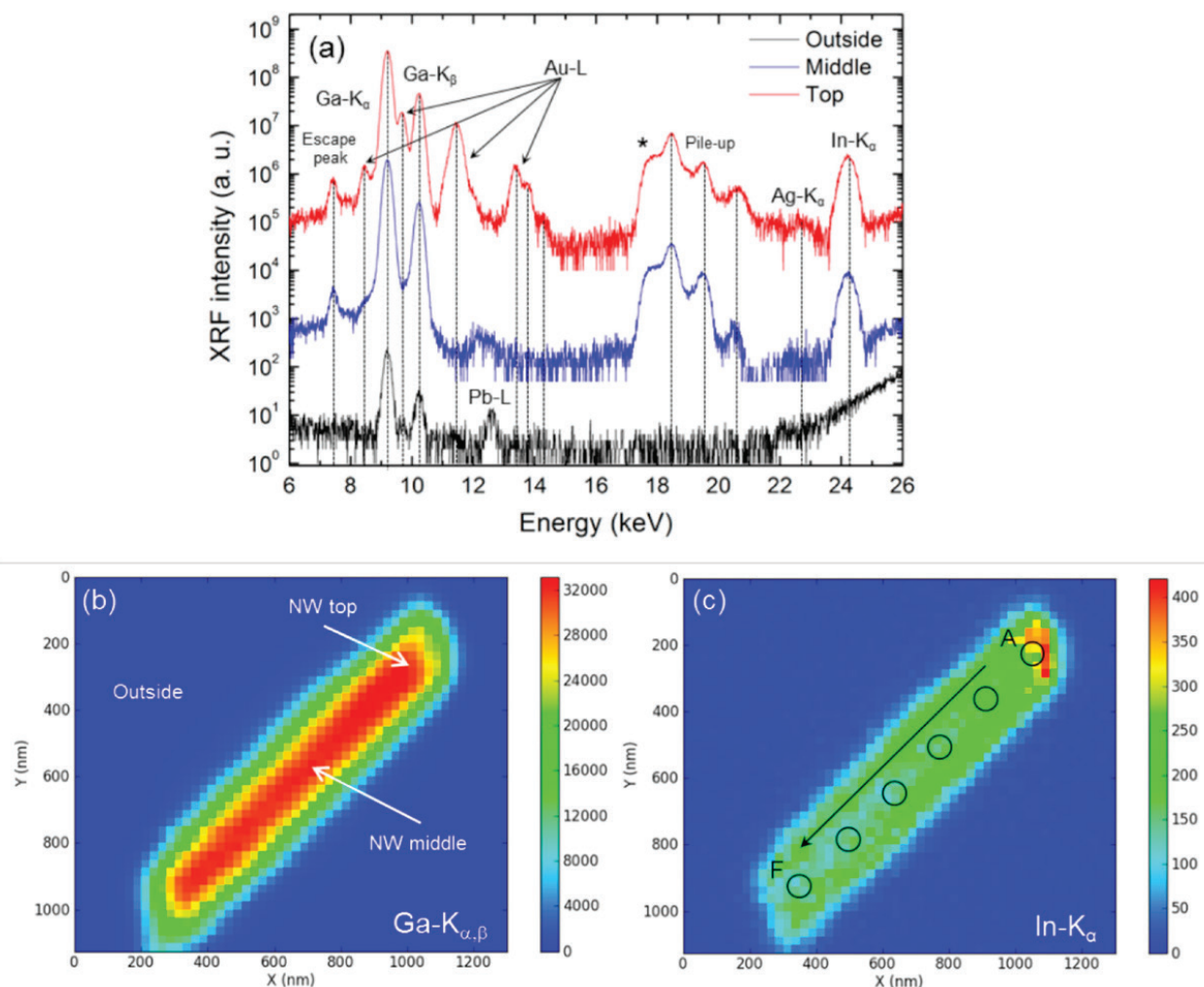
Figure 7. (a) Averaged X-ray fluorescence (XRF) spectra from locations at the top (red) and middle (blue) of the NW, and at an outside region (black). The labels indicate the elements associated with each peak identified with PYMCA. The asterisk represents an artifact coming from the measurements. The XRF intensity color maps of Ga and In in the scanned area are shown in (b) and (c), respectively. Red (blue) color corresponds to high (low) fluorescence intensity (scale in counts). The black circles in (c) indicate the regions of NW along its axis in which In concentration has been estimated (Figure published with permission of Secco *et al.* (2019).
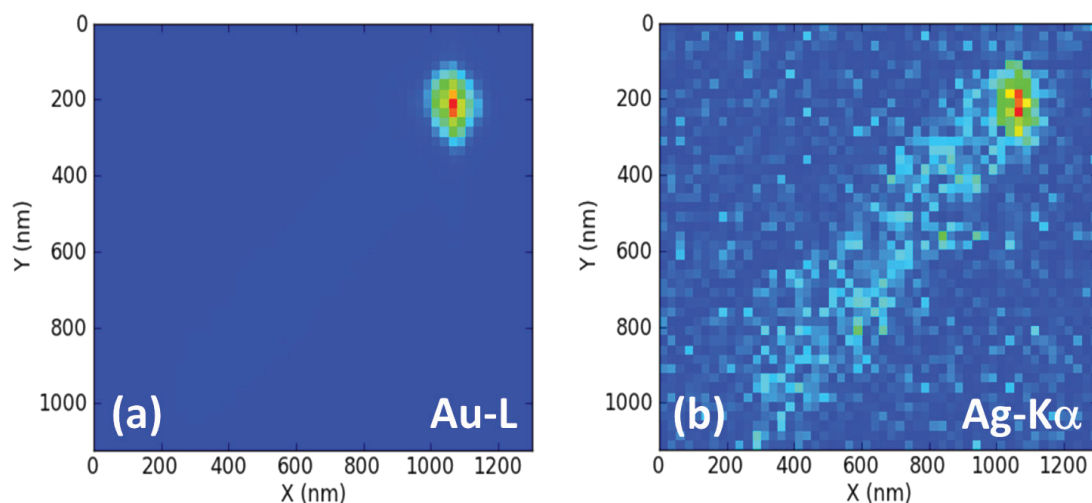

Figure 8. XRF colour map distribution of (a) Au and (b) Ag along a representative NW. The colour scale represents the XRF intensity in photon counts and ranges from 0 to 9000 (for Au) and from 0 to 25 (for Ag) (Figure published with permission of Secco *et al.* (2019).

The crystal phase and lattice parameters of different regions across single NWs can be investigated by nano-XRD. The short distance separating the CCD and the sample allowed measuring three diffraction peaks simultaneously: (104), (210), and (211) reflections of unstrained wurtzite GaN, which were only detected by analyzing the XRD signal of the whole NW, suggesting that the core-shell InGaN MQWs are completely lattice matched to the strain-free GaN core. This is also confirmed by the absence of a distinctive XRD peak coming from core-shell MQWs, which are completely strained (compressed along the *a* and *c* directions and expanded along the m-direction). Additionally, XRD reflections allow calculating the interplanar distance, dhkl, using the general relation between interplanar distances (d), Miller indices (hkl), and lattice parameters (*a* and *c*) in the wurtzite structure. Thus, lattice parameters *a* and *c* in the studied NWs can be measured, their evolution along the *z*-axis of the NW showing no evolution in *a* and a non-monotonous increase in *c* towards the NW top. The studied area starts at the middle and goes up the top of the NW (no signal was registered between the bottom and the middle of the NW due to the loss of the Bragg condition at imperfections on the NW).

Complementary to XRD measurements, which probe the long-range structural order, XANES experiments were performed for studying the local arrangement around Ga atoms in NWs. Figure 9 shows typical XANES spectra for a single NW using perpendicular and parallel polarization in relation to the NW axis, X-ray beam. For comparative purposes, a high-quality *c*-oriented GaN reference layer was also measured with polarized X-rays in relation to the wurtzite *c*-axis. This comparison allows concluding, since the spectra of the NW matches that of the reference, that the NW has a wurtzite structure and there is no mixture of phases. Indeed, the axis of the NW corresponds to the c-axis of the wurtzite structure.

This characterization is an illustrative example where the combination of XRF and EDS gives a reliable picture of the detailed structural characterization, despite the complexity of the NWs nanostructures, because of their inhomogeneities in composition and strain at a nanometer length scale. Similarly, XANES and XRD probe local and long-range order in such heterostructures – determinations of the In concentration in the QWs allows strain state calculations from XRD spectra. Finally, In content fluctuations can explain the variations in the emission energy and the broadening of emission peaks photoluminescence spectra in individual NWs, which can be interpreted and modeled theoretically.
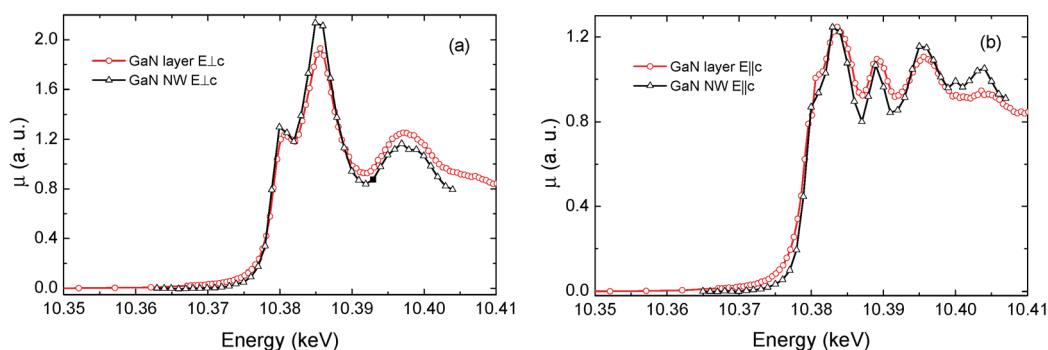

Figure 9. Comparison between X-ray absorption near edge structure (XANES) spectra of a high quality reference GaN layer (red circles) and those of the NW (black triangles) for different X-ray beam incident angles: polarization (a) perpendicular and (b) parallel to the wurtzite *c*-axis (Figure published with permission of Secco *et al.*, 2019).

Conclusions

We listed a series of experimental methodologies based on X-ray probes that offer unique possibilities for nondestructive characterization, overcoming many limitations present in other probes such as ions, neutrons or electrons. The different techniques are based on complementary physical process (e.g., absorption, emission, scattering, diffraction, phase contrast, and polarization), which are compatible with feasible sample preparation and the possibility, in general, to perform experiments at *in situ* or *operando* conditions.

The conventional version of the techniques mentioned, accessible at third generation synchrotron sources, requires the conjunction of several (and different) experiments to arrive at a convincing conclusion. Due to the advent of the new fourth generation of synchrotron sources, with very low emittance, micro and nanoprobes end-stations are the perfect tools for studies that can be more directly reached by only single shot, simultaneously analyzing the emerging probes at very high spatial resolution. The chosen examples of core@shell nanostructures observed with and without spatial resolution illustrate this.

The application of micro- and nanoprobes in the general field of nanoscience research is really auspicious. The X-ray micro- and nano-analytical techniques are quite unique tools for corroborating structures, chemical species, electronics,

magnetism and any other fundamental characteristic. Systems under study can vary from agglomerated atoms or molecules in confined regions to intracellular targets or very inhomogeneous structures, at different thermodynamic conditions, extending the limits of scientific experimentation.

Acknowledgments

References

[1] M. Acebrón, F.C. Herrera, M. Mizrahi, C. Navío, R. Bernardo-Gavito, D. Granados, F.G. Requejo and B.H. Juarez. Inorganically coated colloidal quantum dots in polar solvents using a microemulsion-assisted method. *Physical Chemistry Chemical Physics,* 19(3):1999-2007, 2017.

[2] S. Alayoglu, P. Zavalij, B. Eichhorn, Q. Wang, A. I. Frenkel and P. Chupas. Structural and Architectural Evaluation of Bimetallic Nanoparticles: A Case Study of Pt−Ru Core−Shell and Alloy Nanoparticles. *ACS Nano*, 3(10):3127-3137, 2009.

[3] D.K. Avasthi and G.K. Mehta. *Swift Heavy Ions for Materials Engineering and Nanostructuring, Springer Series in Materials Science* Vol. 145. Springer-Verlag, Berlin, Germany, 2011.

[4] P. Bleuet, P. Cloetens, P. Gergaud, D. Mariolle, N. Chevalier, R. Tucoulou, J. Susini and A. Chabli. A hard x-ray nanoprobe for scanning and projection nanotomography. *Rev. Sci. Instrum.*, 80, 056101:1-3, 2009

[5] T. Buonassisi, A.A. Istratov, M.A. Marcus, B. Lai, Z.H. Cai, S.M. Heald and E.R. Weber. Engineering metal-impurity nanodefects for low-cost solar cells. *Nat. Mater.*, 4(9):676-679, 2005.

[6] M.Y. Chiu, U.S. Jeng, C.H. Su, K.S. Liang and K.H. Wei. Simultaneous Use of Small- and Wide-Angle X-ray Techniques to Analyze Nanometerscale Phase Separation in Polymer Heterojunction Solar Cells. *Adv. Mater.* 20(13):2573–2578, 2008.

[7] M. Cotte, J. Szlachetko, S. Lahlil, M. Salome, V. A. Sole, I. Biron, and J. Susini. Coupling a wavelength dispersive spectrometer with a synchrotron-based X-ray microscope: A winning combination for micro-X-ray fluorescence and micro-XANES analyses of complex artistic materials. *J. Anal. At. Spectrom.* 26:1051-1059, 2011.

[8] M. Cotte, A. Genty-Vincent, K. Janssens, J. Susini. Applications of synchrotron X-ray nano-probes in the field of cultural heritage. *Comptes Rendus Physique,* 19(7):575-588, 2018.

[9] C.-H. Cui and S.-H. Yu. Engineering Interface and Surface of Noble Metal Nanoparticle Nanotubes toward Enhanced Catalytic Activity for Fuel Cell Applications. *Accounts of Chemical Research,* 46(7):1427-1437, 2013.

[10] V. De Andrade, J. Thieme, P. Northrup, Y. Yao, A. Lanzirotti, P. Eng and Q. Shen. The sub-micron resolution x-ray spectroscopy beamline at NSLS-II. *Nucl. Instrum. Meth. Phys. Res. Sect. A: Accelerat. Spectrom. Detect. Assoc. Equip.* 649: 46-48, 2011.

[11] C.-L. Dong and L. Vayssieres. In Situ/Operando X-ray Spectroscopies for Advanced Investigation of Energy Materials. *Chem. Eur. J.* 24, 18356-18373, 2018.

[12] M.R. Fitzsimmons, S.D. Bader, J.A. Borchers, G.P. Felcher, J.K. Furdyna, A. Hoffmann, J.B. Kortright, I.K. Schuller, T.C. Schulthess, S.K. Sinha, M.F. Toney, D. Weller and S. Wolf. Neutron scattering studies of nanomagnetism and artificially structured materials. J. Magn. Magn. Mater., 271;103:146, 2004.

[13] A.I. Frenkel, A. Yevick, C. Cooper and R. Vasic. Modeling the Structure and Composition of Nanoparticles by Extended X-Ray Absorption Fine-Structure Spectroscopy. *Annual Review of Analytical Chemistry*, 4(1):23-39, 2011.

[14] A.I. Frenkel. Applications of extended X-ray absorption fine-structure spectroscopy to studies of bimetallic nanoparticle catalysts. *Chem. Soc. Rev.*, 41:8163–8178, 2012.

[15] F.J. García de Abajo. Optical excitations in electron microscopy. *Rev. Mod. Phys.*, 82:209, 2010.

[16] M.B. Gawande, A. Goswami, T. Asefa, H. Guo, A.V. Biradar, D.-L. Peng, R. Zboril and R.S. Varma. Core–shell nanoparticles: synthesis and applications in catalysis and electrocatalysis. *Chem. Soc. Rev.,* 44:7540-7590, 2015.

[17] P. Glatzel and U. Bergmann. High resolution 1s core hole X-ray spectroscopy in 3d transition metal complexes-electronic and structural information. *Coord. Chem. Rev.*, 249:65-95, 2005.

[18] S. Guo, D. Li, H. Zhu, S. Zhang, N.M. Markovic, V.R. Stamenkovic, S. Sun. FePt and CoPt Nanowires as Efficient Catalysts for the Oxygen Reduction Reaction. *Angewandte Chemie International Edition*, 52(12):3465-3468, 2013.

[19] F. Hofmann, E. Tarleton, R.J. Harder, N.W. Phillips, P.-W. Ma, J.N. Clark, I.K. Robinson, B. Abbey, W. Liu, C.E. Beck. 3D lattice distortions and defect structures in ion-implanted nano-crystals. *Scient. Rep.* 7,45993,1-10, 2017.

[20] M. Holt, R. Harder, R. Winarski and V. Rose. Nanoscale hard X-ray microscopy methods for materials studies. *Annu. Rev. Mater. Res.*, 43(1):183–211, 2013.

[21] C. Hoskins, Y. Min, M. Gueorguieva, C. McDougall, A. Volovick, P. Prentice, Z. Wang, A. Melzer, A. Cuschieri, L. Wang. Hybrid gold-iron oxide nanoparticles as a multifunctional platform for biomedical application. *Journal of Nanobiotechnology,* 10(1):27-39, 2012.

[22] G.E. Ice, J.D. Budai, J.W.L. Pang. The race to X-ray microbeam and nanobeam science. *Science*, 334(6060):1234–1239, 2011.

[23] L.-Y. Jiang, X.-X. Lin, A.-J. Wang, J. Yuan, J.-J Feng and X.-S. Li. Facile solvothermal synthesis of monodisperse Pt2.6Co1 nanoflowers with enhanced electrocatalytic activity towards oxygen reduction and hydrogen evolution reactions. *Electrochimica Acta,* 225(Supplement C):525-532, 2017

[24] R. Koester, J.-S. Hwang, D. Salomon, X. Chen, C. Bougerol, J.-P. Barnes, D.L. Dang, L. Rigutti, A.D. Bugallo, G. Jacopin, M. Tchernycheva, C. Durand and J. Eymery. M-Plane Core-Shell InGaN/GaN Multiple-Quantum-Wells on GaN Wires for Electroluminescent Devices. *Nano Lett.*, (11):4839-4845, 2011.

[25] A. Kolmakov, S. Potluri, A. Barinov, T.O. Menteş, L. Gregoratti, M.A. Niño, A. Locatelli, M. Kiskinova. Spectromicroscopy for Addressing the Surface and Electron Transport Properties of Individual 1-D Nanostructures and Their Networks. *ACS Nano* 2(10):1993-2000, 2008.

[26] G. Krylova, N.M. Dimitrijevic, D.V. Talapin, J.R. Guest, H. Borchert, A. Lobo, T. Rajh and E.V. Shevchenko. Probing the Surface of Transition-Metal Nanocrystals by Chemiluminesence. *Journal of the American Chemical Society*, 132(26):9102-9110, 2010.

[27] G. Krylova, L.J. Giovanetti, F.G. Requejo, N.M. Dimitrijevic, A. Prakapenka and E.V. Shevchenko. Study of Nucleation and Growth Mechanism of the Metallic Nanodumbbells. *Journal of the American Chemical Society,* 134(9):4384-4392, 2012.

[28] W.M. Kwiatek and J.P. Glatzel. XAFS17 Highlights XAS and Related Techniques. *Synchrotron Radiation News,* 32(1):15-17, 2019.

[29] J. Leveneur, G.I.N. Waterhouse, J. Kennedy, J.B. Metson and D.R.G. Mitchell. Nucleation and Growth of Fe Nanoparticles in SiO2: A TEM, XPS, and Fe L-Edge XANES Investigation. *Phys. Chem. C,* 115(43):20978-20985, 2011.

[30] Q. Li, L. Wu, G. Wu, D. Su, H. Lv, S. Zhang, W. Zhu, A. Casimir, H. Zhu, A. Mendoza-Garcia and S. Sun. New Approach to Fully Ordered fct-FePt Nanoparticles for Much Enhanced Electrocatalysis in Acid. *Nano Letters*, 15(4):2468-2473, 2015

[31] M.D. Mizrahi, G. Krylova, L.J. Giovanetti, J.M. Ramallo-López, Y. Liu, E.V. Shevchenko and F.G. Requejo. Unexpected compositional and structural modification of CoPt3 nanoparticles by extensive surface purification. *Nanoscale,* 10:6382-6392, 2018.

[32] G. Martinez-Criado, J. Segura-Ruiz, M. H.Chu, R.Tucoulou, I.Lopez, E. Nogales, B. Mendez and J. Piqueras. Crossed Ga2O3/SnO2 Multiwire Architecture: A Local Structure Study with Nanometer Resolution. *Nano Lett*. 14(10):5479:5487, 2014.

[33] G. Martínez-Criado, J. Villanova, R. Tucoulou, D. Salomon, J.-P. Suuronen, S. Labouré, C. Guilloud, V. Valls, R. Barrett, E. Gagliardini, Y. Dabin, R. Baker, S. Bohic, C. Cohen and J. Morse. ID16B: a hard X-ray nanoprobe beamline at the ESRF for nano-analysis. *J. Synchrotron Rad.*, 23:344-352, 2016.

[34] L. Mino, E. Borfecchia, J. Segura-Ruiz, C. Giannini, G. Martinez-Criado and C. Lamberti. Materials characterization by synchrotron x-ray microprobes and nanoprobes. *Rev. Mod. Phys.*, 90(2):025007, 2018.

[35] D.E. Morrison, J.B. Aitken, M.D. de Jonge, J.A. Ioppolo, H.H. Harris, L.M. Rendina. High mitochondrial accumulation of new gadolinium(III) agents within tumour cells. *Chem. Commun.* 50:2252-2254, 2014.

[36] S. Mourdikoudis, R.M. Pallares and N.T.K. Thanh. Characterization techniques for nanoparticles: Comparison and complementarity upon studying nanoparticle properties. *Nanoscale,* 10:12871-12934, 2018.

[37] National Nanotechnology Initiative. *X-rays and Neutrons: Essential Tools for Nanoscience Research*. Report of the National Nanotechnology Initiative Workshop, Washington, 2005.

[38] E. Nazaretski, K. Lauer, H. Yan, N. Bouet, J. Zhou, R. Conley and X. Huang. Pushing the limits: an instrument for hard x-ray imaging below 20 nm. *J. Synchrotron Radiat.*, 22:336-341, 2015.

[39] E. Nazaretski, H. Yan, K. Lauer, N. Bouet, X. Huang, W. Xu, J. Zhou, D. Shu, Y. Hwu and Y. S. Chu. Design and performance of an X-ray scanning microscope at the Hard X-ray Nanoprobe beamline of NSLS-II. *J. Synchrotron Rad.,* 24:1113-1119, 2017.

[40] S.A. Nepijko, E. Pippel and J. Woltersdorf. Dependence of lattice parameter on particle size. *Physica status solidi (a)*, 61(2):469-475, 1980.

[41] D.A. Neumann. Neutron scattering and hydrogenous materials. *Mater. Today* 9:34-41, 2006.

[42] J.L. Provis, V. Rose, S.A. Bernal and J.S.J. van Deventer. High-Resolution Nanoprobe X-ray Fluorescence Characterization of Heterogeneous Calcium and Heavy Metal Distributions in Alkali-Activated Fly Ash. *Langmuir*, 25(19):11897-11904, 2009.

[43] J.M. Ramallo-Lopez, L. Giovanetti, A.F. Craievich, F.C. Vicentin, M. Marin-Almazo, M. Jose-Yacaman and F.G. Requejo. XAFS, SAXS and HREM characterization of Pd nanoparticles capped with n-alkyl thiol molecules. *Physica B,* 389:150-154, 2007.

[44] M. Salmeron. From Surfaces to Interfaces: Ambient Pressure XPS and Beyond. *Top. Catal.,* 61(20):2044-2051, 2018.

[45] C. Sanchez-Cano, D. Gianolio, I. Romero-Canelon, R. Tucoulou and P.J. Sadler. Nanofocused synchrotron X-ray absorption studies of the intracellular redox state of an organometallic complex in cancer cells. *Chem. Commun.*, 55:7065-7068, 2019.

[46] S. Schorr. The crystal structure of kesterite type compounds: A neutron and X-ray diffraction study. *Solar Energy Mater. Solar Cells*, 95(6):1482-1488, 2011.

[47] E. Secco, H.T. Mengistu, J. Segura-Ruíz, G. Martínez-Criado, A. García-Cristóbal, A. Cantarero, B. Foltynski, H. Behmenburg, C. Giesen, M. Heuken, N. Garro. Elemental Distribution and Structural Characterization of GaN/InGaN Core-Shell Single Nanowires by Hard X-ray Synchrotron Nanoprobes. *Nanomaterials*, 9(5):691-1,11, 2019.

[48] D. A. Shapiro, Y.-S. Yu, T. Tyliszczak, J. Cabana, R. Celestre, W. Chao and K. Kaznatcheev. Chemical composition mapping with nanometre resolution by soft x-ray microscopy. *Nat. Photon.*, 8:765-769, 2014.

[49] J. Singh, C. Lamberti and J.A. van Bokhoven. Advanced X-ray absorption and emission spectroscopy: in situ catalytic studies. *Chem. Soc. Rev.*, 39:4754-4766, 2010.

[50] V.R. Stamenkovic, B.S. Mun, K.J.J. Mayrhofer, P.N. Ross and N.M. Markovic. Effect of Surface Composition on Electronic Structure, Stability, and Electrocatalytic Properties of Pt-Transition Metal Alloys: Pt-Skin versus Pt-Skeleton Surfaces. *Journal of the American Chemical Society* 128(27):8813-8819, 2006.

[51] M. Suzuki. Hard-X-ray magnetic microscopy and local magnetization analysis using synchrotron radiation. *Microscopy*, 63(1):14-15, 2014.

[52] F. Tao, M. E. Grass, Y. Zhang, D. R. Butcher, J. R. Renzas, Z. Liu, J. Y. Chung, B. S. Mun, M. Salmeron and G. A. Somorjai. Reaction-Driven Restructuring of Rh-Pd and Pt-Pd Core-Shell Nanoparticles. *Science*, 322:932–934, 2008.

[53] H.C.N. Tolentino, M.M. Soares, C.A. Perez, F.C. Vicentin, D.B. Abdala, D. Galante, V. de C. Teixeira, D.H.C. de Araújo and H. Westfahl Jr.. CARNAÚBA: The Coherent X-Ray Nanoprobe Beamline for the Brazilian Synchrotron SIRIUS/LNLS. *J. Phys.: Conf. Ser.*, 849:012057, 2017.

[54] H.C.N. Tolentino, M.M. Soares, F.M.C. Silva, J.H. Rezende, D. Puglia, A. Bordin, M.S. Silva and R.R. Geraldes. Innovative instruments based on cryogenically cooled silicon crystals for the CARNAÚBA beamline at Sirius-LNLS. *AIP Conference Proceedings*, 2054:060026, 2019.

[55] H.C.N. Tolentino, R.R. Geraldes, *et al.* TARUMÃ station for the CARNAUBA beamline at SIRIUS/LNLS. Proc. SPIE 11112, X-Ray Nanoimaging: *Instruments and Methods IV*, 1111206, 2019.

[56] A. Ulvestad, A. Singer, J.N. Clark, H.M. Cho, J.-W. Kim, R. Harder, J. Maser, Y.S. Meng and O.G. Shpyrko. BATTERIES. Topological defect dynamics in operando battery nanoparticles. *Science*, 348(6241):1344-1347, 2015.

[57] D.F. van der Vliet, C. Wang, D. Li, A.P. Paulikas, J. Greeley, R.B. Rankin, D. Strmcnik, D. Tripkovic, N.M. Markovic, V.R. Stamenkovic. Unique Electrochemical Adsorption Properties of Pt-Skin Surfaces. *Angewandte Chemie*, 124(13):3193-3196, 2012.

[58] M.L. Vera, A. Cánneva, C. Huck-Iriart, F.G. Requejo, M.C. Gonzalez, M.L. Dell'Arciprete, A. Calvo. Fluorescent silica nanoparticles with chemically reactive surface: Controlling spatial distribution in one-step synthesis. *Journal of colloid and interface science* 496:456-464, 2017.

[59] B. Vianne, M.I. Richard, S. Escoubas, S. Labat, T. Schuelli, G. Chahine, V. Fiori and O. Thomas. Through-silicon via-induced strain distribution in silicon interposer. *Appl. Phys. Lett.*, 106(14):141905,1-5, 2015.

[60] J. Villanova, J. Segura-Ruiz, T. Lafford and G. Martínez-Criado. Synchrotron microanalysis techniques applied to potential photovoltaic materials. *Journal of synchrotron radiation,* 19: 521-524, 2012.

[61] Z. L. Wang, T. S. Ahmad and M. A. El-Sayed. Steps, ledges and kinks on the surfaces of platinum nanoparticles of different shapes. *Surf. Sci.*, 380:302-310, 1997

[62] R.P. Winarski, M.V. Holt, V. Rose, P. Fuesz, D. Carbaugh, C. Benson and D. Shu. A hard x-ray nanoprobe beamline for nanoscale microscopy. *J. Synchrotron Radiat.*, 19:1056-1060, 2012.

[63] L.E. Wu, A. Levina, H.H. Harris, Z. Cai, B. Lai, S. Vogt, D.E. James, P.A. Lay. Carcinogenic Chromium(VI) Compounds Formed by Intracellular Oxidation of Chromium(III) Dietary Supplements by Adipocytes. *Angew. Chem.,* 128:1774-1777, 2016.

[64] L. Wu, A. Mendoza-Garcia, Q. Li and S. Sun. Organic Phase Syntheses of Magnetic Nanoparticles and Their Applications. *Chemical Reviews* 55(5):1742-1745, 2016.

[65] H.L. Xin, S. Alayoglu, R. Tao, A. Genc, C.-M. Wang, L. Kovarik, E.A. Stach, L.-W. Wang, M. Salmeron, G.A. Somorjai and H. Zheng. Revealing the Atomic Restructuring of Pt–Co Nanoparticles. *Nano Letters*, 14(6):3203-3207, 2014.

[66] L. Yan, S. Jahangir, S.A. Wight, B. Nikoobakht, P. Bhattacharya and J.M. Millunchick. Structural and Optical Properties of Disc-in-Wire InGaN/GaN LEDs. *Nano Lett.*, 15(3):1535-1539, 2015.

[67] Y. Yao and J.A. van Kan. Automatic beam focusing in the 2nd generation PBW line at sub-10 nm line resolution. *Nucl. Instrum. Methods Phys. Res., Sect. B,* 348:203-208, 2015.

[68] G.-C. Yin, S.-H. Chang, B.-Y. Chen, H.-Y. Chen, B.-H. Lin, S.-C. Tseng, C.-Y. Lee, J.-X. Wu, S.-Y. Wu and M.-T. Tang. X-ray nanoprobe project at Taiwan Photon Source. *AIP Conference Proceedings*, 1741:030004, 2016.

[69] K. Zhang, Z. Zhao, Z. Wu and Y. Zhou. Synthesis and detection the oxidization of Co cores of Co@SiO2 core-shell nanoparticles by in situ XRD and EXAFS. *Nanoscale Res. Lett.*, 10:37-46, 2015.

[70] J.F. Ziegler and J.P. Biersack. *Treatise on Heavy-Ion Science, Astrophysics, Chemistry, and Condensed Matter, Vol. 6. D. A. Bromley. Springer US, Boston, MA, USA, 1985.*

Bio

Félix G. Requejo

Professor at the National University of La Plata (UNLP, Argentina) and Researcher at CONICET, he obtained his PhD in Physics from UNLP in 1993. He was a postdoctoral fellow at the Lawrence Berkeley National Laboratory (CA, USA) in 2000 under the supervision of Prof. M.B. Salmeron. Back in Argentina in 2003, he started to work in characterization of nanomaterials, employing techniques derived from the use of synchrotron radiation. Prof. Requejo has published over 130 articles in international journals. He led more than hundred research proposals at different synchrotron laboratories around the world and formed several Ph.D. students. He received the "Dra. María Cristina Giordano" Prize in 2010 and the KONEX Prize in Nanotechnology in 2013.

INSTRUCTIONS FOR AUTHORS

GUIDELINES

1. Length

Research reviews should not be less than 7000 words or more than 10,000 words (plus up to 15 figures and up to 50 references).

2. Structure

Whenever possible articles should adjust to the standard structure comprising:
(a) Graphical abstract,
(b) Abstract,
(c) Introduction describing the focus of the review,
(d) Article main body including assessment and discussion of available information (may be further subdivided),
(e) Conclusions,
(f) Bibliography.

3. Format

Authors must submit their articles in a Microsoft Word archive. Figures must be embedded in the article and also submitted in a separate .zip or .rar file.

4. References

References must be numbered in the text ([1] [2] [3]) and identified with the same numbers in the *References* section. Up to 50 references are allowed. The following are examples to take into account in each case.

BOOKS:
- Single author
Chung, R. *General Chemistry: Fundamental Knowledge,* 2nd ed.; McGuffin-Hill: Kansas City, 2003.
- More than one author
Chung, R.; Williamson, M. *General Chemistry: Fundamental Knowledge*, 2nd ed.; McGuffin-Hill: Kansas City, 2003.
- Edited Book
Kurti, F. Photodissociation and Reactive Scattering. In *The Rise of Chemical Physics*; White, AD, Ed.; Wilson: New Jersey, 2007; Vol. 128; p. 257.
- Book in Series
Goth, V. Polymer Chemistry. In *The Foundational Course in Organic Chemistry*; ACDC Symposium Series 1151; American Chemical Fraternity: Seattle, 2014; pp 123-149.
- Article from a reference book
Powder and Metallurgy. *Dictionary of Chemical Technology*, 3rd ed.; Wilson: New Jersey, 1971; Vol. 12, pp 68-82.

ARTICLES:

- Article in a scientific journal

Evans, A.; Stitch, M.; Smithers, ET; Nope, JJ Complex Aldol Reactions to the Total Synthesis of Phorboxazole B. *J. Am. Chem*. Soc. 2012, 122, 10033-10046.

- Article in a popular/non-scientific magazine

Tatum, CJ Super Organics. *Wireless* , June 2001, pp 76-93.

- Article from an online journal

Turkey-Lopez, E. Inexact Solutions of the Quantum Double Square-Well Potential. *Chem. Ed.* [Online] 2007, 11, pp. 838-847. http://chemeducator.org/bibs/0011006/11060380lb.htm (accessed Aug 5, 2019).

PUBLICATION ETHICS

The journal considers that the primary objective of all submissions must be a contribution of relevant and appropriate content, and that all review processes must be structured based on that general criterion. Therefore, there is an emphasis on the concern to maintain the highest quality and ethics standards in the reception, evaluation and publication of articles. These standards include the three participants of the process: author, reviewer and editor.

1. Author's responsibilities

- Submitted manuscripts should maintain rigorous scientific criteria for data validation and conclusions.
- All data (Figures, Tables, etc.) reproduced from previous published articles must give the appropriate recognition to the source. Plagiarism is cause enough to reject the submission.
- Authorship must include all individuals who have contributed in a substantial way to the composition, prior investigation, and execution of the paper. Minor contributions must be acknowledged, but these contributors should not be listed as authors. The main author or authors of the article will make sure that all participants of the paper have approved the final version of the document submitted.
- All authors must reveal in their final manuscript any financial or other type of conflict of interests that might interfere with the results and interpretations in their research. All funding received to carry out the project must be acknowledged.
- After the article is published, in the event an author notices a crucial fault or inaccuracy, he or she should immediately report that fault or inaccuracy, so that an Erratum can be issued as soon as possible.

2. Reviewer's responsibilities

Reviewing is a time-consuming process that is carried out *ad honorem* by *bona fide* scientists conversant with the subject of the reviewed paper. The quality and the ethical standards of the journal depend critically on the quality of the reviewing process, and the following guidelines are established:

- All documents sent to the journal for review will be considered confidential documents and will not be discussed with external third parties.
- When invited, a potential reviewer should decline if: (a) the subject of the article is not within his/her area of expertise; (b) there is any kind of conflict of interest; (c) if the review cannot be finished within the period established by the journal.
- Any criticism or objections to the paper should be done in a neutral tone and based on reasonable grounds, not limited to simple opinions or purely subjective expressions.

3. Editor's responsibilities

- The editors are responsible for selecting the papers that will be published in the journal. The Editorial Management must comply with the ethical standards of the journal, as well as with all legal guidelines, including the prohibition of plagiarism and any other form of copyright infringement.
- The editors will evaluate and make decisions on the articles sent to the journal regardless of the gender, sexual orientation, religious beliefs, ethnic origin, nationality or political ideology of the authors.
- Revealing information identifying reviewers is forbidden.
- The final version of all materials can be published only with the prior approval of their author.
- The editors will refrain from publishing manuscripts that imply a conflict of interests because of any possible connection with other institutions, companies and authors.
- Before deciding to send an article to a peer review, the editors are committed to thoroughly read all texts received and determine their appropriateness to the thematic universe of the journal.
- If a misbehavior or unethical action by an author or reviewer is identified, the editors must request the informer of such conduct or action to provide the evidence that may justify a possible investigation. All accusations will be handled seriously until reliable results are obtained regarding its truthfulness or falseness. If an investigation takes place, the editors are responsible for choosing the appropriate way in which it will be carried out. They can also request the advice and assistance from the Editorial Board, as well as from reviewers and authors.
- In the event a serious non-malicious mistake or a dishonest conduct by an author or a reviewer is proved, the editors shall act according to the nature and seriousness of the case. The actions the editors may take include, but are not limited to: notifying the author or reviewer of the existence of a serious mistake or misapplication of the ethical standards of the journal; writing a strong statement that reports and warns about a bad practice or unethical behavior; publishing that statement; unilaterally withdrawing the reported paper from the review or publication process; revoking the paper if it has already been published; communicating the journal's decision and the reasons behind it to the general public; and banning paper submissions by the people involved for a certain period of time.

PRIVACY STATEMENT

The names and email addresses entered in this journal site will be used exclusively for the stated purposes of this journal and will not be made available for any other purpose or to any other party.

NEXT ISSUE
Vol. 1, No. 4

TO BE PUBLISHED ON SEPTEMBER 15, 2020

We are preparing a special issue covering the ongoing R&D projects on CO-VID-19 in Argentina.

Science Reviews
from the end of the world